SPECTROSCOPIC INVESTIGATION OF RADIATION INDUCED EFFECTS IN BOROSILICATE GLASSES USED FOR IMMOBILIZATION OF NUCLEAR WASTES

By

MANOJ MOHAPATRA

(CHEM 01200604018)

Radiochemistry Division

Bhabha Atomic Research Centre, Trombay, Mumbai

A thesis submitted to the
Board of Studies in Chemical Sciences
In partial fulfillment of requirements
For the Degree of

DOCTOR OF PHILOSOPHY

Of

HOMI BHABHA NATIONAL INSTITUTE

January, 2013

SPECTROSCOPIC INVESTIGATION OF RADIATION INDUCED EFFECTS IN BOROSILICATE GLASSES USED FOR IMMOBILIZATION OF NUCLEAR WASTES

By

MANOJ MOHAPATRA

(CHEM 01200604018)

Radiochemistry Division

Bhabha Atomic Research Centre, Trombay, Mumbai

A thesis submitted to the
Board of Studies in Chemical Sciences
In partial fulfillment of requirements
For the Degree of

DOCTOR OF PHILOSOPHY
Of
HOMI BHABHA NATIONAL INSTITUTE

January, 2013

Homi Bhabha National Institute

Recommendations of the Viva Voce Board

As members of the Viva Voce Board, we certify that we have read the dissertation prepared by Mr. Manoj Mohapatra entitled 'Spectroscopic investigation of radiation induced effects in borosilicate glasses used for immobilization of nuclear wastes' and recommend that it may be accepted as fulfilling the dissertation requirement for the Degree of Doctor of Philosophy.

Date: 13|11|13
Chairman-Prof. K. L. Ramakumar

Date:
Guide- Prof. B. S. Tomar

Date: 13/11/2013
Member-Prof.A.Goswami Goswami

Date: 13-11-2013
Member-Prof. P.K.Mohapatra

Date:
Member- N. Vareich 13/11

Final approval and acceptance of this dissertation is contingent upon the candidate's submission of the final copies of the dissertation to HBNI.

I hereby certify that I have read this dissertation prepared under my direction and recommend that it may be accepted as fulfilling the dissertation requirement.

Date: 13/11/2013

Place: BARC, Trombay, Mumbai

STATEMENT BY AUTHOR

This dissertation has been submitted in partial fulfillment of requirements for an advanced degree at Homi Bhabha National Institute (HBNI) and is deposited in the Library to be made available to borrowers under rules of the HBNI.

Brief quotations from this dissertation are allowable without special permission, provided that accurate acknowledgement of source is made. Requests for *permission for extended quotation from or reproduction of this manuscript in* whole or in part may be granted by the Competent Authority of HBNI when in his or her judgment the proposed use of the material is in the interests of scholarship. In all other instances, however, permission must be obtained from the author.

Manoj mohapatra
(Manoj Mohapatra)

DECLARATION

I, hereby declare that the investigation presented in the thesis has been carried out by me. The work is original and has not been submitted earlier as a whole or in part for a degree / diploma at this or any other Institution / University.

Manoj Mohapatra
(Manoj Mohapatra)

ACKNOWLEDGEMENTS

In the first place, I wish to express my deep sense of gratitude to my guide Prof.B.S.Tomar, for his invaluable guidance with affection and constant encouragement all throughout the course of this work. I sincerely acknowledge my gratitude to Prof. S. V. Godbole, for his valuable suggestions, constant support and encouragement for completion of this work. It gives me immense pleasure to record my sincere thanks to Prof.V.K.Manchanda for his valuable inputs in the work. I am grateful to Prof. K. L.Ramakumar, Chairman, Doctoral Committee for his constant encouragement. Thanks are also due to Prof. A.Goswami and Prof. P.K. Mahapatra, members of the doctoral committee for their constructive suggestions.

I gratefully acknowledge the help of Prof.R.M.Kadam during the entire doctoral work. I am highly grateful to Prof.P.K.Pujari for his help in the positron annihilation work and useful discussions. I sincerely thank the staff of ILU-6, Vashi and EBC, Kharghar for providing the electron beam facility. Thanks are also due to the staff of BARC-TIFR pelletron facility for providing beam time for heavy ion irradiation. I am thankful to Dr. R.J.Kshirsagar, SR&HPPD, BARC for facilitating the FTIR and ATR-FTIR data. I express my gratitude to Dr J.G.Abraham and Prof.V.Kain, MSD, BARC for providing the micro-Raman data.

I place on record my sincere thanks to all my collogues, Dr. A.R.Dhobale, Dr.Y.Babu, Dr.T.K.Seshagiri, Dr.Mrs.P.J.Purohit, Dr.V.Natarajan, Dr.N.K.Porwal, Dr.M.K.Bhide, Dr.S.K.Thulasidas, Dr.Mrs.N.Goyal, Dr.Mrs.M.J.Kulkarni, Dr.Mrs.V.C.Adya, Mrs.B.Rajeswari, for their constant support and encouragement.

I am thankful to Prof.S.K.Ghosh, Dean Chemical Sciences, HBNI and Director, BARC, for allowing me to register for PhD. degree with HBNI and for kindly permitting me to utilize the infrastructure of BARC for this work. I express my gratitude towards HBNI under whose auspices this dissertation work was carried out.

I owe special gratitude to my beloved wife Swagatika for tolerating my silliness and encouraging me to complete the work. Last but not the least; I would like to acknowledge the presence of my cute little Guchu who is the reason behind my every positivity in spite of all the odds.

(Manoj Mohapatra)

CONTENTS

Description Page No

CHAPTER-I

CHAPTER-II

EXPERIMENTAL TECHNIQUES

CHAPTER-III

SPECTROSCOPIC INVESTIGATIONS OF THE BOROSILICATE WASTE GLASSES PRIOR TO IRRADIATION

3.3. Results and discussion

CHAPTER-IV

SPECTROSCOPIC INVESTIGATIONS OF THE GAMMA IRRADIATED BOROSILICATE WASTE GLASSES

4.3. Results and Discussion

A. Studies on the base glass

B. Studies on the Eu doped glass

C. Studies on the Fe doped glass

CHAPTER-V

SPECTROSCOPIC INVESTIGATIONS OF THE ELECTRON BEAM IRRADIATED BOROSILICATE WASTE GLASSES

5.3 Results and Discussion

CHAPTER-VI

SPECTROSCOPIC INVESTIGATIONS OF THE HEAVY ION IRRADIATED BOROSILICATE WASTE GLASSES

CHAPTER-VII

SUMMARY AND OUTLOOK

LIST OF FIGURES

LIST OF TABLES

Synopsis

Nuclear energy is one of the better options for mankind available today keeping in mind the growing energy demands and concerns for a clean environment. In order to achieve this, India has adopted a three stage nuclear power program based on closed uranium, plutonium and thorium based fuel cycles [1]. One of the important aspects for successful operation of such nuclear fuel cycles is safe management of the nuclear waste generated during the fuel cycle. A major portion of the waste comes from the so called high level radioactive liquid waste (HLW) generated after the reprocessing of spent nuclear fuels. It is estimated that majority of the radioactivity encountered in the entire nuclear fuel cycle gets concentrated in the corresponding HLW. Apart from the residual and minor actinides, the major constituents of the HLW are the fission/activation and corrosion products, process pick up elements, chemical additives etc. To manage this highly radioactive substance, the philosophy of 'concentrate and contain' is applied where in, the waste is fixed in some suitable inert matrix. The composition of the matrix depends on the nature of the waste which in turn depends on the nature of the reactor/fuel, cooling period, process flow sheet etc. Matrices such as borosilicate based glasses, glass-ceramics; synthetic inorganic matrices (synroc) etc have been explored for this purpose. Among these, borosilicate based glass systems have been adopted universally as the matrix for immobilization of HLW on industrial scale [2]. These glasses possess desirable properties like high chemical, mechanical, thermal and radiation stability for HLW storage. Also, the amorphous nature of the glass helps to accommodate the waste containing a variety of elements easily [3-4].

At Bhabha Atomic Research Centre (BARC), Trombay, the stored HLW generated from the research reactors is characterized by the presence of high amounts of sulfate ions and sodium along with other products. Sulfate in the waste is derived from ferrous sulfamate [$Fe(NH_2SO_3)_2$] used as a reducing agent for conversion of Pu^{4+} to Pu^{3+} at partitioning stage of the actinides during reprocessing. Sulfate is one of the troublesome ions having limited solubility in borosilicate glass matrices and thus creates a separate phase during vitrification. To deal with this problem, a barium oxide containing sodium borosilicate glass has been developed in Waste Management Division, BARC which is routinely used for the waste immobilization [5]. The quaternary system of $BaO-Na_2O-B_2O_3-SiO_2$ referred to as the base glass is found to be suitable to deal the problem of sulfate ions forming a separate phase without affecting the waste oxide loading.

Because of the decay of the radioactive components such as fission /activation products and minor actinides present in the waste, the glass experiences radiation damage. These damages can significantly alter the glass structure which may influence their long term leaching behavior. Several reports are available in literature focusing on the radiation induced changes in borosilicate glasses of varying composition. These materials can undergo changes in their structure, mostly by ionization and ballistic interaction of high-energy radiation with the atoms of the glass matrix, that introduce disorders in the original structure causing formation of defect centers accompanied with volume changes, phase separation or gas accumulation etc. A comprehensive review has been given in this aspect by Weber et al in their classical paper [6]. It is pivotal to study these changes so as to predict the long term leaching behavior of the vitrified waste product. Moreover, it is well known that the optimal engineering performance of a glass is dominated by its structure. So, the knowledge of the glass structure before and after irradiation is a prerequisite for understanding the structural evolution of glasses under long term irradiation [7].

In the present work, barium based alkali borosilicate glass samples having similar composition to the Trombay nuclear waste glass were investigated for radiation induced changes by spectroscopic techniques. The waste glasses were also investigated prior to irradiation to carry out speciation study of the various metal ions expected to be present in the waste glass. These studies on the borosilicate glasses will lead to an understanding of the nature of the damage which can further lead to fabrication of materials in which the deleterious effects of radiation can be minimized. Moreover, careful study of radiation induced defects can help to elucidate certain structural aspects of the glassy state which cannot be readily accessible by other means.

The details of the experimental procedures, instruments used for characterization and results have been discussed in total seven chapters, as summarized below.

Chapter- I: Introduction

This chapter briefly discusses the importance of nuclear energy, three stages of the Indian Nuclear Energy Program, nuclear waste management philosophy and waste classification. It also describes the different matrices used for fixing the radioactive wastes such as borosilicate glass, glass-ceramics, SYNROC etc and highlights the salient features of each of them. It gives a brief overview of the current literature available on radiation induced changes in nuclear waste glasses of various compositions. The importance of spectroscopic techniques for these types of investigations has also been discussed in the chapter.

Chapter II: Experimental Details

The different spectroscopic techniques used to characterize the glasses along with a brief overview of the glass preparation have been given in this chapter. Details of the irradiation facilities used for the experiments have also been discussed.
The various spectroscopic techniques described in the chapter include:

1. X-Ray Diffraction (XRD)
2. Electron Probe Micro Analysis (EPMA)
3. UV-Visible absorption
4. Photoluminescence (PL)
5. Electron Paramagnetic Resonance (EPR)
6. Photoacoustic spectroscopy
7. Positron Annihilation Spectroscopy (PAS)
8. FTIR
9. Raman Spectroscopy

Chapter –III: Spectroscopic investigations of the borosilicate waste glasses prior to irradiation

This chapter describes the UV-Visible, PL, EPR and PAS investigations of the base glass samples prior to irradiation. This work was carried out in order to characterize the oxidation states and coordination behavior of several transition metal ions namely Cr, Cu, Fe and Mn and rare earth (RE) ions, namely, Eu and Gd in the nuclear waste glasses. The respective metal ions were individually doped in the base glass and studied by the spectroscopic techniques. As the transition elements mimic the process pickup elements and the RE ions mimic the minor actinides (e.g. Am and Cm) and the fission products, this exercise gives us an idea about the speciation of these metal ions in the waste glass before irradiation.

From these studies it was observed that Cr ions got stabilized in the glass matrix in two oxidation states namely 3+ and 5+ in distorted octahedral geometries where as Cu ions got stabilized as Cu^{2+} only. In case of Fe incorporated glass, it was found that iron gets stabilized in 3+ oxidation state both in tetrahedral and octahedral geometries. In case of Mn incorporated glass, it was found out that, apart from the usual 2+ oxidation state, Mn gets stabilized in the matrix in the form of MnO_4^- and MnO_4^{2-}.

In case of the RE ions, it was observed that, both the ions (Eu and Gd) stabilized in the most stable 3+ state in asymmetric geometries. Spectral analysis of the Eu-glass was carried out to evaluate the Judd-Ofelt (J-O) intensity parameters and various radiative properties such as radiative transition rate (A_R), radiative and non-radiative lifetimes (τ_R and τ_{NR}) and luminescence branching ratios (β_R). These properties suggested the existence of short range ordering in the glass with higher covalence between the rare earth ions and the surrounding oxygens.

After these investigations on the pristine glass samples, experiments were carried out on irradiated glass samples as discussed below.

Chapter IV: Spectroscopic investigations of gamma irradiated nuclear waste glasses

Gamma radiation induced changes in the waste glasses were investigated by irradiating them in a ^{60}Co gamma chamber with a dose rate of 1kGy/hr. The Trombay waste base glass as well as glasses doped with transition metal and rare earth ion was investigated for the radiation induced changes. The base glass sample was irradiated up to a dose of 100kGy and investigated by EPR spectroscopy. Two individual sets of representative glasses containing either Fe or Eu were also irradiated at varying dose and studied by

EPR and PL techniques. The radiation induced radicals were observed to be similar in nature in both the base and doped glasses. Detailed temperature variation and microwave power variation experiments were carried out by EPR technique to unequivocally identify all the defect centers formed in the systems. The results showed the formation of silicon hole centers and electron trap centers apart from boron based oxy hole centers (BOHC) in the glasses due to the gamma irradiation. The EPR Hamiltonian parameters for these radicals were evaluated by computer simulation technique using Bruker SIMFONIA computer program.

The iron containing glasses were irradiated up to a maximum radiation dose of 250 kGy. Glasses with varying iron content (from 0.1 mol % to 2.5 mol %) were irradiated with the same amount of dose to evaluate the effect of iron content on the defect centre concentration. A spin counting technique was employed to evaluate the number of defect centers formed in each glass. It was observed that the defect centre concentration reduced as a function of increasing iron content. This was attributed to the charge trapping process of ferric ions in the amorphous system.

In case of the glasses containing Eu also similar type of defect centers were observed to be formed upon gamma irradiation. No change in the oxidation states of the metal ion was observed on gamma irradiation up to a dose of 900 kGy. It was also observed that, the metal ion distributes itself in two different environments in the irradiated glass. To use Eu^{3+} ion as a local probe for radiation induced changes in the glass matrix, Judd-Ofelt (J-O) analyses of the emission spectra were done before and after irradiation. No change was observed in the J-O intensity parameter Ω_2 on irradiation; however, Ω_4 changed significantly indicating change in the long range ordering in the amorphous matrix. A similar spin counting was employed to quantify the number of defect centres formed in the glass at the highest gamma dose studied. From the spin counting studies the concentration of defect centres in the glass was calculated to be 350 ppm at 900 kGy. This indicated the fact that bulk of the glass remained unaffected after gamma irradiation up to 900 kGy.

Chapter –V: Spectroscopic investigations of electron beam irradiated nuclear waste glasses

Electron beam irradiations can simulate the effects of beta irradiation in HLW glasses to a great extent if not in totality [8]. Several effects such as the rates of alkali ion exchange in radiation fields do show a non-Arrhenius behavior depending on both the irradiation dose and dose rate as suggested by Ojovan and Lee [9]. Nevertheless, many literature reports are available where nuclear waste glasses of varying compositions were irradiated by high energy electron beams to simulate the beta irradiation effects [10-12].

In this context, spectroscopic investigations were carried out on the waste glasses irradiated with high energetic electron beam. The samples were irradiated with cumulative doses of 10^5, 10^6 and 10^8 Gy by varying the beam exposure time. In addition to EPR technique, PL, PAS and FTIR investigations were done on the irradiated samples to evaluate the radiation induced changes in the glass. This chapter describes the results obtained in this study in detail. Defect centers similar to those observed in case of gamma irradiated samples were also observed in this case by PL and EPR techniques. From the experiments it was concluded that, boron-oxygen and silicon based hole centers along with E' centers are getting formed in the glass after irradiation due to the breaking of the Si-O bonds at regular tetrahedron sites of Si-O-Si. The PAS data gave an idea regarding the free volume size and fraction of the glasses before and after irradiation. It was seen that, after irradiation the free volume size in the glass increased with creation of additional sites. Here also the spin counting technique was used to evaluate the defect concentration in the glasses after irradiation. It was observed that even at 10^8 Gy, the number of defect centers were few hundreds of ppm. This, in a way, confirmed the radiation stability of the barium borosilicate glasses routinely used for vitrifying the research reactor nuclear waste. This fact was further supported by the FTIR data where no change was observed in the glass network on irradiation. Since, FTIR is a bulk technique, the results suggested that, on irradiation, even if some defect centers get generated and the glass network gets modified, on a macroscopic scale, bulk of the glass remains unaffected.

Chapter –VI: Spectroscopic investigations of heavy ion irradiated nuclear waste glasses

This chapter is devoted to the radiation damage in the waste glasses caused by heavy ion irradiation. External heavy ion irradiation is a convenient laboratory technique for simulating the alpha damages in the borosilicate glasses from radioactive waste encapsulation point of view [13]. Several reports are available in the literature where heavy ion irradiation studies have been done on nuclear waste glasses to assess the effects of alpha decay on the structural properties of the glass matrix [14, 15].

In this context, high energetic ^{4}He and ^{12}C particles were impinged on the waste glasses and the changes occurring in the glasses were investigated using micro Raman and FTIR (in attenuated total reflection mode) techniques. The maximum dose received by the samples was ~10^{11} Gy. The micro Raman data suggested modification in the silicate network due to the irradiation. Formation of molecular oxygen was also noticed in the borosilicate glass irradiated by helium ions. These modifications were ascribed to the breaking of the Si-O bonds at regular sites and dislocation of the alkali metal ion form its position. However, in the FTIR investigations, no significant changes in the band positions were observed. This suggested that, even after the heavy ion irradiation, bulk of the glass remains unaffected.

Chapter –VII: Conclusion and Future scope

A brief summary of the investigations taken up in this doctoral work and its future scope is presented in this chapter. In the present study, an attempt has been made to characterize the nuclear waste glasses for radiation induced changes by spectroscopic techniques. Moreover, the quantification of the defect centers formed in the glasses due to irradiation could be done. For the first time, the radiation stability of the indigenously developed Trombay nuclear waste glass has been assessed in the study. It was estimated that, up to a cumulative radiation dose of 10^{11}Gy, the bulk of the glass network was unchanged.

The present investigation will find immense application in nuclear waste management in developing matrices for nuclear wastes for future reactors like PFBR (prototype fast breeder reactor) and AHWR (advanced heavy water reactor). The investigations on the radiation induced radicals/defect centres reported in the present thesis will serve as a valuable data base for formulations of matrices for futuristic wastes.

However, no single technique is sufficient to get all the required information. In addition to the techniques used in the present set of investigations, advanced synchrotron based techniques such as EXAFS (extended absorption fine structure spectroscopy) and XANES (X-Ray absorption near edge spectroscopy) can provide more insight into the radiation induced changes occurring in the matrices. Similarly, ESCA (electronic spectroscopy for chemical analysis) can provide in depth information in terms of the changes in the speciation of various metal ions in the glasses because of radiation. Moreover, there is a need to establish a one to one correlation in between the radiation induced changes in the waste glasses and it's leaching.

References:

1. Anil Kakodkar, "Shaping the third stage of Indian Nuclear Power Programme" presented at 12th annual conference of Indian Nuclear Society (INSAC-2001), Indore, India.
2. M. J. Plodinec, Glass Tech. 41 (2000) 186
3. M. I. Ojovan and W. E. Lee, New Development in Glassy Nuclear Waste forms. Nova Science Publishers, New York, 2007
4. C. M. Jantzen, K. G. Brown and J. B. Pickett, Int. J. Appl. Glass Sci. 1 (2010) 38–62
5. C.P. Kaushik, R.K. Mishra, P. Sengupta, A. Kumar, D. Das, G.B. Kale and K. Raj, J. Nucl. Mater. 358 (2006) 129
6. W.J.Weber, R.C.Ewing, C.A.Angell, G.W.Arnold, A.N.Cormack, J.M.Delaye, D.L.Griscom, L.W.Hobbs, A.Navrotsky, D.L.Price, A.M.Stoneham, M.C.Weinberg, J. Mater. Res. 12 (1997) 1946.
7. D.R. Neuville, L. Cormier, B. Boizot, A. Flank, J. Non-Cryst. Solids, 323 (2003) 207.
8. E. Malchukova, B. Boizot, G. Petite, D. Ghaleb, J. Non-Cryst. Solids 354 (2008) 3592.

9. M. I. Ojovan, W. E. Lee, J. Nucl. Mater. 335 (2004) 425.
10. N.Ollier, B.Boizot, B.Reynard, D.Ghaleb, G.Petite, Nucl. Inst. and Meth. B 218 (2004) 176
11. E. Malchukova, B. Boizot, G. Petite, D. Ghaleb, J. Non-Cryst. Solids 353 (2007) 2397
12. B. Boizot, G. Petite, D. Ghaleb, B. Reynard, G. Calas, J. Non-Cryst. Solids 243 (1999) 268
13. G.W.Arnold, Radiation damage effects in nuclear waste glasses, Radiat. Eff. 74 (1983) 151-159.
14. J. de Bonfils, G. Panczer, D. de Ligny, S. Peuget, B. Champagnon, Behaviour of simplified nuclear waste glasses under gold ions implantation: A microluminescence study, J. Nucl. Mater. 362 (2007) 480-484.
15. R.C. Ewing, W.J. Weber, F.W. Clinard, Radiation effects in nuclear waste forms for high level radioactive waste, Prog. Nucl. Energy 29 (1995) 63-127.

Publications in International Journals within the scope of the thesis

1. EPR investigations of electron beam irradiated Trombay waste base glass, **M.Mohapatra**, R.M.Kadam, B.S.Tomar, R.K.Mishra, C.P.Kaushik, S.V.Godbole, K.Raj and V.K.Manchanda, *IOP Conf. Series: Materials Science and Engineering* 2 (2009) 012022
2. Spectroscopic investigation of transition metal (Cr, Cu, Fe, and Mn) containing Trombay waste base glass, **M. Mohapatra,** R. M. Kadam, S. N.Tripathy, A. R. Dhobale, R. K. Mishra, C. P. Kaushik, B. S. Tomar, Kanwar Raj, S. V. Godbole & V. K. Manchanda, *Physics and Chemistry of Glasses* 51 (2010) 217
3. Photoluminescence investigations of rare earth (Eu and Gd) incorporated nuclear waste glass, **M. Mohapatra**, R.K.Mishra, C.P.Kaushik and S.V.Godbole, *Physica B* 405 (2010) 4790
4. Electron beam irradiation effects in Trombay nuclear waste glass, **M. Mohapatra**, R.M.Kadam, R.K.Mishra, D. Dutta, P.K.Pujari, C.P.Kaushik,

R.J.Kshirsagar, B.S.Tomar and S.V.Godbole, *Nuclear Instruments and Methods in Physics Research B* 269 (2011) 2057

5. Gamma radiation induced changes in nuclear waste glass containing Eu, **M. Mohapatra**, R.M.Kadam, R.K.Mishra, C.P.Kaushik, B.S.Tomar and S.V.Godbole, *Physica B* 406 (2011) 3980
6. Gamma radiation induced changes in Trombay nuclear waste glass containing Iron, **M.Mohapatra**, R.M.Kadam, R.K.Mishra, C.P.Kaushik, B.S.Tomar and S.V.Godbole, International Journal of Applied Glass Science 4 [1] 53–60 (2013)

7. Spectroscopic investigations of radiation damage in glasses used for immobilization of radioactive waste, **M.Mohapatra** and B.S.Tomar, Defects and Diffusion Forum 341 (2013) 107-128

Other related publications

1. Characterization of borosilicate glass as host matrix for high level waste, **M Mohapatra** and V.K.Manchanda, *IOP Conf. Series: Materials Science and Engineering* 2 (2009) 012006
2. Photoacoustic spectroscopic and electron paramagnetic resonance investigations on copper doped alkali borosilicate glasses, A R Dhobale, **M. Mohapatra**, R M Kadam, Mithlesh Kumar, C P Kaushik and S V Godbole, *IOP Conf. Series: Materials Science and Engineering* 2 (2009) 012044
3. Photoluminescence and photoacoustic investigations of U and Th in nuclear waste glass, A.R.Dhobale, **M. Mohapatra**, R.K.Mishra, C.P.Kaushik and S.V.Godbole, *International Journal of Applied Glass Science* 1 (2010) 322

Chapter-I

INTRODUCTION

Energy is essential for economic development and quality of life for any nation. A reasonably good correlation exists between the per capita energy consumption and the quality of life, as the former is a measure of UN Human Development Index. For the past two decades, energy demand has increased roughly by 2-3% per annum on global scale [1]. These figures are likely to move up with industrialization and modernization of our society. Especially in developing countries like India, where majority of the population are still out of the reach of industrialization, the energy demand is going to compound. Hence there is an urgent need to identify suitable energy resources for the future so that the required demand can be adequately met. Presently, 2/3rd of the energy demand in India is met by non-renewable sources such as coal, petroleum, natural gas etc. For a large country like India, a major fraction of energy must come from domestic resources. We have rather limited options in this regard from a long term perspective. There are environmental issues which will be inevitably associated with large-scale deployment of coal based power plants. Apart from this, a fact, which is often overlooked, is that the existing reserves of coal in our country would be inadequate to meet an enhanced rate of energy consumption, for more than a few decades. Currently lot of research and development work is going on in the fields of renewable energy sources such as solar, wind etc. However, estimates show that even under the best possible situation such energy sources may not be able to fulfill the demand. Hence, to bridge the gap between demand and supply, nuclear energy appears to be the best solution [2].

In case of nuclear fission based technology, enormous energy can be obtained either through bombardment of fissile and/or fertile radionuclides such as ^{235}U, ^{233}U, ^{239}Pu, ^{238}U, ^{232}Th etc., by slow or fast neutrons, which split them into lighter nuclei. India has already attained some maturity in this technology and currently >4700 MWe electricity is being produced from 20 nuclear reactors. As far as nuclear fusion energy sources are concerned, significant R&D initiatives have been taken by the Department of Atomic Energy and other national research centres. The International Thermonuclear Experimental Reactor (ITER) is a project being developed jointly by international consortium [3].

1.1. Indian Nuclear Energy Programme

The Indian nuclear power program has been conceived bearing in mind the optimum utilization of domestic uranium and thorium reserves with the objective of providing long-term energy security to the country. One of the essential elements of the Indian strategy is to enhance the fuel utilization using a closed fuel cycle. This entails reprocessing of the spent fuel to recover fissile and fertile materials and recycle them back into the system. Considering this objective, the indigenous nuclear power program in India was initiated with Pressurized Heavy Water Reactors (PHWRs) using natural uranium and heavy water, and based on pressure tube technology. In the second stage of the Indian nuclear power program, plutonium from the natural uranium-based PHWRs will be used in Fast Breeder Reactors (FBR) for multiplying the fissile base. Considering the large thorium reserves in India, the future systems, in the third stage of the program, will be based on natural thorium–^{233}U fuel cycle. A schematic diagram of closed nuclear fuel cycle is presented in figure 1.1.

1.2. Radioactive waste

Various types of nuclear waste are generated at every step of the nuclear fuel cycle. They are classified on the basis of their physical state as gaseous waste, liquid waste and solid waste. Amongst these wastes, liquid wastes need more attention due to their high volumes and mobility. Radioactive liquid waste streams are commonly classified as Exempted Waste, Low Level Waste (37-3.7×10^{6} Bq/L), Intermediate Level Waste (3.7×10^{6}- 3.7×10^{11} Bq/L) and High Level Waste (above 3.7×10^{11} Bq/L) [4].

The concentrations of long lived radionuclides and tritium are also taken into account while classifying the liquid wastes. The general categorization of radioactive waste is presented in Table 1.1. Out of all radioactive wastes generated in the entire nuclear fuel cycle, high level radioactive liquid waste (HLW) contains majority (~99% of total) of the radioactivity. As major share of radioactivity belongs to the HLW, the present thesis will focus on the materials used for fixing HLW.

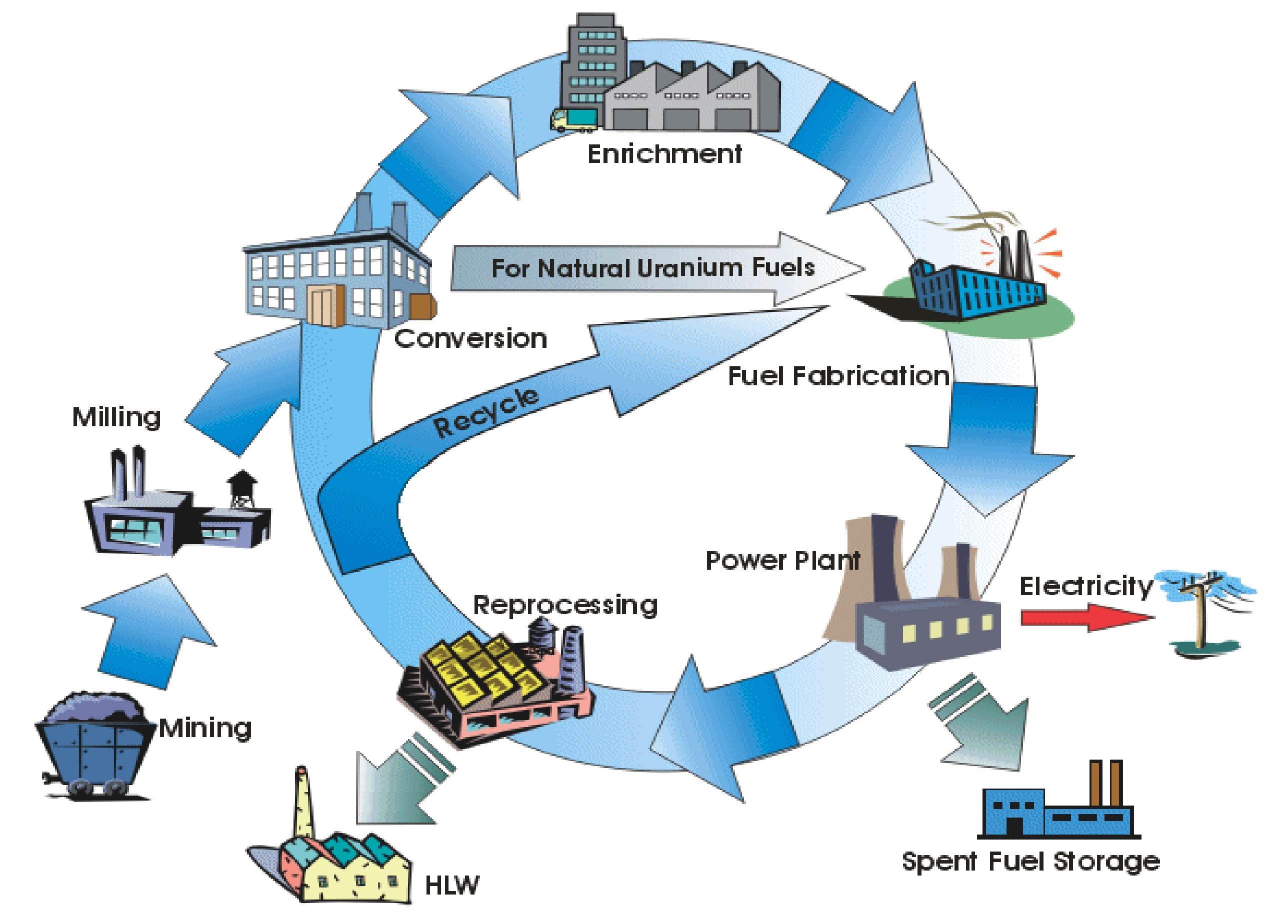

Figure 1.1 A schematic diagram of closed nuclear fuel cycle

Category	Solid	Liquid	Gaseous
	Surface Dose (mGy/hr)	Activity Level (Bq/m^3)	Activity Level (Bq/m^3)
I	<2	$< 3.7\times10^4$	< 3.7
II	2-20	3.7×10^4 to 3.7×10^7	3.7 to 3.7×10^4
III	>20	3.7×10^7 to 3.7×10^9	$> 3.7\times10^4$
IV	Alpha Bearing	3.7×10^9 to 3.7×10^{14}	
V		$>3.7\times10^{14}$	

Table-1.1: Categorization of radioactive waste

1.3. Principles of Radioactive Liquid Waste Management

The basic principles followed in liquid waste management are

- Delay and decay for the waste having short-lived isotopes,
- Dilution and dispersion to the environment of very low level activity well below the nationally accepted levels which are in line with international practices and
- Concentration and containment of radioactivity as much as practicable.

Amongst them concentration and containment is one of the widely adopted processes for managing HLW [5].

1.4. Sources of HLW

Reprocessing of the spent fuel is the major source of HLW. Reprocessing of the spent natural uranium oxide fuel from the PHWRs and research reactors involves its dismantling and dissolution in nitric acid. The liquid thus obtained contains uranium, plutonium, fission products, corrosion products, minor actinides etc. Solvent extraction process (PUREX process) is being routinely used to recover U and Pu from this liquid using 30% tri-butyl phosphate. During this process, major stream in the form of HLW is generated from the first cycle of the extraction scheme. The high active waste (HAW) is concentrated and is termed as HLW, as it contains around 99% of radioactivity of the spent fuel.

The major components of the HLW are as follows:

a) Minor actinides such as ^{237}Np, $^{241, 243}$Am, $^{242, 244, 245}$Cm

b) Unrecovered U and Pu

c) Fission products, such as, ^{90}Sr, ^{99}Tc, ^{106}Ru, ^{129}I, ^{135,137}Cs , ^{144}Ce, ^{147}Pm etc

d) Chemicals introduced in the reprocessing plant like nitric acid, sulphates, sodium nitrate, aluminum nitrate, chlorides, fluorides, traces of TBP and its degradation products,

e) Corrosion products of steel and other structural material (Fe, Ni, Cr, Mn etc),

f) Alloying elements such as Fe, Al, Si, Mo etc. in the fuel particularly when U metal is used as fuel,

g) Soluble poisons such as Gd, B and Cd.

Common radioisotopes present within HLW along with their respective half-lives are tabulated in Table 1.2. Table 1.2.B contains radionuclides which are of concern from the long term impact of the deep geological repository.

A-Relatively short half life			
Strontium-90	28 yrs	Cerium-144	1.3 yrs
Ruthenium-106	1 yr	Promethium-147	2.3 yrs
Cesium-137	30 yrs	Curium-244	17.4 yrs
B-Long Half-Life			
Technitium-99	$2x10^5$ yrs		
Iodine-129	$1.7x10^7$ yrs	Plutonium-240	6500 yrs
Neptunium-237	$1.6x\ 10^6$ yrs	Americium-241	440 yrs
Plutonium-238	85.3 yrs	Americium-243	7300 yrs
Plutonium-239	24360 yrs	Curium-245	8500 yrs

Table 1.2: Common radioisotopes present in HLW and their half-lives ($t_{1/2}$)

1.5. Management of HLW

The HLW generated after reprocessing, requires special treatment to ensure its isolation from human environment for extended period of time. Actinides present in HLW are mostly alpha active and have very long half lives and require isolation for longer time span compared to other radioactive fission and activation products. The philosophy of ‘concentrate and contain’ is used in managing this HLW. The strategy adopted all over the world for this purpose is to convert the liquid waste into some kind of suitable solid form (immobile form) which is chemically, mechanically and thermally stable over the life time of major long lived isotopes. The solid waste form is stored in an interim storage facility in natural air circulation to allow the decay of short lived radioisotopes (Table-1.2.A) and then buried in deep geological repositories.

Solidification provides improved safety during handling and shipping. Further, it minimizes the release of radioisotopes due to leaching with ground water in the deep repositories. The candidate matrix immobilizing the waste should be able to accommodate all the active and inactive components of the waste and bind them in the structure of the matrix so as to achieve the required isolation. The desirable properties of immobile matrix for fixation of high level waste forms are:

(i) Ability to incorporate a wide range of elements present in HLW.

(ii) Good chemical durability, i.e. low leachability.

(iii) Good thermal conductivity, so that the heat generated due to decay of radioactive isotopes is well dissipated.

(iv) Good thermal and radiation stability over extended periods of time.

(v) Good mechanical strength and shock resistance so that transportation to storage or disposal site is safe.

(vi) Minimum volume.

(vii) Compatibility with storage container.

(viii) Compatibility with geological repositories.

(ix) Technical and economical considerations (raw material availability, adaptability of process parameters to easily available engineering materials).

Many candidate matrices have been studied and developed for immobilization of HLW worldwide and characterized for aforesaid properties. These are briefly discussed here.

1.6. Candidate matrices for HLW

A. Glass based matrices

The most extensively studied and used waste forms are phosphate and borosilicate based glass and glass ceramics. Phosphate based glass systems were found attractive in early stages, as they can effectively incorporate molybdenum and sulphate present in the waste. The main additives of this glass form are in liquid form and formation temperatures of the system are comparatively low. However, material of construction is a major limitation in phosphate glass process because of severe corrosive conditions. Also the product, in general, is inferior from long term durability point of view.

Borosilicate based glass systems are now universally accepted as the matrix for immobilization of HLW on account of good product durability [6]. The pouring temperature is moderate being in the range of 1000 to 1100°C. However, elaborate glass forming additives are required either in the form of aqueous slurry of mixed oxides or glass frit.

Glass ceramics are obtained by controlled crystallization of the desired phases in bulk glass. In these types of matrices, the fission products and actinides of the waste can be accommodated into a desired crystalline phase. It can be prepared by annealing the glass product at a temperature of maximum nucleation rate. Once the nuclei are formed, a second annealing step is carried out at a temperature high enough to have maximum crystal growth. The product consists of continuous glassy phase with crystals homogeneously dispersed in it. For getting the fine grained product oxides facilitating nucleation such as TiO_2/ZrO_2 are normally added into the glass matrix. With the proper composition of base glass and schedule of nucleation, the desired crystals can be generated, where the fission products and actinides can be accommodated. In general, the glass ceramics are mechanically more stable than the glass; however accommodation of particular element into a desired crystalline phase uniformly throughout the glassy phase is difficult.

B. Crystalline matrices

(i) Ceramic Waste Forms

Ceramic nuclear waste forms are attractive alternative to glass based nuclear waste form since they are thermodynamically more stable and have better chemical durability. The ceramic waste form such as supercalcine, synthetic rocks (SYNROC), sodium zirconium phosphate (NZP), sodium zirconium tungstate etc. are considered as suitable crystalline matrices for immobilization of HLW. Pyrochlores ($A_2B_2O_7$) are also being contemplated as potential ceramic waste form.

Supercalcine is an alumino-silicon product of the ceramic type produced by tailored additions of Al_2O_3, SiO_2, CaO etc. into the liquid waste. Such types of supercalcines however have higher leaching rates than glass.

SYNROCs are titanate based crystalline forms comprising of phases like hollandite

($BaAl_2Ti_6O_6$), perovskite ($CaTiO_3$), zirconolite ($CaZrTi_2O_7$), Ba-feldspar ($BaAl_2Si_2O_8$), kalsilite ($KAlSiO_4$), leucite ($KAlSi_2O_6$) etc. depending on the precursor used. Normally the precursors, such as TiO_2, CaO, ZrO_2, BaO, Al_2O_3, SiO_2 etc are used. In general, the hollandite phase accommodates the elements like Mo^{4+}, Ru^{4+}, Rh^{3+}, Fe^{3+}, Fe^{2+}, Cr^{3+}, Ni^{2+}, K^+, Cs^+, Rb^+, Na^+ etc., the zirconolite phase accommodates the elements like U^{4+}, Th^{4+}, Cm^{3+}, Am^{3+}, Y^{3+}, Ln^{3+} etc. and the perovskite phase accommodates elements like U^{4+}, Th^{4+}, Pu^{4+}, Cm^{3+}, Am^{3+}, Y^{3+}, Ln^{3+}, Sr^{2+} etc [7].

C. Other matrices

Other matrices such as calcines, coated particles and metal matrix products are also potential candidates for waste immobilization. Calcines are produced by dehydration and de-nitration of the waste with no appreciable addition of other chemicals. Since the product has appreciable solubility in water, it is not considered suitable for long term disposal, but considered as intermediate product during its final solidification [8].

Coated particles are produced as a multi-barrier development concept. In this process, HLW is converted into spherical agglomerates of supercalcine powder in the form of 1-5 mm size range. Thereafter they are coated with an impervious layer of alumina and/ or pyrolytic carbon for added leach resistance. This gives enhanced inertness and improvement in thermal stability, mechanical strength and leachability. In the metal matrix process, the HLW is immobilized in glass matrix and then embedded in metal matrix like lead to enhance the thermal conductivity of the final product [9]. For example, vitromet consists of waste containing glass beads encapsulated in a matrix of 99% Pb-1 % Sb alloy.

Similarly HLW can be converted to a supercalcine or to a sintered ceramic and then embedded in a metal matrix. This type of matrix will be very important for immobilization of fresh HLW, where container centerline temperature must be kept within a reasonable limit as thermal conductivity of this matrix is considerably high.

1.7. Glass – a candidate waste form for immobilization of HLW

Out of all the listed waste forms, glass has received major attention in product development as well as in long term product characterization with respect to the desired waste form characteristics. It is now the material of choice for incorporating and immobilizing the potentially hazardous radionuclides in HLW. The typical material properties, which make it superior as compared to others include (i) structural flexibility to accommodate wide range of elements (ii) simplicity in processing technique (iii) high corrosion resistance (iv) good thermal and radiation stability (v) high volume reduction during immobilization (vi) established long term integrity and (vii) inexpensive raw materials.

These characteristic properties of the glass make vitrification the focal point of systems for treatment of HLW around the world. Borosilicate based glasses have been studied in detail and have found wide acceptance in the world as one of the suitable matrices having capability to retain radioactivity for long duration. However, the glass composition varies with the composition of the respective HLW, which in turn depends on the type of reactor, burn up, off reactor cooling of spent nuclear fuel and nature of reprocessing flow sheets etc. Although the basic network is of silicon and boron oxides, other modifiers are necessary to take into account site specific variations in HLW composition [10].

1.8. Glass structure

Glass is an inorganic product of fusion (chemical reaction) which has been cooled under rigid conditions of temperatures without crystallization. It is a rigid, non crystalline (amorphous) material. The open random structure of glass is primarily responsible for achieving high waste loading and high chemical durability. The radionuclides from the nuclear waste are contained in a glass through primary and/or secondary bonding with the silicate network. This inherent property leads to the incongruent release of different elements from a waste glass. The network structure of glasses precludes the description of their composition in sample chemical formulae. The most common way of describing glass is to list relative amount of oxides derived from the raw materials used in the glass formulation even though these oxides do not exist as it is in the glass network. Another advantage of glasses over ceramic waste form is that they do not have any crystallographic limits for incorporation of waste.

According to Zachariasens' view of atomic arrangement, the oxides involved in the glass formations can be categorized as follows [11].

a) ***Network formers*** – Oxides of elements that can produce glasses by forming chains and networks in a completely random manner. The elements of these oxides have a co-ordination number of four. The inorganic species increase the network connectivity by covalent bonds with the oxygen atoms in a silicate network. Generally network formers are acidic (e.g. SiO_2, B_2O_3 etc.) in nature.

b) ***Network Modifiers*** **–** Oxides of elements that can produce glasses by melting with network formers. The inorganic species interrupt the network continuity by forming ionic bonds with the oxygen or other elements in the glass network. Generally glass network modifiers are basic (e.g. Na_2O, K_2O, Li_2O, BaO, CaO) in nature.

c) ***Intermediates* –** These are oxides of elements that can produce glasses by fusion with network formers. The elements of these oxides have co-ordination number in between those of glass formers and glass modifiers. Intermediates can also act like network formers. In some instances, intermediates are referred to as dwellers. Generally, intermediates are amphoteric (e.g. Al_2O_3, Fe_2O_3 etc) in nature.

An oxygen atom involved in interconnecting either two network forming elements or a network forming and a network dwelling element is regarded as bridging oxygen (BO). Chemical durability of the glass increases with increase in the BO, since they help to maintain the network continuity. In general, the bridging oxygens bind covalently to both the network formers and dwellers. A non bridging oxygen (NBO) can be defined as an atom interconnecting the network forming and network modifying elements. In general the NBO's bond covalently with formers and ionically with the modifiers. However, due to the electrostatic nature of the ionic bond, NBOs fail to retain network continuity and hence affect the glass durability adversely [12].

Hazardous constituents of the waste can be immobilized in the vitrification process either by their participation in glass formation (as network former), chemical bonding (network modifier) or encapsulation. Random network structure (two dimensional) of vitrified waste product is shown in figure 1.2.

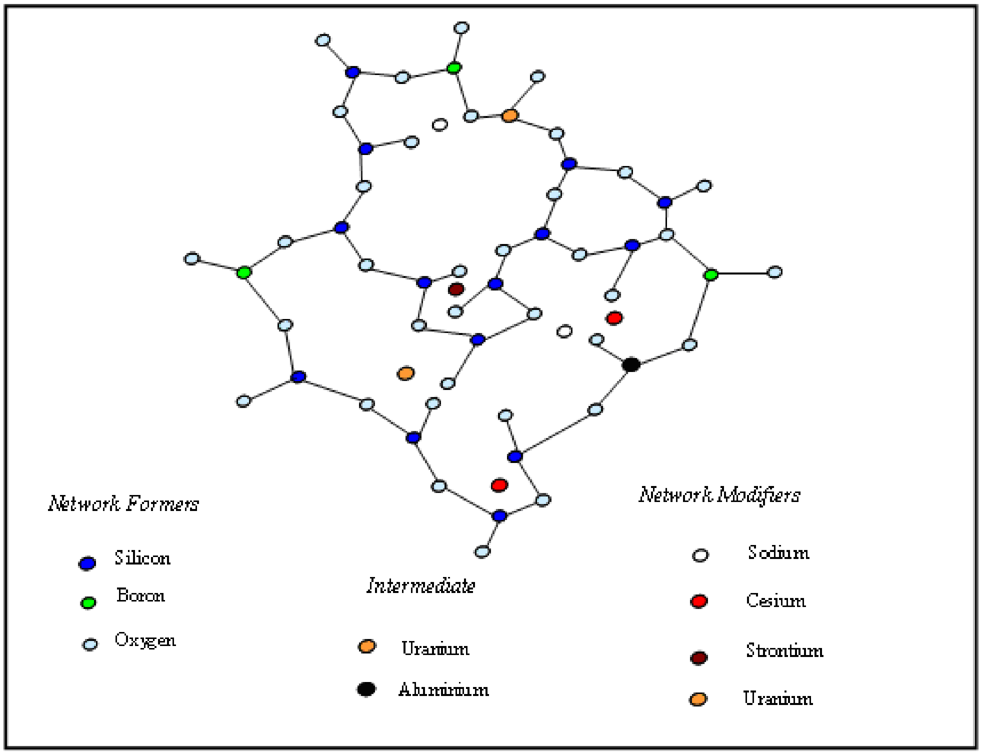

Constituent present in waste streams can themselves serve as primary glass formers and modifiers	**Proportioning of these different waste streams with minimum external additives can result in optimized vitreous waste forms**

Figure 1.2. Random network structure of vitrified waste product

Certain waste constituents can be immobilized by chemical bonding with the glass forming materials, particularly silica present in the wastes. The most notable chemical bonding within vitrified materials occurs, when waste constituents bond covalently with the oxygen atoms in a silica network and become part of the network. Waste constituents like U, Fe, Al etc. that interact this way, behave like network formers since they essentially replace silicon in the glass network structure. Other waste constituents can bond chemically with oxygen or other elements in the glass network. To sum up the above discussion, it is understood that ionic bonding incorporates the material into the glass but disrupts the network continuity thereby modifying the physical and chemical properties of the vitrified materials. Materials, which interact in this fashion, are called network modifiers. Hazardous waste constituents may also be immobilized without direct chemical interaction with the glass network. Since vitrification constitutes a molten phase at some stage of the process, materials that do not interact chemically or have not completely entered the solution can be surrounded by a layer of vitrified material and thus get encapsulated, as the melt cools. This layer of vitrified material protects the capsulated constituents from the chemical attack. This structural characteristic of the glass providing three routes for immobilization of waste constituents make vitrification as the focal point of immobilization of HLW.

1.9. Glass composition for Indian nuclear reactors

In India, work on conditioning of HLW in borosilicate matrices was started in early seventies. For HLWs generated from uranium fuel cycle (PHWR), sodium borosilicate glass matrix containing TiO_2, MnO, BaO etc. are used for vitrification**.** On the other hand, suitable glass formulations for thorium rich HLWs, which are likely to be generated during reprocessing of spent fuel containing thorium (from AHWR), are yet to be developed [13].

The HLW from reprocessing plant at Trombay is characterized by the presence of high amounts of sulfate ions and sodium along with fission and activation products, corrosion products and actinides. Sulfate in the waste is derived from ferrous sulfamate [$Fe(NH_2SO_3)_2$] used as reducing agent for conversion of Pu^{4+} to Pu^{3+} at partitioning stage of the reprocessing and is one of the troublesome constituents with respect to vitrification in view of its limited solubility in the glass matrix. To deal with this, a barium oxide containing alkali borosilicate glass has been developed and is routinely used for the waste immobilization [14]. The quaternary system of BaO-Na_2O-B_2O_3-SiO_2 referred to as the base glass is found to be suitable to deal the problem of sulfate ions forming a separate phase without affecting the waste oxide loading.

1.10. Radiation induced changes in nuclear waste glasses

As discussed earlier, the HLW contains most of the radioactivity generated during reactor operation. Because of the radioactive components present in the HLW, the glass experiences constant irradiation with α, β and γ radiations. Numerous literature reports are available in the field of radiation induced changes in nuclear waste glass. Major work in this area has been carried out at several laboratories in the USA such as the Pacific Northwest National Laboratory by Weber and his colleagues [15], at Argonne National Laboratory [16] and Naval Research Laboratory [17]. Similar work was also initiated at CEA in France [18-20] and at the Kyushu University and Kyoto University in Japan [21]. In UK, at the University of Sheffield, radiation damage studies of nuclear waste glasses have also been carried out along with leaching studies [22-24]. Among these literature reports, a majority of the work is related to the electron beam irradiation of the waste glasses. This is understandable, because for the first few years, the β decay plays a predominant role in radiation induced changes. Electron beam irradiations can simulate the effects of beta irradiation in the waste glasses to a great extent if not in totality. Boizot et al. have studied the electron beam irradiated French nuclear waste glasses by Raman spectroscopy and confirmed the migration of alkali metal ions in the glass [19, 25]. Similar alkali ion migration in electron beam irradiated glasses was previously also reported by Usher [26]. Ollier et al. have also studied the irradiated French waste glass to analyze the formation of molecular oxygen in it [27]. This was done by Raman depth profiling technique using micro

Raman spectroscopy. In another report the authors have investigated the microstructure evolution in the irradiated waste glasses by incorporating Cr^{3+} ions as a luminescence and EPR probe [28]. The role of mixed alkali effect on the radiation damage of these glasses gave also been reported by this group [29]. Apart from trivalent chromium, many rare earth ions have been used as local structural probes to understand the beta radiation damage in the nuclear waste glasses viz the reports by Malchukova et al. where the trivalent rare earth ions, Gd^{3+}, Eu^{3+} and Sm^{3+} have been used as local structural probes to monitor the radiation damage in the glasses [30-33]. On similar lines, Ollier et al. have reported electron beam irradiation induced changes in the Yb^{3+} and Sm^{3+} doped waste glasses [34, 35]. In the rare earth doped glasses, it was observed that, both the oxidation states and the coordination geometries of the ions are affected by irradiation. In some cases, the formation of unusual oxidation states of the metal ions has also been observed. Several other reports suggest a modification in the borosilicate/ silicate network upon beta irradiation e.g. the reports by Buscarino et al. [36], Antonini et al. [37], Boizot et al. [38, 39] and Yang et al. [40].

Although for the first few years, the beta decay is primarily responsible for the radiation damage, in order to understand completely the damage in the glass matrix, one can not ignore the effect of gamma radiation. Further, gamma rays with higher penetrating power than the beta particles can create effects uniformly throughout the glass. Formation of defect centers along with changes in the oxidation states and coordination numbers is the main out come of the studies on gamma irradiation of the waste glasses. El Batal et al. have studied several gamma irradiated glasses in order to characterize the radiation induced changes [41, 42]. Durability and the modification in gamma irradiated borate, silicate and borosilicate glasses have also been reported by many researchers [43-47]. Like in the case of electron beam irradiated glasses, gamma irradiated glasses incorporated with several rare earth and transition metal ions as local probes have been used to study the radiation induced changes. Baccaro et al. have reported the gamma radiation induced changes in silicate glasses incorporated with trivalent Ce, Tb and Eu [48, 49]. Gamma radiation induced changes in Sm incorporated waste glasses have been reported by Malchukova et al. [50]. Recently McGann et al. have reported an exhaustive study on the gamma radiation effects on simulated waste glasses of varying composition [51].

Apart from the gamma and beta damages occurring in the glass, the changes caused by the alpha particles and the resulting recoiled nuclei is of prime concern. In fact, majority of the atom displacements occurring in the vitreous waste form are due to recoil nuclei [52]. External heavy ion irradiation is a convenient laboratory technique for simulating the alpha damages in the borosilicate glasses from radioactive waste encapsulation point of view [53]. One can find many reports in the literature where heavy ion irradiation studies have been done on nuclear waste glasses to assess the effects of alpha decay on the structural properties of the glass matrix. There are number of reports by de Bonfils et al. on heavy ion (particularly gold) irradiated waste glasses having analogous composition to that of the French waste glass [54, 55]. In some other reports, incorporation of alpha particles in the glass matrix, either in the form of ion beam (viz ^{4}He beam) or direct incorporation of actinides have been described [56-60]. Matzke had incorporated ^{244}Cm in glass as well as SYNROC to simulate the alpha damages [61]. The same group also carried out ion implantation in the matrices at different temperatures to compare the effects [62]. Effect of different ion implantation in alkali borosilicate glasses have also been investigated by Arnold [63], who bombarded the borosilicate glasses with ‘He’, ‘Ar’ and ‘Xe’ ions and investigated the radiation induced damage. In another report ‘Kr’ ions have also been used to bombard the nuclear waste glasses and investigate the radiation damage [64]. Proton beam irradiation of silicate glasses have been carried out by Kudo et al. [65], who used micro fluorescence and EPR techniques to study the radiation induced damages in the glasses. Sato et al. irradiated simulated waste glasses by electron beam, gamma rays and heavy ions to investigate the radiation damage [66]. The change in the glass density as a function of irradiation has been measured by the authors as a function of ion-fluence using electron microscope.

Most of these studies have shown that the nuclear waste glasses upon irradiation by high-energy gamma rays, electron beams and heavy ions undergo changes in their structure. These changes are caused mostly by the ionization and ballistic interaction of high-energy radiation with solid constituents of the glass matrix, that introduce disorders in the original structure causing formation of defect centers accompanied with volume changes, phase separation or gas accumulation in the irradiated glasses [67-70]. It is pivotal to study these changes so as to predict the long term leaching behavior of the vitrified waste product. Moreover, it is well known that the optimal engineering performance of a glass is dominated by its structure. So, the knowledge of the glass structure before and after irradiation is a prerequisite for understanding the structural evolution of glasses under long term irradiation. In addition, these studies on the borosilicate glasses will lead to an understanding of the nature of the damage which can further lead to fabrication of materials in which the deleterious effects of radiation can be minimized. Moreover, careful study of radiation induced defects can help elucidate certain structural aspects of the glassy state which cannot be readily accessible by other means.

1.11. Spectroscopic techniques to study the radiation induced changes

Spectroscopic techniques provide non-invasive and direct methods for characterizing glass samples before and after irradiation. Through these techniques one can obtain extensive information with minimal sample handling. In literature one can find various spectroscopic techniques being used for these investigations. As no single spectroscopic technique is capable of answering all the questions related to the radiation damage of glasses, use of multiple techniques becomes imperative. For example, Electron Paramagnetic Resonance (EPR) can give information regarding the chemical nature of defect centers formed in the irradiated glass and quantify them. On the other hand, FTIR (Fourier Transform Infra Red) can give information about the changes in the bulk glass network. In the present set of investigations, conventional photon based techniques such as UV-Vis absorption, Photoacoustic spectroscopy (PS), Photoluminescence spectroscopy (PL), FTIR and Raman spectroscopic techniques were used along with novel techniques like positron annihilation spectroscopy (PAS) and EPR.

1.12. Motivation for the present work

As discussed above, keeping in view the high sulphate ion content in the stored HLW from Trombay reprocessing plant, a special glass formulation has been developed [14]. This alkali barium borosilicate glass formulation has been observed to tackle the problem of separate phase formation of sulphate ions quite effectively. In view of this, it is being routinely used for vitrifying the stored HLW. After vitrification, these wastes are to be stored for an interim period of 30-50 years under surveillance after which these are proposed to be buried in a deep geological repository. However, these glass matrices have not been characterized from radiation damage point of view, which is essential for predicting their long term integrity. In the present doctoral work, the alkali barium borosilicate glasses with and without dopant ions were characterized before and after irradiation. Suitable local structural probes were introduced in the glass to monitor radiation induced structural changes in the glasses due to irradiation. Different types of radiation sources such as gamma rays, electron beam and heavy ion beam were used for the irradiation. The free volume and defect centers formed in the glass were characterized by different spectroscopic techniques. It was observed that, the bulk of the glass remains unaffected even at a high dose of 10^{11} Gy(J/kg).

The following issues are taken up during execution of this research work

a) Speciation studies (determination of oxidation states and coordination geometry) of different metal ions expected to be present in the waste glass. As the oxidation states predict the solubility of a particular species, these studies have direct relevance to the solubility limit of the metal ion in the glass.

b) Characterization of the waste glass after gamma irradiation in terms of various defect centers and radicals formed.

c) Use of Eu^{3+} as a local probe in the glass to study radiation damage.

d) Role of ‘Fe’ in the radiation damage in glass.

e) Electron beam irradiation effects on the glass to simulate the effects of beta decay.

f) Quantification of the defects formed in the glass after radiation damage.

g) Effect of heavy ion irradiation on the glasses.

References

1. "Blue print for Power Sector Development", Ministry of Power, Govt. of India, (2001).
2. World Nuclear Association Report, "Nuclear power in India", Oct. (2008).
3. A. Kakodkar, "Indian nuclear power programme- Materials Challenges", Proc. Inter. Symp. on Energy Related Materials, Mumbai, India (2007) 1.
4. K.Raj, K.K.Prasad, N.K.Bansal, Nucl. Engg. Design 236 (2006) 914.
5. Atomic Energy Regulatory Board (2003), "Safety Code on Establishing Radioactive Waste Management System", Department of Atomic Energy, India.
6. M. J. Plodinec, Glass Tech. 41 (2000) 186.
7. ERDA (Energy Research and Development Agency),"Alternatives for managing waste from reactors and post fission operations in the LWR fuel cycle", 2 (1976) 14.
8. D.M.Roy, W.Fajun and M.W.Grutzeck, 1984, Nuclear Waste Management, in: Advances in Ceramics, Vol. 8, Chicago, (1983) Editors, G.G. Wicks and W.A.Ross (American Ceramic Society, Columbus, Ohio, USA) p. 401.
9. G. J. Mc Carthy, Nucl. Technol. 32 (1977) 92.
10. C. M. Jantzen, K. G. Brown, J. B. Pickett. Int. J. App. Glass Sci. 1 (2010) 38
11. W.H. Zachariasen, J. Am. Chem. Soc. 54 (1932) 3841.
12. Vitrification Technologies for treatment of Hazardous and radioactive waste, May 1992, EPA/625/R-92/002 Rev.00, prepared for office of Research and Development, Washington, DC.
13. V.S. Yalmali, D.S. Deshingkar, P.K. Wattal and S.R. Bharadwaj, J. Non Cryst Solids 353 (2007) 4647–4653

14. C.P. Kaushik, R.K. Mishra, P. Sengupta, Amar Kumar, D. Das, G.B. Kale, Kanwar Raj, J. Nucl. Mater. 358 (2006) 129.
15. W.J. Weber, Nucl. Instrum. And Meth. B32 (1988) 471.
16. I. A. Shkrob , B. M. Tadjikov, A. D. Trifunac, J. Non Cryst Solids 262 (2000) 6.
17. D.L.Griscom, J. Non Cryst Solids, 13 (1973/74) 251
18. E. Malchukova, B. Boizot, G. Petite, D. Ghaleb, J. Non Cryst Solids 354 (2008) 3592
19. B. Boizot, G. Petite, D. Ghaleb, N. Pellerin, F. Fayon, B. Reynard, G. Calas, Nucl. Instrum. And Meth. B 166/167 (2000) 500
20. J. de Bonfils, S. Peuget, G. Panczer, D. de Ligny, S. Henry, P.-Y. Noël, A. Chenet, B. Champagnon, J. Non Cryst Solids 356 (2010) 388
21. S. Sato, F. Hirotaka, K. Asakura and K. Ohta, Nucl. Instrum. And Meth. B l (1984) 534
22. G. Möbus, M. Ojovan, S. Cook, J. Tsai, G. Yang, J. Nucl. Mater.396 (2010) 264
23. J.M. Juoi, M.I. Ojovan, W.E. Lee, J. Nucl. Mater. 372 (2008) 358
24. M. I. Ojovan, W. E. Lee, J. Nucl. Mater. 335 (2004) 425
25. B. Boizot, G. Petite, D. Ghaleb, B. Reynard, G. Calas, J. Non-Cryst.Solid 243 (1999) 268
26. D. M. Usher, J. Phys. C: Solid State Phys., 14 (1981) 2039.
27. N. Ollier, B. Boizot, B. Reynard, D. Ghaleb, G. Petite, J. Nucl. Mater. 340 (2005) 209
28. N. Ollier, B. Champagnon, B. Boizot, Y. Guyot, J. Non-Cryst.Solid 323 (2003) 200
29. N. Ollier, B. Boizot, B. Reynard, D. Ghaleb, G. Petite, Nucl. Instrum. And Meth. B 218 (2004) 176
30. E. Malchukova, B. Boizot, D. Ghaleb, G. Petite, J. Non-Cryst. Solids 352 (2006) 297
31. E. Malchukova, B. Boizot, G. Petite, D. Ghaleb, J. Non-Cryst. Solids 354 (2008) 3592
32. E. Malchukova, B. Boizot, Mater. Res. Bull. 45 (2010) 1299

33. E. Malchukova, B. Boizot, G. Petite, D. Ghaleb, J. Non-Cryst. Solids 353 (2007) 2397
34. N. Ollier, B. Boizot, P. L'henoret, S. Guillous, G. Petite, J. App. Phys. 105 (2009) 113515
35. N. Ollier, J.-L. Doualan, V. Pukhkaya, T. Charpentier, R. Moncorgé, S. Sen, J. Non-Cryst. Solids, 357 (2011) 1037
36. G. Buscarino, S. Agnello, F. M. Gelardi, R. Boscaino, Phys. Rev. B 80 (2009) 094202
37. M. Antonini, A. Manara, S.N.Buckley, S.N.Manthorpe, J. Phys. Chem. Solids 46 (1985) 281
38. B. Boizot, N. Ollier, F. Olivier, G. Petite, D. Ghaleb, E. Malchukova, Nucl. Instrum. And Meth. B 240 (2005) 146
39. B. Boizot, G. Petite, D. Ghaleb, G. Calas, Nucl. Instrum. and Meth. B 141 (1998) 580
40. G. Yang, G. Möbus, P. A. Bingham, R. J. Hand, Phys. Chem. Glasses: Eur. J. Glass Sci. Technol. B, 50 (2009) 378
41. F.H.El Batal, N.Nada, S.M.Desouky, M.M.I.Khalil, Ind.J.Pure Appl.Phys.42 (2004) 711
42. F.H. El Batal, A.A. El Kheshen, M.A. Azooz, S.M. Abo-Naf, Opt. Mater. 30 (2008) 881
43. N. A. El-Alaily, F. M. Ezz-Eldin, H. A. El-Batal, Radiat. Phys. Chem. 44 (1994) 45
44. A K Sandhu, S Singh, O P Pandey, J. Phys. D: Appl. Phys. 41 (2008) 165402
45. M.M. Morsi, S. El-Konsol, M.A. Adawi, J. Non-Cryst. Solids 58 (1983) 187
46. S. Baccaro, N. Catallo, A. Cemmi, G. Sharma, Nucl. Instrum. and Meth. B 269 (2011) 167
47. T. Tsuboi, Eur. Phys. J. Appl. Phys. 26 (2004) 95
48. S. Baccaro, A. Cecilia, M. Montecchi, M. Nikl, P. Polato, J. Non-Cryst. Solids 315 (2003) 271
49. S. Baccaroa, A. Cecilia, E. Mihokova, M. Nikl, K. Nitsch, P. Polato, G. Zanella, R. Zannoni, Nucl. Instrum. and Meth. A 476 (2002) 785
50. E. Malchukova, B. Boizot, D. Ghaleb, G. Petite, Nucl. Instrum. and Meth. A 537 (2005) 411

51. O. J. McGann, P. A. Bingham, R. J. Hand, A. S. Gandy, M. Kavčič, M. Žitnik, K. Bučar, R. Edge, N. C. Hyatt, J. Nucl. Mater. (2012) doi: 10.1016/j.jnucmat.2012.04.007.
52. Hj. Matzke, Nucl. Instrum. and Meth. B 65 (1992) 30
53. G.W.Arnold, Radiat. Eff. 74 (1983) 151
54. J. de Bonfils, S. Peuget, G. Panczer, D. de Ligny, S. Henry, P.-Y. Noël, A. Chenet, B. Champagnon, J. Non-Cryst.Solid 356 (2010) 388
55. J. de Bonfils, G. Panczer, D. de Ligny, S. Peuget, B. Champagnon, J. Nucl. Mater. 362 (2007) 480
56. A. Abbas, Y. Serruys, D. Ghaleb, J.M. Delaye, B. Boizot, B. Reynard, G. Calas, Nucl. Instrum. and Meth. B 166/167 (2000) 445
57. J.M. Costantini, C. Trautmann, L. Thomé, J. Jagielski, F. Beuneu, J. App. Phys. 101 (2007) 073501
58. S. Peuget, J.-N. Cachia, C. Je´gou, X. Deschanels, D. Roudil, V. Broudic, J.M. Delaye, J.-M. Bart, J. Nucl. Mater. 354 (2006) 1
59. R.A.B. Devine, Nucl. Instrum. and Meth. B 91 (1994) 378
60. A. Haddi, P. Trocellier, I. Draganic, F. Farges, S. Poissonnet, P. Bonnaillie, Nucl. Instrum. and Meth. B 266 (2008) 3182
61. Hj. Matzke, Nucl. Instrum. And Meth. B 32 (1988) 455
62. Hj. Matzke, G. Della Mea, J.C. Dran, G. Linker, B. Tiveron, Nucl. Instrum. And Meth. B 46 (1990) 256
63. G. W. Arnold, Radiat. Eff.98 (1986) 55
64. P. Trocellier, A. Haddi, S. Poissonnet, P. Bonnaillie, Y. Serruys, Nucl. Instrum. And Meth. B 249 (2006) 145

65. H. Kudo, T. Akagawa, Y. Katsumura, Nucl. Instrum. And Meth. B 245 (2006) 201

66. S. Sato, H. Furuya, K. Asakura, K. Ohta, T. Tamai, Nucl. Instrum. And Meth. B 1 (1984) 534

67. R. C. Ewing, W. J. Weber, F. W. Clinard, Prog. Nucl. Energy 29 (1995) 63.

68. D.R. Cousens, S. Myhra, J. Non-Cryst.Solid 54 (1983) 345.

69. D.R. Neuville, L. Cormier, B. Boizot, A. Flank, J. Non-Cryst. Solids, 323 (2003) 207.

70. W.J.Weber, R.C.Ewing, C.A.Angell, G.W.Arnold, A.N.Cormack, J.M.Delaye, D.L.Griscom, L.W.Hobbs, A.Navrotsky, D.L.Price, A.M.Stoneham, M.C.Weinberg, J. Mater. Res. 12 (1997) 1946.

Chapter- II

Experimental Techniques

2.1 Introduction

This chapter describes briefly the method of preparation of the glass samples and their characterization by different spectroscopic techniques. Powder X-ray diffraction (XRD), UV-Visible Spectroscopy, Photoacoustic Spectroscopy (PS), Photoluminescence (PL), Electron Paramagnetic Resonance (EPR), Positron Annihilation Spectroscopy (PAS), Fourier Transform Infrared spectroscopy (FTIR) and micro Raman spectroscopic techniques have been used to investigate the borosilicate glass samples before and after irradiation.

XRD technique was used for characterization of samples with respect to homogeneity whereas UV-Vis Spectrophotometry and PS techniques were used for studying the speciation of metal ions. PL and EPR studies were done in order to identify the defect centers formed in the glass samples because of irradiation. PAS studies helped us identify the changes in the free volume size and fraction due to irradiation. FTIR and Raman spectroscopic techniques gave information about the changes in the bulk glass network due to irradiation.

2.2 Glass preparation

All the glass samples were prepared by conventional melt quenching technique at Waste Management Division (WMD), BARC. All the chemicals used were of AR grade and procured locally. For effective mixing and reaction among different constituents, the reactants were thoroughly ground and subjected to different heating steps depending on the type of glass, prior to final melting and quenching process. Specific details of the method of preparation of various glass samples are given in the relevant chapters.

2.3 Characterization Techniques

I. X-ray Diffraction (XRD)

XRD is one of the simplest and most widely used techniques to confirm the formation of glassy phase. In crystalline materials, due to the presence of long range periodicity, the XRD patterns are in the form of sharp peaks. For glasses, the diffraction pattern is characterized by a broad and continuous peak. This is because glasses do not possess long range periodicity, and there is considerable distribution in the bond angles and bond lengths between the constituent atoms present in the glass.

In this study, the glass samples prepared were checked for their amorphous nature by XRD. Glass samples prepared by standard melt quench method were ground in agate mortar and sieved through 200 mesh (ASTM) to get uniform particle size. This sieved powder was spread over a perspex sample holder and scanned by XRD. A 2θ scanning speed of 1^{o} per minute (θ is Bragg angle) was employed and samples were scanned in the range of 10^{o} to 70^{o} with an accuracy of 0.02^{o}.

The principle of XRD technique is based on scattering of X-rays by a crystal consisting of well-defined array of atoms, ions and molecules. Since the crystal lattice consists of parallel arrays of atoms equivalent to the parallel lines of the diffraction grating, the inter-planar spacing could be successfully determined from the separations of bright fringes of the diffraction pattern. These interplanar spacings (or distances) are of the same magnitude as the wavelength of X-rays (0.5 to 2 Å) and hence crystal planes act as diffraction gratings. Interaction of X-rays reflected by a set of parallel planes satisfying Bragg′s condition lead to constructive interference only at a particular angle. The Bragg condition for the occurrence of such diffraction can be written as:

$$\boldsymbol{n\lambda = 2d \sin\theta} \qquad \textbf{(1)}$$

where,

λ is the wavelength of X-rays,

θ is the glancing angle (called as Bragg′s angle),

d is the inter-planar separation and

n is the order of diffraction

X-rays being electromagnetic radiations, interact with the electron cloud of the atom. The electron clouds at the lattice points act as scattering centers and the two scattered X-rays from two centers may have constructive or destructive interference depending on equation 1.

The main steps covering the details of the techniques are described as follows

Instrumental details

A typical classical powder X-ray diffractometer consists of a source of X-ray and a detector for the detection of diffracted X-rays. Common diffractometer geometries are based on the Bragg-Brentano geometry. A block sketch of the typical powder diffractometer is shown in the Figure.2.1.

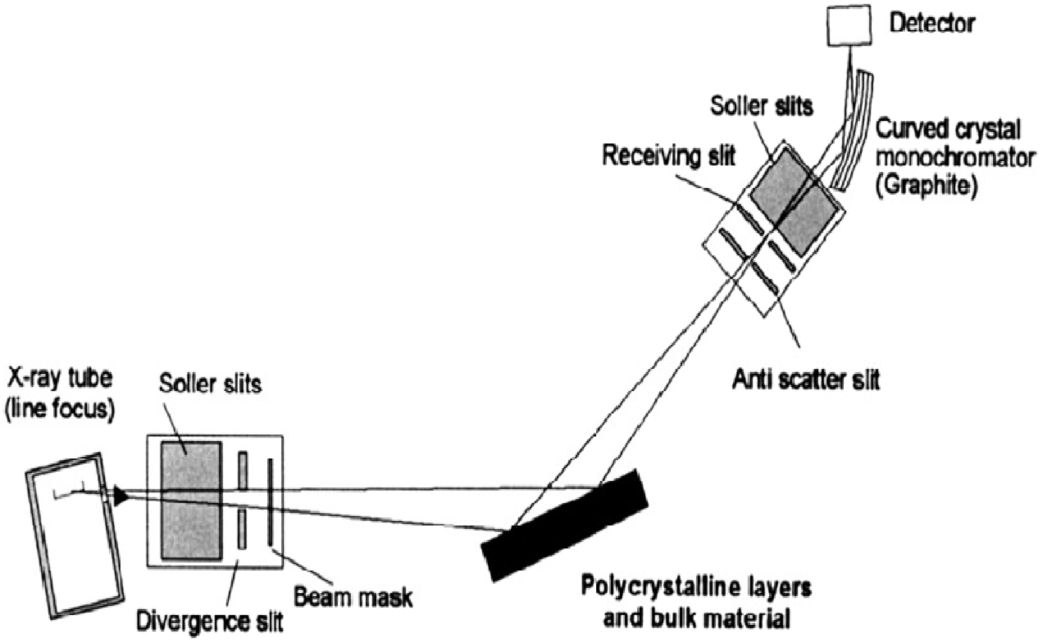

Figure. 2.1: A schematic diagram of a typical X-ray diffractometer.

Several kinds of sources are available for X-ray, but the most common laboratory diffractometers use sealed tube X-ray source. The basic construction of the tube is similar to the Coolidge tube. The X-rays are produced by bombarding high-speed electrons on a metal target. A part of the electron energy is used in producing X-ray beam, which is a combination of a continuous radiation with wavelength ranging from a particular shortest value (λ_{swl}) onwards and several intense spikes, which are characteristics of the target elements (called characteristic radiation). The intense continuous radiations or the monochromatic wavelength radiations can be used for the diffraction experiments. The latter is used in the most common diffraction instruments (angle dispersive). The details of the X-ray production and the typical X-ray spectra are explained in several monographs [1, 2]. The X-rays are produced in all directions; but are allowed to escape from a particular direction (usually from beryllium window) for experiments. The background and β-radiation are filtered using β-filters. The beam of X-rays is passed through the soller and divergence slits and then allowed to fall on the sample.

The fine grains of sample are generally spread uniformly over a rectangular area of a glass slide. The sample is usually adhered to glass slide either using binders like collodion. The amount of the sample exposed generally depends on the scattering power of the elements and absorption coefficient of the sample. The crystalline sample usually shows good scattering and sharp diffraction lines.

In the diffractometer, the diffracted beams are passed though the soller slits and divergence and receiving slits. Then it is allowed to fall on a monochromator before detection. The gas filled tubes or scintillation counters are commonly used for the detection of the X-rays. The gas filled tubes can either be a proportional counter or Geiger-Muller counter. The gas filled tube is usually filled with a gas, which gets ionized with the impact of the radiation. The ions are collected by applying a potential difference between the two electrodes. The typical current obtained is proportional to the number of photons reaching the detector.

The diffracted rays are scanned by covering the angular range of 2θ. The angle (θ) where the incident beam satisfies the Bragg′s condition for a particular plane, a constructive interference among the diffracted X-rays occurs, giving a sharp rise in the intensity (peak). Thus, the counts or count rates of the X-ray photon are measured at different angles. The output is obtained as plot of the intensity of diffracted X-rays versus angle (2θ).

The peaks (also called as reflections) in the plot correspond to a set of parallel planes with inter-planar spacing d_{hkl}. The *d*-values are calculated from the position of the peaks. Thus, for a particular sample, a set of *d*-values giving constructive interference are observed. The peak positions are related to the unit cell parameters of the lattice. Also, a particular sample gives a characteristic set of *d*-values. Thus, they generally act as fingerprint for the crystalline materials and hence can be used for identification of the materials. The intensity distribution of the reflections is governed by the nature and kind of distribution of atoms in the unit cell. The absolute intensities of the reflections depend on the source intensity and counting time, in addition to the nature and kind of distribution of atoms in the unit cell.

For the present investigations we used a Philips 1710 diffractometer which is based on the Bragg-Brentano reflection geometry. The Cu K_α from a sealed tube is used as the incident beam. A Ni foil is used as a filter and the diffracted beam is monochromatized with a curved graphite single crystal. The diffractometer has a proportional counter (Argon filled) as the detector. For investigation of the glass samples, the X-ray tube rating was maintained at 40 kV and 30 mA throughout.

II. UV-Visible Spectrophotometry

UV-Visible Spectrophotometry works on the principle of Lambert – Beer law. It states that equal fractions of the incident light are absorbed by successive layers of equal thickness and equal concentration of absorbing medium. Spectroscopic analysis of a substance is carried out using radiation of a particular wavelength, which is absorbed, to the maximum extent. This wavelength is called λ_{max} of the substance. Other wavelengths are either not absorbed or absorbed minimally. Thus a substance may show strong absorption at several wavelengths depending on its structure. It is possible to identify a particular group in a molecule or a particular oxidation state of a metal ion by determining its λ_{max} value. In a typical absorption spectrophotometer, a continuum source, such as Xe, D_2 or W-Halogen lamp is used as the excitation source. A monochromator is used to produce the light of desired wavelength. Different elements in the sample absorb at different wavelengths (at their respective λ_{max}). A schematic diagram of a standard spectrophotometer is given in figure-2.2.

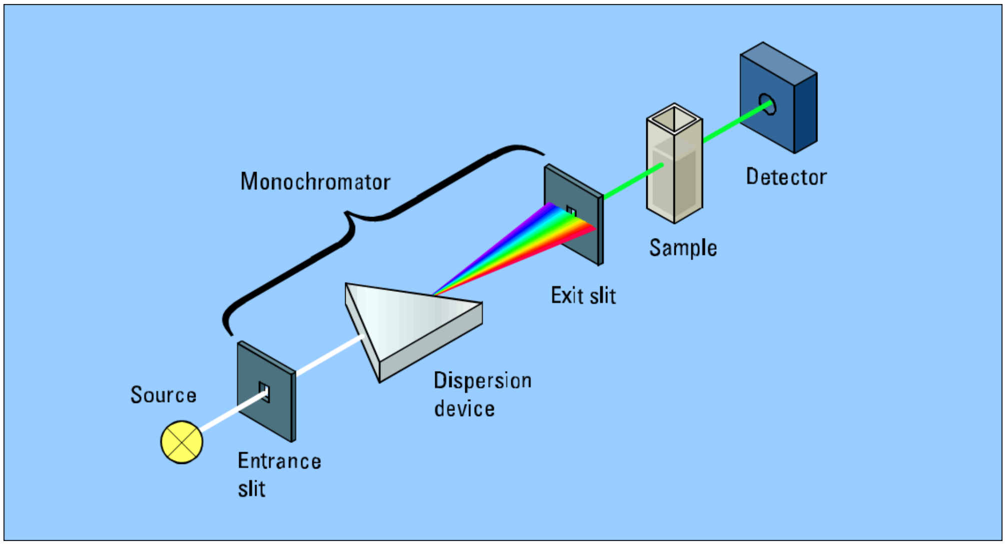

Figure. 2.2: Schematic diagram of a basic UV-Vis spectrophotometer

In the present case, UV-Visible absorption spectra of the glass samples were recorded using a Jasco V-350 UV/Vis spectrophotometer at ambient conditions. To cover the whole spectral range, studies were carried out in the wavelength range 200-1100 nm. The equipment records absorption or transmission spectra using socket type deuterium lamp and 50W long life halogen lamp as source of radiation for ultraviolet and visible region respectively. A photomultiplier tube is used for detection of transmitted photons. The instrument has a resolution is 1 nm with wavelength accuracy of ± 0.5 nm.

III. Photoacoustic spectroscopy (PS)

Photoacoustic spectroscopy is part of a class of “photothermal” techniques, in which an impinging light beam is absorbed and alters the thermal state of a sample. This "thermal state" can manifest itself as a change in temperature, density, or other measurable property of the sample. When an incoming light is modulated, the absorbing sample warms and cools in a cycle. If the cycle is so fast that the sample does not have time to expand and contract in response to the modulated light, a change in pressure develops. This pressure "wave" can lead to the production of a sound wave. This signal is known as photoacoustic signal.

In 1880, Alexander Graham Bell found that when a thin disk was exposed to mechanically chopped sunlight, sound was emitted [7]. In addition, he noted a similar effect when infrared or ultraviolet light was used. This effect was essentially forgotten until researchers led by Allen Rosencwaig rediscovered the behavior and provided a theoretical basis for the same [8]. The commonly accepted mechanism for the photoacoustic effect is called RG theory, after its developers Rosencwaig and Gersho [9].

The main source of the acoustic wave is the repetitive heat flow from the absorbing condensed-phase sample to the surrounding gas, followed by propagation of the acoustic wave through the gas column to microphone-based detector. The photoacoustic signal can also be detected piezoelectrically. Instead of being dissipated as heat, the absorbed radiant energy can be transferred through the solid-state vibrational modes, or phonon modes, of the sample. The motions of these phonon modes are nondissipative (unlike heating), limited only by the size of the sample. A piezoelectric detector physically connected to the sample can detect absorbed energy in this manner. Although piezoelectric detection is about 100 times less sensitive than microphone detectors, it can be preferable for large samples or for samples that do not efficiently convert absorbed light to heat.

The advantage of photoacoustic spectroscopy is that it can be performed on all phases of matter using lasers so that very small concentrations also can also be determined. This technique being non-destructive in nature, the sample does not have to be dissolved in some solvent or embedded in a solid-state matrix. Sample can be used "as it is."

A typical experimental setting for a photoacoustic spectrometer is shown in figure 2.3 A. A photograph of the instrument is shown in figure 2.3 B.

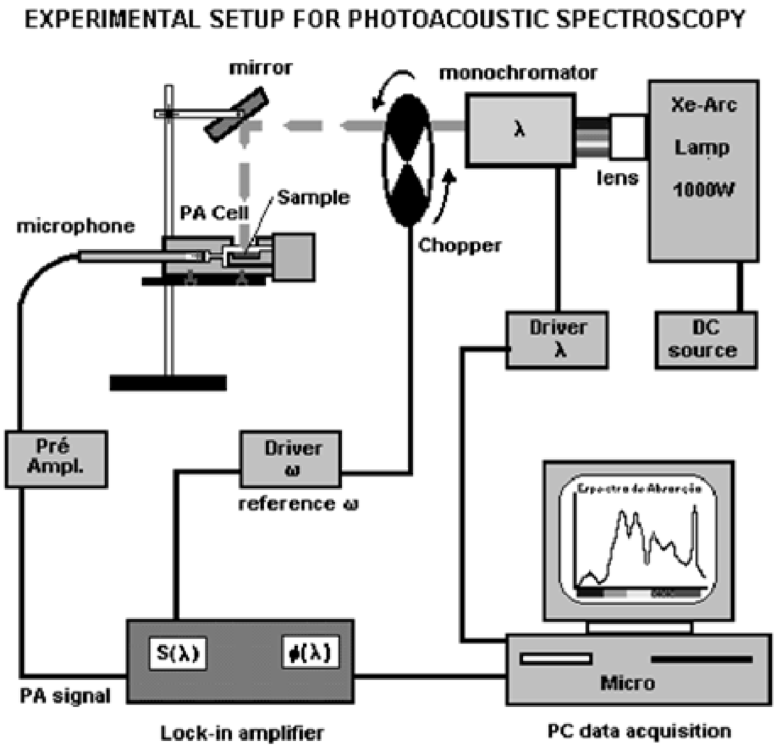

Figure. 2.3 A: Schematic of a PS spectrometer with microphone as the detector

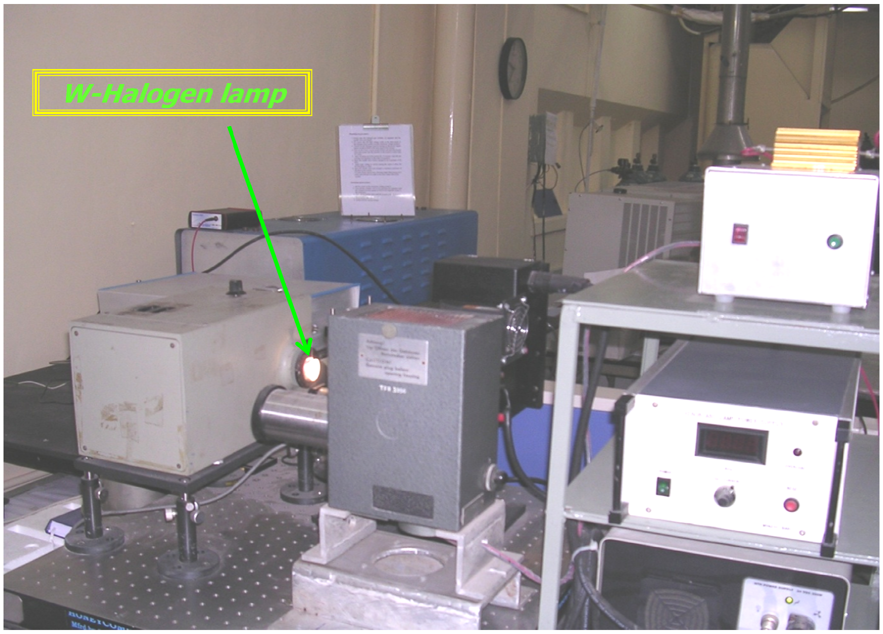

Wavelength range – 350-900nm

Figure. 2.3 B: Photograph of the home built PS spectrometer

For the present PAS investigations, a home built PAS spectrometer was used [10]. The PAS unit consists of 250 W tungsten-halogen lamp, 0.25 M monochromator (model 82-410, Jarrell-Ash Ebert), PAS cell and lock-in amplifier (model– IE 1033, Unilock) designed and fabricated in-house. The light beam from the tungsten-halogen source is chopped at 33 Hz using a mechanical chopper. This chopper also provides the reference voltage needed for lock-in-amplifier. The design of non resonant photoacoustic cell is based on the Rosencwaig criteria [11] which accommodates a prepolarized condenser microphone (Type 4155, BRÜEL & KJÆR, sensitivity = 50 mV/Pascal). The photoacoustic volume was isolated from the surrounding noise by the use of a heavy metallic block during the fabrication of the photoacoustic cell. The monochromator operation was controlled by a stepper motor and the steps were calibrated to wavelength. Automatic acquisition of the PAS signal from lock-in-amplifier as a function of wavelength through PC was achieved using a PCI-1050, 12 bit multifunction Dynalog DAS card. The sample spectrum was normalized by comparing it to that of a pre-stored Carbon-black spectrum.

IV. Photoluminescence (PL) Spectroscopy

Photoluminescence (abbreviated as PL) is a process in which a substance absorbs photons (electromagnetic radiation) and then emits its characteristic luminescence. Quantum mechanically, this can be described as an excitation to a higher energy state and then return to a lower energy state accompanied by the emission of a photon. This phenomenon is a subset of a more broad process known as luminescence or light emission. This process is different from the other processes of luminescence such as chemiluminescence (emission of light due to chemical reaction), thermoluminescence (emission due to external heating), mechanoluminescence (emission due to mechanical energy), triboluminescence (emission due to external pressure) or bioluminescence (emission from biological reactions). The period between absorption and emission is extremely short, typically of the order of 10 nanoseconds. Under special circumstances, however, this period can be extended into minutes or hours. The simplest photoluminescence processes are resonant radiations, in which a photon of a particular wavelength is absorbed and an equivalent photon is immediately emitted. This process involves no significant internal energy transitions of the chemical substrate between absorption and emission and is extremely fast, of the order of 10 nanoseconds. More interesting processes occur when the chemical substrate undergoes internal energy transitions before emitting the higher wavelength radiations than excitation wavelength.

The most familiar effect is fluorescence, which is a fast process, but in which some of the original energy is dissipated so that the emitted light photons are of lower energy than those absorbed. The generated photon in this case is said to be red shifted, referring to the loss of energy as Jablonski diagram shows (figure 2.4).

An even more specialized form of photoluminescence is phosphorescence, in which the energy from absorbed photons undergoes intersystem crossing into a state of higher spin multiplicity, usually a triplet state.

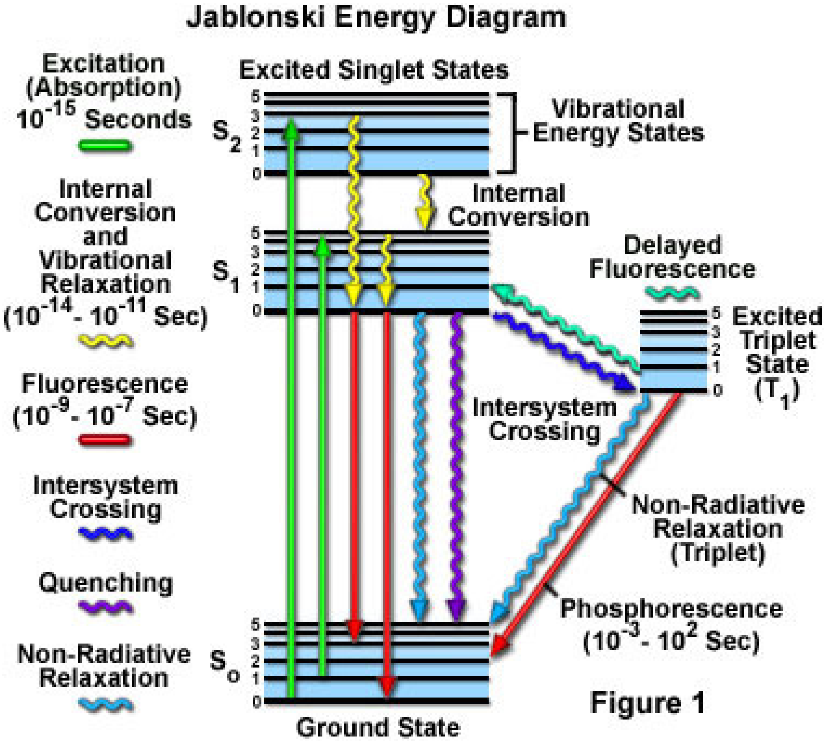

Figure. 2.4: A simplified Jablonski Diagram

Once the energy is trapped in the triplet state, transition back to the lower singlet energy states is quantum mechanically forbidden, meaning that it happens much more slowly than other transitions. The result is a slow process of radiative transition back to the singlet state, sometimes lasting even minutes or hours. In practice, the fluorescence and phosphorescence spectra are collectively called as emission spectra.

The intensity and spectral content of this photoluminescence is a direct measure of various important material properties like oxidation states of metal ions, co-ordination numbers, covalency etc.

In photoluminescence another important parameter that one comes across is the fluorescence life time or decay time of the particular metal ion. It is defined as the time taken for the excited state population to become 1/e of the original value. The lifetime of a luminescent ion gives vital information about its' bonding, coordination number and covalency. By virtue of this triple resolution namely, excitation, emission and lifetime resolution, PL technique offers a very powerful yet non-invasive technique for material characterization.

This technique being a contactless, nondestructive method for probing the electronic structure of materials, has extensive use in speciation studies of various metal ions in crystalline as well as amorphous matrices.

For the present set of investigations, an Edinburgh 920 series spectrometer was used which works on the principle of Time Correlated Single Photon Counting (TCSPC). The spectrometer is equipped with a Xe flash lamp and a couple of M 300 monochromator providing resolution of ~1 nm.

Time Correlated Single Photon Counting (TCSPC)

TCSPC technique is a digital counting technique where the photons, that are time correlated in relation to an excitation light pulse, are counted. The sample is repetitively excited using a pulsed light source and the measurement builds a probability histogram relating the time between an excitation pulse (Start) and the observation of the first fluorescence photon (Stop). The fact that the time at which a fluorescence photon is incident on the detector can be defined precisely is critical to the working of TCSPC. The output pulses from the photomultiplier corresponding to individual photon detection, have a significant spread in pulse height. This implies that timing based on amplitude threshold would be subject to considerable jitter. A constant fraction discriminator (CFD) is used to extract precise timing information from the detector pulse output using a method that is largely independent on the amplitude of the pulse.

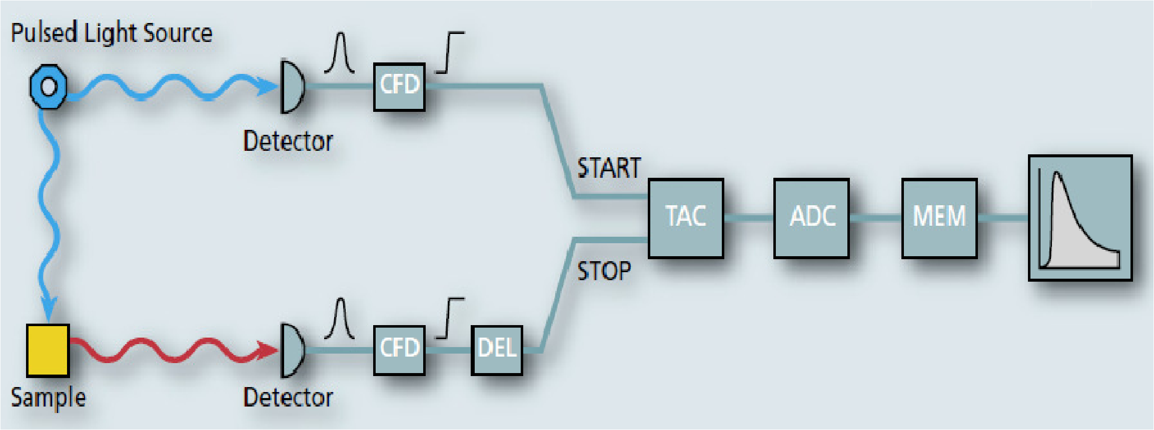

Figure. 2.5 A: Block diagram of TCSPC set up for PL experiments

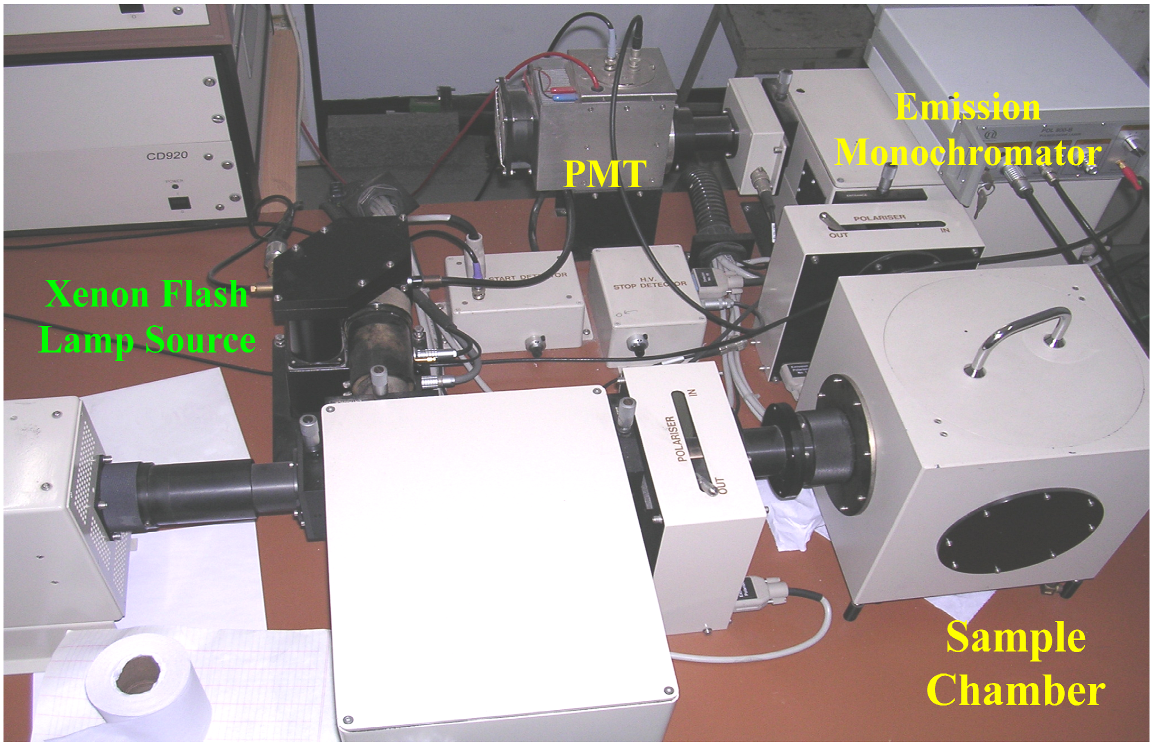

Wavelength range – 180-900nm

Figure. 2.5 B: Photograph of the CD-920 time resolved PL spectrometer

The ‘start’ signal triggers a linear voltage ramp of the ‘time to amplitude converter’ (TAC). This ramp is stopped when the first photon is detected. The TAC produces a voltage output which is proportional to the time between the start and the stop signal. The voltage is read by an analog to digital converter (ADC) and the value is stored in the memory (MEM). Summing over many such start-stop cycles, the evolution of the probability histogram can be displayed in real time representing the growth and decay of the fluorescence [12]. A schematic representation for the TCSPC set up is shown in figure 2.5 A. a photograph of the CD-920 PL life time spectrophotometer is shown in figure 2.5 B.

V. Electron Paramagnetic Resonance (EPR) Technique

A molecule or an ion having unpaired electron(s) absorbs electromagnetic radiation of microwave frequency under the influence of a magnetic field. This phenomenon is known as electron spin resonance (ESR) and it is exhibited by a paramagnetic species. Therefore it is also referred as electron paramagnetic resonance (EPR). Large number of materials in nature contains unpaired electrons. EPR is a unique technique to identify the paramagnetic species such as free radicals, transition metal complexes and defects in solid materials both crystalline and amorphous. Free radicals are often short lived, but still they play crucial role in many processes such as photosynthesis, redox reactions, catalysis and polymerization reactions. Therefore this technique is extensively used in Chemistry, Physics, Material Science, Biology and Life Science [3]. EPR spectrum of a sample is very sensitive to the local environment around a paramagnetic ion. Therefore, this technique is used to probe the local coordination around the paramagnetic ion.

Sometimes the EPR spectra exhibit dramatic changes in the line shape giving insight into dynamic processes such as molecular motion or fluidity.

A. Basic Theory of EPR

Interaction between electron spin and magnetic field: the Zeeman Effect

An electron has a spin quantum number s = ½. The magnetic spin quantum number corresponding to these orientations are Ms = +½ and Ms = -½. In the absence of any external magnetic field, the two Ms states will have same energy (degenerate). On the application of a magnetic field (represented as H or B), the degeneracy of these two states is lifted. This effect is called the Zeeman Effect. It is said that out of the two states Ms = ± 1/2, Ms = -1/2 state get aligned parallel with the direction of the applied field and its energy is lowered (E = -1/2 gβB), where as Ms = +1/2 state gets oriented anti parallel with respect to the applied field and its energy is raised (E = +1/2 gβB). Thus the two otherwise degenerate Ms states, in the absence of magnetic field get separated by gβB (or gβH) on the application of a magnetic field. Now, if an energy corresponding to a microwave frequency υ is fed to the electron and the applied magnetic field is such that hν = gβB the energy will be absorbed by the Ms = -1/2 state and a transition between the two Ms states will take place (Figure. 2.6). The energy differences we study in EPR spectroscopy are predominately due to the interaction of unpaired electrons in the sample with a magnetic field produced by a magnet in the laboratory.

In the basic equation of EPR, hν = gβB; 'g' is a proportionality constant approximately equal to 2 for most samples, but varies depending on the electronic configuration of the radical or ion. From this it is clear that, the two spin states have the same energy in the absence of a magnetic field and the differences in the energies of the spin states diverge linearly as the magnetic field increases. These two statements have important consequences for spectroscopy:

- Without a magnetic field, there is no energy difference to measure.
- The measured energy difference depends linearly on the magnetic field.

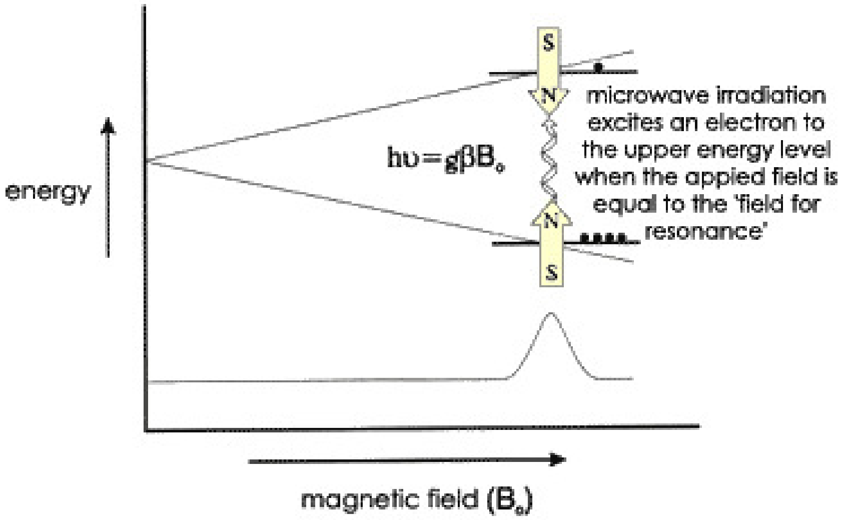

Figure. 2.6: Energy level diagram and resonance conditions for s = ½ system. Resonance conditions hν = gβB where g is spectroscopic splitting factor, β is Bohr magneton, which is the natural unit of electronic magnetic moment and B is the applied magnetic field

Because we can change the energy differences between the two spin states by varying the magnetic field strength, we have an alternative means to obtain spectra. We could apply a constant magnetic field and scan the frequency of the electromagnetic radiation as in conventional spectroscopy. Alternatively, we could keep the electromagnetic radiation frequency constant and scan the magnetic field. A peak in the absorption will occur when the magnetic field tunes the two spin states so that their energy difference matches the energy of the radiation resulting in a resonance. Owing to the limitations of microwave electronics, the magnetic field is scanned keeping the frequency fixed in all standard EPR spectrometers.

The field for resonance is not a unique fingerprint for identification of a compound because spectra can be acquired at several different frequencies. The g-factor, being independent of the microwave frequency, is much better for that purpose. High values of 'g' occur at low magnetic fields and vice versa. A list of fields for resonance for a $g = 2$ signal at microwave frequencies commonly available in EPR spectrometers is presented in table 2.1. Depending on the frequency at which the resonance occurs, the spectrometers are named as S, X, K, Q etc.

B. 'g' value and factors affecting it

The spectroscopic splitting factor 'g' is the measure of the total magnetic moment associated with the paramagnetic species and it is represented by the following equation.

$g = 1 + [J(J+1) + S(S+1) - L(L+1)]/[2J(J+1)]$.

For a free electron, $S = 1/2$, $L = 0$, $J = S = ½$. This gives $g = 2.0$. The g factor is a dimensionless constant.

For most of the free radicals g value is very close to 2.0000. This is because in case of radicals the unpaired electron is not confined to a localized orbital but can move freely over the orbital resulting in the quenching of the orbital contribution ($L=0$).

In case of transition metal complexes, on the other hand, the unpaired electron is confined in a particular orbital. Because of the loss of orbital degeneracy and the spin orbit coupling the 'g' value of the complex is different from 2.0000.

Microwave Band	Frequency (GHz)	H_{res}(Gauss)
L	1.1	392
S	3.0	1070
X	9.75	3480
Q	34.0	12000
W	94.0	34000

Table-2.1. Field for resonance, B_{res} or H_{res}, for a g = 2 signal at selected microwave frequencies.

The 'g' value of the transition metal complexes depends on the relative magnitude of the spin orbit coupling and the crystal field splitting. The spin orbit contribution makes 'g' as a characteristic property of a transition metal ion and its oxidation state. From the 'g' value of a transition metal complex, one can obtain important information about the structure of the complex. For such complex in solution or gas phase, the g value is averaged over all the orientations because of the free motion of the molecules. In solids, the movement of the molecule is restricted. In a cubic crystal field, the metal ligand bond lengths are same along three crystallographic axes and hence g value remains the same (isotropic), that is $g_x = g_y = g_z$. If the crystal field is tetragonal, the metal - ligand distance along the x and y axis are the same but different from the metal ligand distance along the z direction. The g value for such complex is anisotropic and they are expressed as $g_z = g_{||}$ and $g_x= g_y = g_\perp$. Whereas if the symmetry of the complex is orthorhombic, all the three g values will be different that is $g_x \neq g_y \neq g_z$.

C. Interaction between electron spin and nuclear spin: The hyperfine interaction

The nuclei of the atoms in a molecule or complex often have a magnetic moment, which produces a local magnetic field at the electron. Splitting of an EPR line due to interaction of the unpaired electron with its own nucleus is known as hyperfine interaction. Figure 2.7 depicts the origin of the hyperfine interaction. The spinning of the nucleus produces a magnetic field at the electron, B_1. This magnetic field opposes or adds to the magnetic field from the laboratory magnet, depending on the alignment of the moment of the nucleus. When B_1 adds to the magnetic field, we need less magnetic field from our laboratory magnet and therefore the field for resonance is lowered by B_1. The opposite is true when B_1 opposes the laboratory field. For a spin ½ nucleus, such as a proton nucleus, we observe that the single EPR absorption signal splits into two signals which are away from the original signal by B_1 (Figure 2.8.).

If there is a second nucleus, each of the signals is further split into a pair, resulting in four signals. For N number of spin 1/2 nuclei, we will generally observe a total of 2^N EPR signals. As the number of nuclei gets larger, the number of signals increases exponentially. Sometimes there are so many signals that they overlap and we only observe the one broad signal. The selection rules for EPR are Δ Ms = ± 1 and Δ MI = 0.

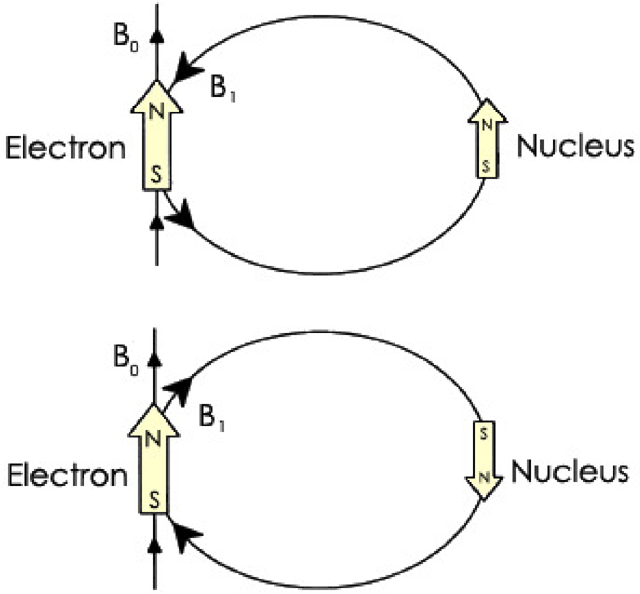

Figure. 2.7: Hyperfine interaction

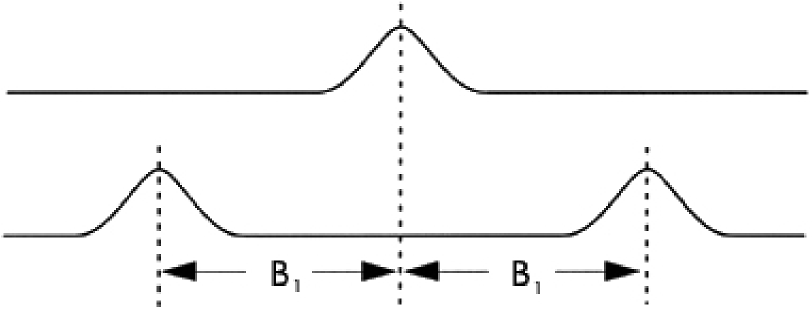

Figure. 2.8: Splitting in an EPR signal due to the local magnetic field of a nearby nucleus

The number of hyperfine transitions are given by the total number of orientations of the nuclear spin I, i.e., by (2I+1). These lines are of equal intensity and separated by spacing of A, which is usually known as the hyperfine coupling constant. The hyperfine interaction is described by including the term of the type $H_{h.f.} = M_I.A.M_S$. to the total

Hamiltonian. The magnitudes of the hyperfine coupling constant depend on the nature of the covalent bonding.

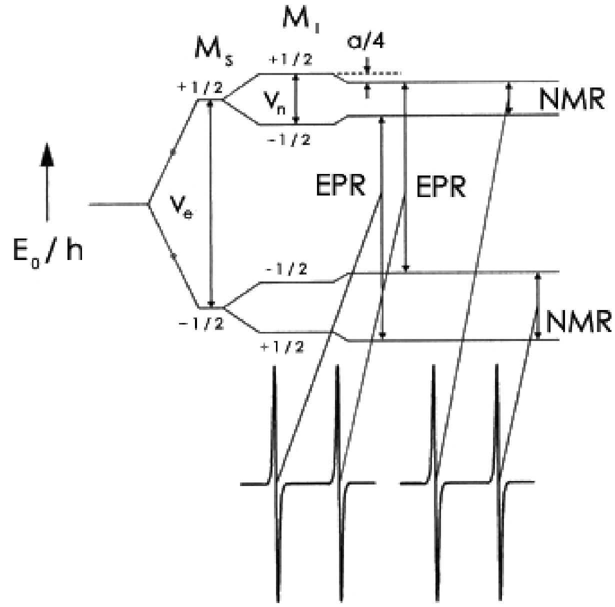

Figure. 2.9: Energy level diagram for the interaction of an electron(s=1/2) with proton (I=1/2)

With increasing covalency the hyperfine coupling constant would decrease due to larger extent of delocalization of unpaired electron to the neighboring atoms. For example the ^{1}H atom has single unpaired electron (s = ½) and its nuclear spin I = ½. So the EPR spectrum of a hydrogen atom in a solid matrix will consist of two peaks of equal intensity centered at g = 2.0023. The two energy levels of the free electron in a magnetic field consisting of Ms = -1/2 aligned with the field and Ms = + ½ aligned opposite to the field. The spectrum of the free electron in hydrogen atom would consist of a single peak corresponding to a transition between these levels. For each of the electron spin quantum number (m_s), the magnetisation quantum number M_I, can have values of ± 1/2., giving rise to four different energy levels. The energies of these levels are given by expression $E = g\beta BMs + A.MsMI$ where A is hyperfine coupling constant [4].

D. Super hyperfine interaction

If the unpaired electron on the paramagnetic ion interacts with the surrounding nuclei (neighboring nuclei) having magnetic moment ($I \neq 0$), it causes further splitting of the lines which is referred as super hyperfine structure. If the unpaired electron interacts with ‘n’ number of equivalent nuclei of spin I, the super hyperfine structure would consist of ($2nI+1$) components having binomial distribution of intensity. The super hyperfine structure gives information about the number of surrounding nuclei and their equivalence. The super hyperfine coupling constant is a measure of the extent of covalence *viz* the extent of delocalization of the unpaired electron on to the neighboring nuclei.

E. Fine structures in the EPR spectrum

In a paramagnetic system where the ground state is an orbital singlet ($L = 0$) with spin multiplicity greater than two [$(2S+1)> 2$], very often there is initial splitting of the ground state multiplet even in the absence of a magnetic field. The most important cause of this splitting is the Stark effect due to asymmetrical crystalline fields together with the spin orbit interaction which mixes the ground state with the excited states. Whenever there is zero field splitting of the ground state multiplet, the system of Zeeman components arising from the ground state multiplet ceases to be equally spaced and all the resonant transitions ($\Delta Ms = \pm 1$) do not occur at the same frequency and there will be 2S well separated transitions. This is called as fine structure of the paramagnetic resonance spectrum.

For example the ground state ^4F of Cr^{3+} (S= 3/2) splits in a cubic crystalline field giving the lowest orbital singlet ^4A_2g and two higher lying orbital triplets. Considering the S-state ion Mn^{2+} the six fold spin degeneracy of the ^6S ground state is partly lifted giving three- Kramer's doublets in the presence of an axial crystalline field. This splitting is responsible for the observation of five fine transitions in the EPR spectrum of Mn^{2+} ion. The fine structure in the EPR spectrum is represented by the term $[D\{S_z^2-1/3S(S+1)\} + E(S_x^2-S_y^2)]$ in the Hamiltonian [5].

The value of D is the measure of axial distortion whereas E is a measure of non axial (orthorhombic) distortion. This term would vanish for S = ½ and cubic fields. The different possibilities that can occur are D= 0, E =0 for cubic symmetry, $D \neq 0$, E = 0 for axial symmetry and $D \neq 0$, $E \neq 0$ for orthorhombic symmetry.

F. Introduction to the EPR spectrometers

The simplest possible spectrometer has three essential components: a source of electromagnetic radiation, a sample, and a detector. To acquire a spectrum, we change the frequency of the electromagnetic radiation and measure the amount of radiation which passes through the sample with a detector to observe the spectroscopic absorptions. Despite the apparent complexities of any spectrometer we may encounter, it can always be simplified to the block diagram shown in Figure 2.10.

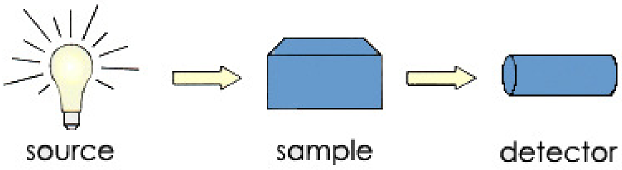

Figure. 2.10: The simplest spectrometer

Figure 2.11 A shows the general layout of an EPR spectrometer. The electromagnetic radiation (microwave) source is usually an electron tube known as Klystron or a diode known as gunn-diode. The detector is usually a diode crystal. The microwave source and the detector are in a box called the microwave bridge. The sample is in a microwave cavity, which is a metal box that helps to amplify weak signals from the sample. The cavity is placed between the two poles of a strong electromagnet. A console holds the controlling, signal processing and general electronics of the spectrometer. A computer is used for analyzing data as well as coordinating all the units for acquiring a spectrum. A photograph of the ESR spectrometer used for the present investigations is presented in figure 2.11 B.

The microwave bridge

The microwave bridge houses the microwave source, the detector and associated electronics. The basic parts of a microwave bridge are shown in Figure 2.12. If one follows the path of the microwaves from the source to the detector, then the following sequence of events will take place.

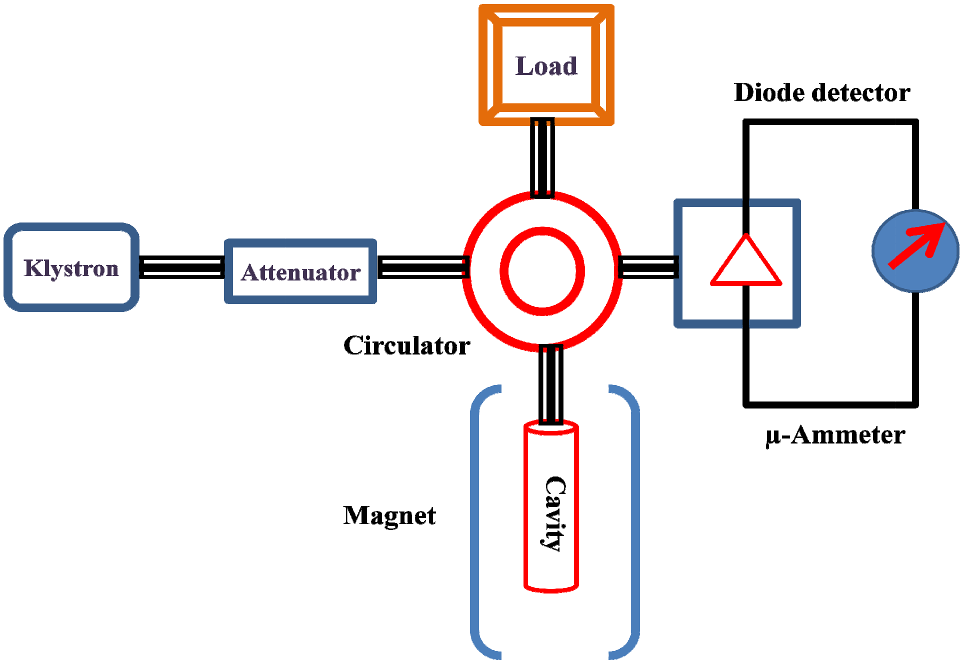

Figure. 2.11 A: The general outlay of an EPR spectrometer

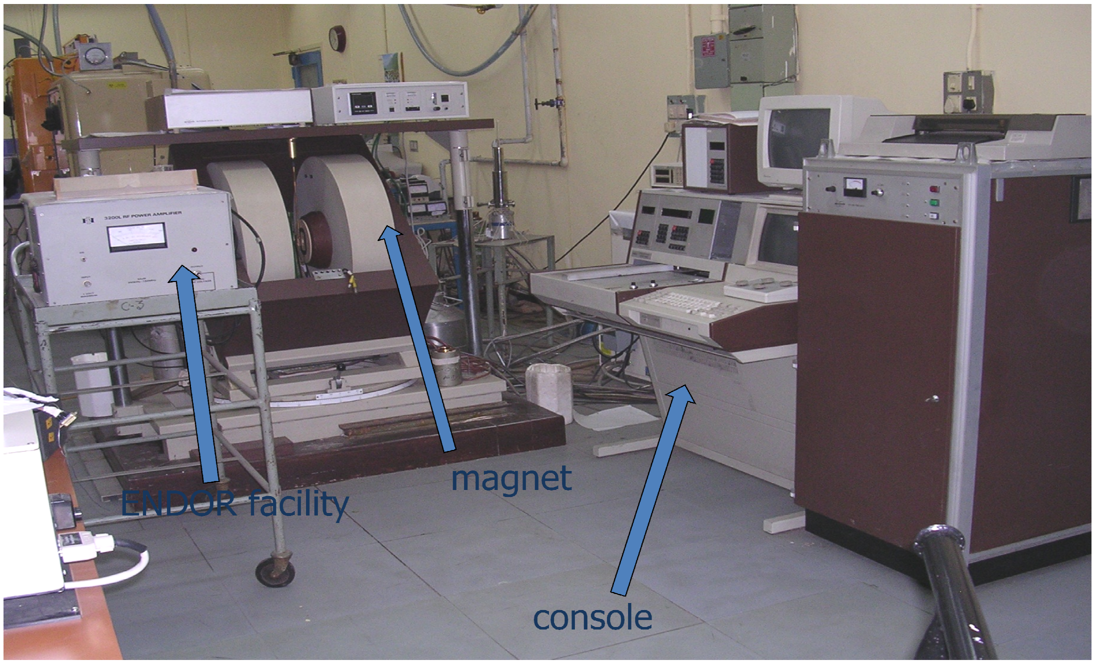

Bruker ESP- 300 spectrometer operating at X-band (ν = 9.5 GHz)
with situ-variable temperature facility from 20-1200 K

Figure. 2.11 B: Photograph of the ESR/EPR spectrometer used for the investigation

Microwaves are generated at the source point A in the diagram. To control the intensity of the microwaves we have an attenuator B, a device which blocks the flow of microwave radiation. With the attenuator, we can precisely and accurately control the microwave power seen by the sample. Most EPR spectrometers are reflection spectrometers. They measure the changes (due to spectroscopic transitions) in the amount of radiation reflected back from the microwave cavity containing the sample (point D in the figure). Hence the objective is to adjust the detector to see only the microwave radiation coming back from the cavity, which is possible because of the microwave device at point C (circulator). Microwaves coming in port 1 of the circulator only go to the cavity through port 2 and not directly to the detector through port 3.

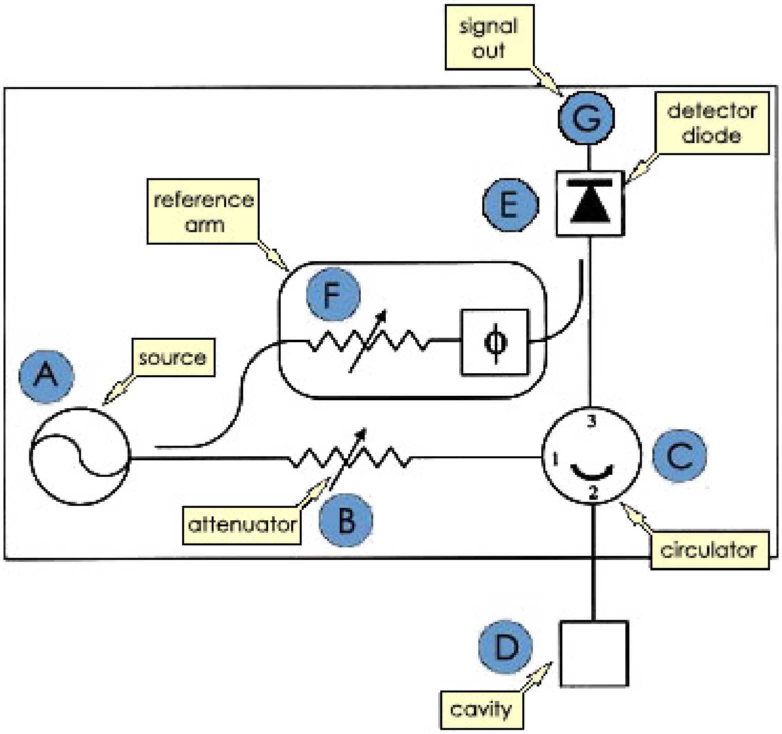

Figure. 2.12**:** Block diagram of a microwave bridge

Reflected microwaves are directed only to the detector and not back to the microwave source. A Schottky barrier diode to detect the reflected microwaves (point E in the figure). It converts the microwave power to an electrical current.

To ensure that the detector operates at an optimum level, there is a reference arm (point F in the figure) which supplies the detector with some extra microwave power or bias. Some of the source power is tapped off into the reference arm, where a second attenuator controls the power level (and consequently the diode current) for optimal performance. There is also a phase shifter to ensure that the reference arm microwaves are in phase with the reflected signal microwaves when the two signals combine at the detector diode. The detector diodes are very sensitive to damage from excessive microwave power and will slowly lose their sensitivity. To prevent this from happening, there is protection circuitry in the bridge which monitors the current from the diode [6].

VI. Positron annihilation Spectroscopy (PAS)

Before understanding positron annihilation spectroscopy (PAS), let us understand what positrons are? Positrons are the antimatter or anti-particles to the electron, that is they have the same mass but opposite charge. A thermalised positron annihilates with an electron converting their mass into energy in the form of γ-rays. The total energy of these γ-rays can be calculated from Einstein's famous equation, $E=mc^2$. Therefore, positron/electron annihilation produces two 511 keV energy γ-rays, always emitted back-to-back at opposite directions (due to momentum considerations). Positrons may form an exotic atom with an electron called Positronium (Ps). Ps is a hydrogen-like atom, except with the proton replaced by a positron. As Ps is formed of antimatter particles, it has a short lifetime before annihilation (142 ns in vacuum). Interactions of Ps atoms with other atoms/molecules may reduce the lifetime through a process called quenching, whereby the positron in the Ps atom annihilates with an electron from the other atom/molecule. Amongst other processes, positrons may be obtained through radioactive decay, wherein a proton is converted to a neutron and the positive charge is emitted in the form of a positron. ^{22}Na is a positron emitter and has a half life of 2.6 years, which makes it useful for lab based experiments with positrons.

PAS is a non destructive technique for characterizing the free volumes/defects/ porosity of materials [13]. The technique operates on the principle that a positron or positronium will annihilate through interaction with electrons. This annihilation releases gamma rays that can be detected; the time between emission of positrons from a radioactive source and detection of gamma rays due to annihilation corresponds to the lifetime of positron or positronium. When positrons are injected into a solid body, they will interact with the electrons in that species. For solids containing free electrons (such as metals or semiconductors), the implanted positrons will annihilate very rapidly unless voids such as vacancy defects are present [14]. If voids are available, positrons will reside in them and annihilate less rapidly than in the bulk of the material, on time scales up to ~1 ns. For insulators such as polymers or zeolites, implanted positrons interact with electrons in the material to form positronium. Triplet positronium has a characteristic lifetime of 142 ns in vacuum; in solids, this lifetime is reduced depending on the pore structure of the analyte (similar to positrons, but on a larger size and time scale).

Positron annihilation lifetime spectroscopy (PALS) is one of the techniques in PAS, which provides the information about the electron density in the medium and thereby the defects and microstructure of the sample.

PALS has been widely used as an important non destructive tool to study the defects in metals and semiconductors as well to study the free volume related microstructure in different crystalline and amorphous solid substances. Because of its light mass and positive charge, positrons are sensitively trapped at vacancy-type defects and give us very useful information about their size, concentration and electronic structures. Several groups have studied the positron annihilation behavior in silica and other glassy materials [15-18]. A borosilicate based glassy system can be visualized as a continuous random network of tetrahedra of the glass forming elements e.g. Si and B, joined at the corners such that each silicon atom is bonded to four oxygen atoms and each oxygen atom bridges between two silicon or boron atoms (known as the bridging oxygen). The bond angle of a regular Si-O-Si bond in amorphous borosilicate glass varies largely from 109 ° to 180 ° [19, 20] and hence the resulting structure has large open spaces or voids. When positron is introduced into such an amorphous material with large void spaces, a fraction of thermalized positron may form positronium (a bound-state of an electron and positron) and localize in the void space. Positronium (Ps) is formed either as spin-singlet *para* positronium (p-Ps) or spin triplet *ortho* positronium (o-Ps) with a ratio 1:3. In vacuum, p-Ps decays into two photons with intrinsic lifetime 0.125 ns and o-Ps decays into three photons with a large intrinsic lifetime 142 ns. However, in the presence of matter, o-Ps can seek out electron with opposite spin from the surface of the void and annihilate through two-photon mode known as *pick-off* annihilation with lifetime range

~1-10 ns. Thus, the o-Ps *pick-off* annihilation rate (or lifetime) and their intensity can give valuable information about the void size and their number density.

PALS spectrometer

When a positron is emitted from a ^{22}Na atom, the residual nucleus (^{22}Ne) is left behind in an energetic state. This energy is then emitted as a γ-ray with energy 1.275 MeV. Detection of this γ-ray tells us when a positron is born, i.e. the start of its lifetime. The positron is implanted into a material, whereby it quickly thermalises (~10ps) and either annihilates or forms a Ps atom. The Ps atoms tend to reach to pores within the material where they are confined and bounce off the walls. Each time they impact the walls there is a probability of the atom annihilating releasing 511 keV γ-rays. Therefore, the time after being emitted from the ^{22}Na source and when the positron annihilates tells us information on the size and number of pores (fractional free volume) within the material. By detecting the time between the 1.275 MeV and 511 keV γ-rays, a lifetime spectrum may be measured. In order to determine the pore size of a sample, the lifetime for Ps atoms annihilating in the pores is extracted from the lifetime spectrum. The longer is the lifetime, the larger is the pore size. The intensity of the Ps annihilation lifetime also gives information on the fractional free volume.

A typical spectrometer consists of two scintillation detectors (D1 and D2) optically coupled to photo multiplier tube detectors (PMTs). The latter converts the light photon emitted by the scintillator to photoelectrons which are multiplied and finally collected at anode to give an electrical signal.

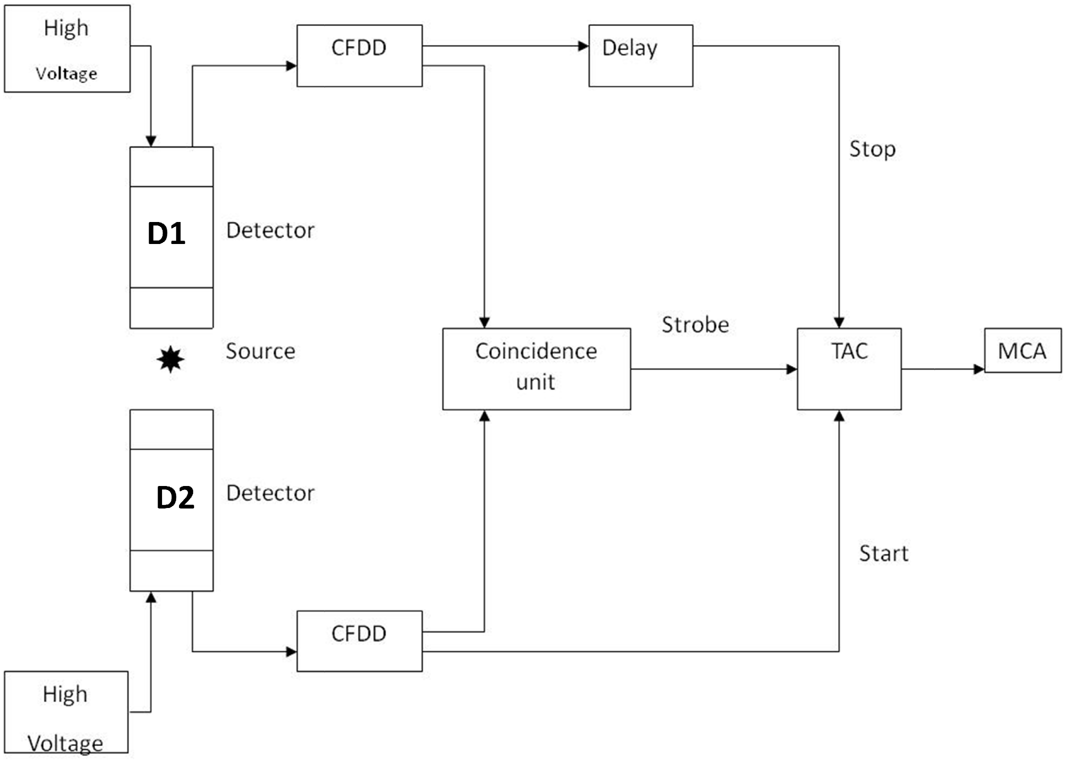

Figure. 2.13: Schematic diagram of a PAS instrumental set up

D1 detects the 1.275 MeV γ-rays representing the positron being emitted from ^{22}Na, whilst D2 detects the 511keV from the annihilation of the positron within the sample. The pulses are processed in a fast-fast coincidence set up similar to TCSPC to obtain a time spectrum for positron annihilation within the sample material. A schematic of the instrumental set up is presented in figure 2.13.

VII. FTIR Technique

FTIR technique was used for carrying out structural characterization of glass samples. FTIR technique is based on Michelson interferometer, which is an optical device consisting of a fixed mirror, movable mirror and a beam splitter. The interferometer shifts the phase of one of the beams with respect to another by moving one of the mirrors and keeping the other mirror at fixed position. When the two beams overlap, depending on whether they are in phase or out of phase, constructive and destructive interference takes place. If the light source is monochromatic, the intensity of the interference pattern will rise and fall periodically and the detector will measure a sinusoidal signal as a function of the optical path difference. When the light source contains many frequencies, like the radiation emitted from a Globar IR source, the intensity measured, I (x), as function of optical path difference, (x) is known as the interferogram. Fourier transformation of the interferogram results in the frequency spectrum, I (v). The optical path difference (x) , can be accurately obtained from the interference patterns generated from the interferometer using a laser source, whose frequency is accurately known.

In the present study all IR experiments were carried out using a Bomem MB102 FTIR machine with resolution of 4 cm^{-1} having a range of 200-4000 cm^{-1}. IR radiation was generated from a Globar source (bonded silicon carbide rod). The instrument uses CsI single crystal, as the beam splitter and deuterated triglycine sulphate (DTGS) as the detector. A He-Ne laser having a wavelength of 632.9 nm (with a max. power of 25μW) has been used for the calibration purpose. Prior to the IR measurements, the samples were ground thoroughly by mixing with dry KBr powder, made in the form of a thin pellet and introduced into the sample chamber for recording the IR spectra.

Attenuated Total Reflection (ATR) FTIR

An attenuated total reflection accessory operates by measuring the changes that occur in a totally internally reflected IR beam when the beam comes in contact with a sample as shown in the figure 2.14. An IR beam is directed onto an optically dense crystal with a high refractive index at a certain angle. This internal reflectance creates an evanescent wave that extends beyond the surface of the crystal into the sample held in contact with the crystal. The evanescent wave can be thought of as a bubble of IR that sits on the surface of the crystal. This wave protrudes only a few microns (0.5-5 μ) beyond the crystal surface and into the sample. Consequently it can probe the surface and few microns into the sample. However, there must be good contact between the sample and the crystal surface. In regions of the IR spectrum where the sample absorbs energy, the evanescent wave will be attenuated or altered. The attenuated energy from each evanescent wave is then passed back to the IR beam which then exits from the opposite end of the crystal and passed to the IR detector which in turn generates the IR spectrum. For this technique to be successful the following two requirements should be satisfied.

(a) The sample must be in direct contact with the ATR crystal

(b) The refractive index of the ATR crystal must be significantly greater than that of the sample otherwise internal reflection will not occur. The light will be simply transmitted rather than internally reflected. A typical ATR crystal has a refractive index value in between 2.38 and 4.01 at 2000 cm^{-1}.

Typical materials for ATR crystals include germanium, KRS-5 and zinc selenide, while ‘silicon’ is ideal for use in the Far-IR region of the electromagnetic spectrum. The excellent mechanical properties of ‘diamond’ make it an ideal material for ATR, particularly when studying very hard solids, but its much higher cost limits its use. The shape of the crystal depends on the type of spectrometer and nature of the sample.

With dispersive spectrometers, the crystal is a rectangular slab with chamfered edges,. Other geometries use prisms, half-spheres, or thin sheets.

For the present set of investigations, a Bruker - Vertex 80 V spectrometer was used.

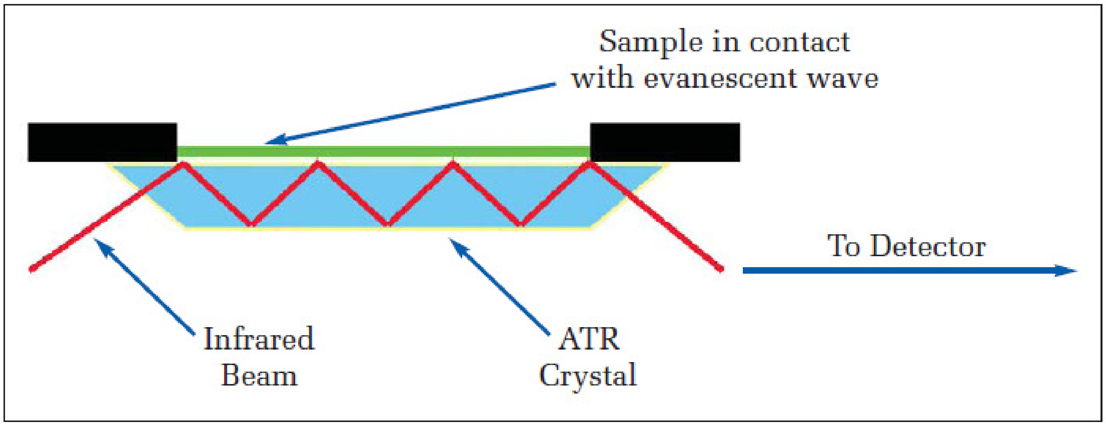

Figure. 2.14: Schematic diagram for an ATR-FTIR set up

VIII. Raman Spectroscopy

Raman Spectroscopy is a technique used to study vibrational, rotational, and other low-frequency modes in a system and relies on inelastic scattering [4]. The Raman Effect occurs when light impinges upon a molecule and interacts with the electron cloud and the bonds of that molecule. For the spontaneous Raman Effect, which is a form of light scattering, a photon excites the molecule from the ground state to a virtual energy state. When the molecule relaxes it emits a photon and it returns to a different rotational or vibrational state. The difference in energy between the original state and this new state leads to a shift in the emitted photon's frequency away from the excitation wavelength. If the final vibrational state of the molecule is more energetic than the initial state, then the emitted photon will be shifted to a lower frequency in order for the total energy of the system to remain balanced. This shift in frequency is designated as a Stokes shift. If the final vibrational state is less energetic than the initial state, then the emitted photon will be shifted to a higher frequency, and this is designated as an Anti-Stokes shift. Raman scattering is an example of inelastic scattering because of the energy transfer between the photons and the molecules during their interaction. A change in the molecular polarization potential — or amount of deformation of the electron cloud — with respect to the vibrational coordinate is required for a molecule to exhibit a Raman Effect. The amount of the polarizability change will determine the Raman scattering intensity. The pattern of shifted frequencies is determined by the rotational and vibrational states of the sample. Infrared spectroscopy also yields similar, but complementary information. The different scatterings along with the Raman scattering is represented in figure 2.15.

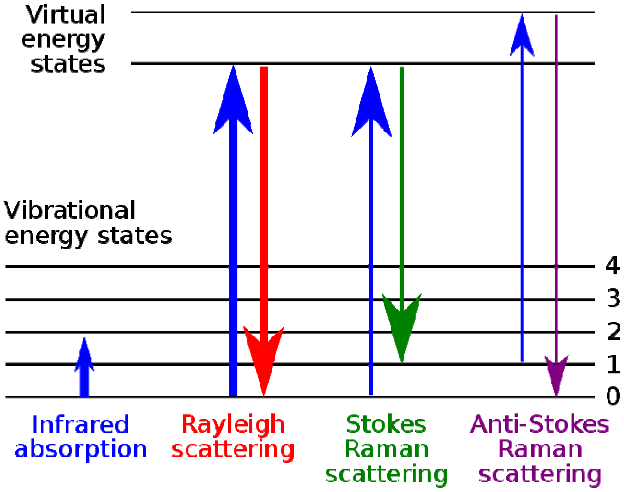

Figure. 2.15: Schematic representation of Raman scattering

In a typical Raman spectrometer, the sample is illuminated with a laser beam, and light from the illuminated spot is collected with a lens and sent through a monochromator.

Wavelengths close to the laser line due to elastic Rayleigh scattering are filtered out while the rest of the collected light is dispersed onto a detector.

Spontaneous Raman scattering is typically very weak, and as a result the main difficulty of Raman spectroscopy is in separating the weak inelastically scattered light from the intense Rayleigh scattered laser light. Historically, Raman spectrometers used holographic gratings and multiple dispersion stages to achieve a high degree of laser rejection. In the past, photomultipliers were the detectors of choice for dispersive Raman setups, which resulted in long acquisition times. However, modern instrumentation almost universally employs notch or edge filters for laser rejection and spectrographs (either axial transmissive (AT), Czerny-Turner (CT) monochromator, or FT (Fourier transform spectroscopy based), and CCD detectors.

Raman microspectroscopy (micro Raman Spectroscopy)

Micro Raman spectroscopy is a technique that uses a specialized Raman spectrometer to measure the spectra of microscopic or very thin samples. It is analogous to the use of ATR crystal in infrared spectroscopy. In general terms, a Raman spectrometer is integrated with a Raman microscope. Different types of lasers may be used to excite a microscopic sample at different wavelengths so that the micro Raman spectrometer can collect and analyze the vibrational spectra. The Raman spectrometer portion of the micro Raman spectrometer is an optical instrument for measuring the intensity of light relative to its Stokes shift from the wavelength of the exciting laser light. This shift is given in wave-numbers. A beam of light, collected from the sample, enters the device and is separated into its Stokes shifted frequencies by a diffraction grating. The separated light is then focused onto a CCD array detector where the intensity of each frequency is then measured by an individual pixel on the array. The CCD output is fed to a computer resulting in a spectrum which displays the intensity of the inelastically scattered light in wave-numbers relative to the wavelength of the exciting laser. A schematic block diagram of a typical spectrometer is given in figure 2.16.

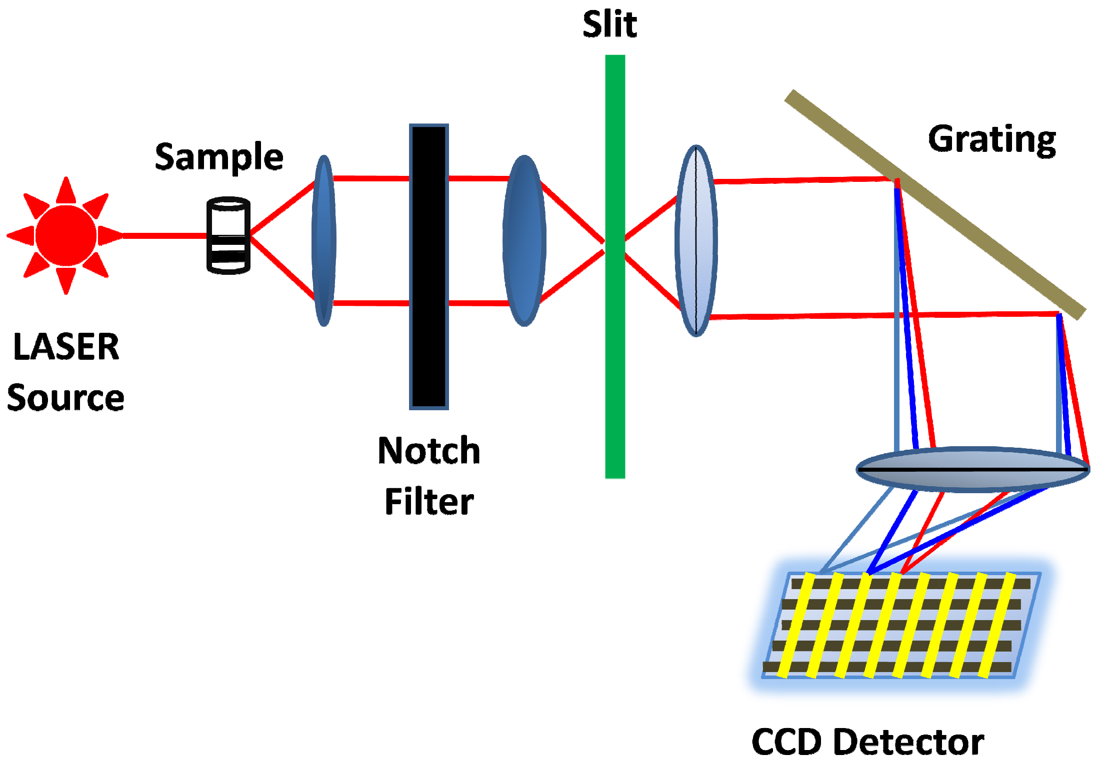

Figure. 2.16: A typical micro Raman spectrometer

References

1. B.D. Cullity, *Elements of X-ray diffraction.,* Addison-Wilson Publishing Comp. Inc., USA, 1959.

2. H.P. Klug, L.E. Alexander, *X-ray diffraction procedures.,* Wiley-Interscience Publication, New York, USA 1974.
3. P. W. Atkins, Physical Chemistry, 4th Edition, ELBS, Oxford, 1990.
4. C. N. Banwell and E. M. McCash, Fundamentals of Molecular Spectroscopy, 4th Edition, Tata McGraw-Hill publishers Ltd., New Delhi,2000.
5. C. Poole, *Electron Spin Resonance: a Comprehensive Treatise on Experimental Techniques, Editions 1, 2:* Interscience Publishers, New York, (1967), (1983).
6. A. J. Weil, J. R. Bolton, and J. E. Wertz, *Electron Paramagnetic Resonance, Elementary Theory and Practical Applications:* Wiley-Interscience, New York, (1994).
7. A.G. Bell, Am. J. Sci. 20, 305 1880.
8. A. Rosencwaig, *Photoacoustics and Photoacoustic Spectroscopy*, R.E. Krieger Publishing Company, Malabar, Florida, USA 1980.
9. A. Rosencwaig and A. Gersho, Science 190 (1975) 556
10. A.R.Dhobale, M.Kumar, A.G.Page and M.D.Sastry, *Bhabha Atomic Research Centre External Report* BARC/96/E/020 (1996).
11. A.Rosencwaig and A.Gersho, J.App. Phys. 47 (1976) 64
12. Cess Ronda (Edt.), Luminescence: From theory to applications: Wiley-VCH, Weinheim, Germany 2008

13. M.J.Puska, R.M.Nieminen, Rev. Mod. Phys. 66 (1994) 841
14. D. B. Cassidy, K. T. Yokoyama, S. H. M. Deng, D. L. Griscom, H. Miyadera, H. W. K. Tom, C. M. Varma, A. P. Mills Jr, Phys. Rev. B 75 (2007) 085415
15. M. Hasegawa, M. Tabata, M. Fujinami, Y. Ito, H. Sunaga, S. Okada, S. Yamaguchi, Nucl. Instrum. Methods B 116 (1996) 347
16. S. Damrefaer, T. Bretagnon and D. Kerr, J. Appl. Phys. 74 (1993) 884
17. M. Hasegawa, M. Tabata, T. Miyamoto, Y. Nagashima, T. Hyodo, M. Fujinami and S. Yamaguchi, Mat. Sci. Forum, 175 (1995) 269.
18. P. Asoka-Kumar, K.G. Lynn and D.O. Welch, J. Appl. Phys. 76 (1994) 4935.
19. W.H. Zachariasen, J. Am. Chem. Soc. 54 (1932) 3841.
20. R.A.B. Devine, Nucl. Instrum. Meth. B 91 (1994) 378.

Chapter-III

Spectroscopic investigations of the borosilicate waste glasses prior to irradiation

3.1. Introduction

The HLW generated from the reprocessing of spent nuclear fuels contains almost all elements of the periodic table. It is clear from the earlier discussion that the borosilicate based glass containment for HLW storage experiences radiation damage due to the decay of its radioactive component [1]. Also it is known that this radiation damage can significantly alter the properties of the various metal ions present in the high level waste [2]. The solubility and leachability (migration) of any metal ion is dependent on its oxidation state and coordination geometry [3]. Therefore in order to investigate the radiation induced changes in these parameters, it is necessary to do speciation studies of these metal ions prior to irradiation. This chapter deals with the speciation studies of various metal ions expected to be present in the Trombay nuclear waste glass by spectroscopic techniques. By virtue of their non-invasive nature spectroscopic techniques are best suited for these kinds of investigations.

The metal ions chosen for these studies are Cr, Cu, Fe and Mn from transition metal (TM) series, and Eu and Gd from rare earths (RE). Cr, Fe and Mn are expected to be present in the HLW in large quantities (total salt content- 317gm/L) as corrosion products. Though Cu is not expected to be present in the HLW, it has been chosen as a spectroscopic probe. Due to the broad radial distribution of the outer d electron orbital functions, these transition metal ions are known to be good probes for investigating the crystal field [4]. The RE ions chosen here, in their trivalent state, are considered as possible surrogates for the trivalent minor actinides [5]. Moreover, they can mimic trivalent plutonium Pu(III) in glassy matrices, which was found to be more soluble in borosilicate glasses than the usual Pu(IV) [6]. The spectroscopic techniques employed here in these studies are UV/visible absorption technique, Photoluminescence (PL), Photoacoustic Spectroscopy (PS) and Electron Paramagnetic Resonance (EPR) techniques. In addition to this, the Judd-Ofelt parameters and various radiative properties for one of the glass namely, Eu-glass was evaluated from its PL data. These investigations throw light on the covalency and site occupancy of the metal ion in the glassy system.

3.2. Experimental Details

The glass samples were prepared at Waste Management Division, Waste Immobilization Plant-BARC. All the chemicals used for the sample preparation were of AR grade. At first, required amounts of glass network formers namely SiO_2 and H_3BO_3 and network modifiers e.g. $Ba(NO_3)_2$ and $NaNO_3$, were taken and mixed thoroughly in an agate mortar so as to get the base glass. For the TM and RE doped glasses, required amounts of metal oxides were individually added in the above base glass composition appropriately. For all the glass samples, the ratio of Na_2O to BaO and SiO_2 to B_2O_3 were maintained constant at 1.2 and 1.76, respectively. The amount of the metal oxide was chosen so that it formed no separate phase in the glass. The powdered mixtures were ground and transferred into a platinum crucible and heated at 700^oC for 2 hours for the completion of calcinations and then melted at 1000^oC. The melt was maintained at

1000°C for 4 hours to ensure homogenization. The free flowing melt was quenched between two stainless steel plates. After that, the glass samples were ground thoroughly in agate mortar-pestle and sieved through a specified sieve of ASTM 200 mesh size so as to obtain a homogenous powder. The compositions for all the glasses are given in table-3.1.

To ensure the formation of glassy phase, X-ray diffraction (XRD) patterns were recorded using a Philips PW 1710 X-ray diffractometer with nickel filtered Cu-K_α radiation. Absorption studies in the wavelength range 200-1100 nm were carried out on a Jasco V-350 UV/Vis spectrophotometer at ambient conditions. Wherever absorption spectra of the samples could not be recorded, like in the case of Mn glasses, PS studies were performed. The PS signal from a sample is obtained by detecting the heat generated through the non-radiative relaxation released by the sample after absorbing a modulated incident light. PS spectra in 350-900 nm range were recorded on an indigenously built PS spectrometer with a 450w tungsten-halogen lamp as the excitation source. PS spectra were normalized for variations in the intensity of excitation source profile by normalization of sample spectra to that of a carbon spectrum.

PL experiments were done at room temperature on an Edinburgh CD-920 Time Resolved Fluorescence Spectrometer unit (Edinburgh Analytical Instruments, Livingston, UK) with Xe flash lamp. The spectra obtained were analyzed by F-900 software provided by Edinburgh. EPR experiments were carried out on a Bruker ESP 300 spectrometer operating at X band frequency (9.6 GHz) using 100 kHz field modulation. The magnetic field was scanned from -4.5mT (-45 Gauss) to 1200 mT (12 kilo Gauss) with di-phenyl picryl hydrazyl (DPPH) as the field marker.

Starting material (In mol %)	Base Glass (A)	Cr-Glass (B)	Cu-Glass (C)	Fe-Glass (D)	Mn-Glass (E)	Eu-Glass (F)	Gd-Glass (G)
SiO_2	47.34	47.11	46.88	46.17	46.88	46.17	46.17
Na_2O	14.30	14.22	14.15	13.93	14.15	13.93	13.93
B_2O_3	26.80	26.67	26.53	26.13	26.53	26.13	26.13
BaO	11.56	11.50	11.44	11.27	11.44	11.27	11.27
Cr_2O_3	---	0.5	---	---	---	---	---
CuO	---	---	1.00	---	---	---	---
Fe_2O_3	---	---	---	2.5	---	---	---
MnO	---	---	---	---	1.00	---	---
Eu_2O_3	---	---	---	---	---	2.5	---
Gd_2O_3	---	---	---	---	---	---	2.5

Table 3.1: Composition of the borosilicate glass system

EPR data acquisition and analysis was done by WIN-EPR software and the EPR simulation studies were carried by Simfonia software from Bruker. For XRD and EPR investigations, the powdered forms of the glass samples were taken where as for absorption and luminescence studies, polished glass samples in the form of plates of 2 mm thickness were taken.

3.3. Results and discussion

A.X-ray diffraction Investigations

XRD patterns of all the glass samples are shown in figure-3.1. These are characterized by the presence of a broad hump in between the scattering angle (2θ) 10^0-20^0. This confirms the uniform glassy state of all the samples.

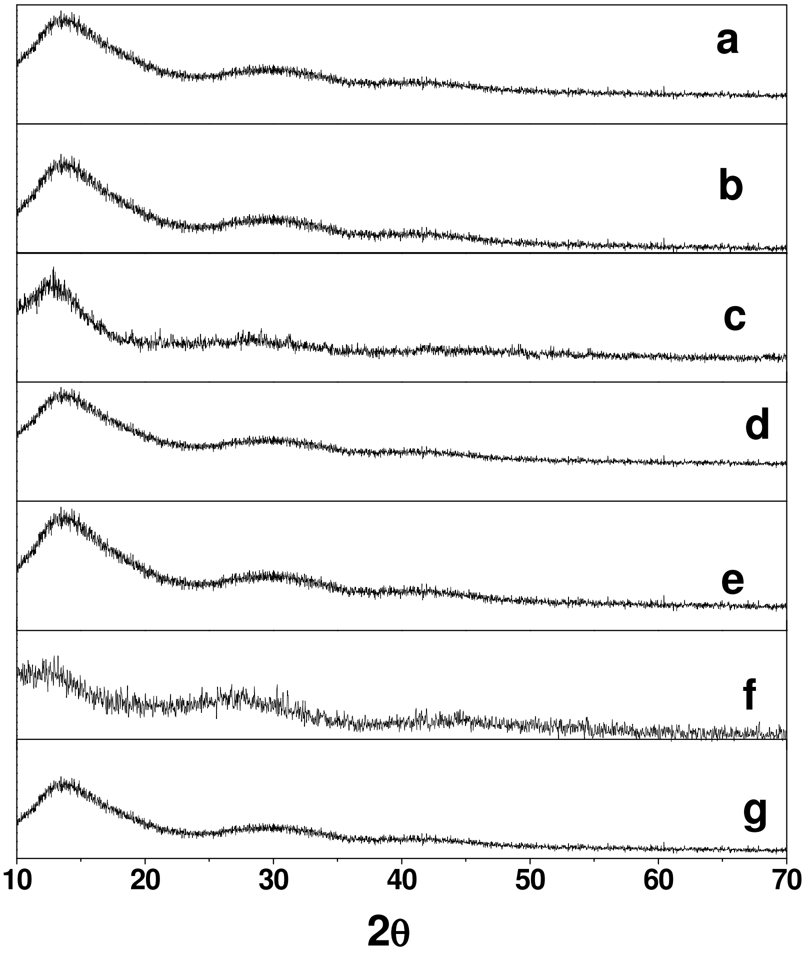

Figure 3.1. XRD patterns of the transition metal and rare earth incorporated sodium barium borosilicate glasses, (a) the base glass without any metal ion (b) Cr glass (c) Cu-glass (d) Fe- glass (e) Mn- Glass (f) Eu-Glass and (g) Gd-glass.

B. UV-Vis Absorption Studies

Figure 3.2a shows the UV-Vis absorption spectra of the barium borosilicate base glass in the wavelength region 200-1100nm. When an electron in the valence band interacts with electromagnetic radiation, it can have two types of allowed optical transitions which are well documented by Davis and Mott theory [7].

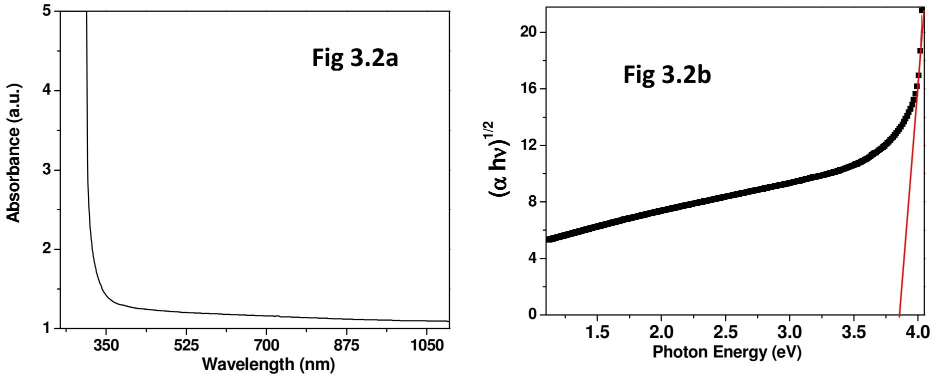

Figure 3.2a. UV/Vis spectrum of the sodium barium borosilicate base glass with out any transition metal ion; Figure 3.2b. Band gap profile of the sodium-barium borosilicate base glass

According to this theory, the absorption coefficient, $\alpha(v)$, as a function of photon energy (hv) for allowed indirect optical transitions is given by the following expression.

$$\alpha(v) = C\,(hv-E_g^{opt})^{1/2} / hv \qquad (1)$$

Here, C is the proportionality constant and E_g^{opt} is the optical band gap. The band gap for a system thus can be determined by plotting $(\alpha hv)^{1/2}$ against the photon energy and extrapolating the linear portion of the graph to the photon energy axis at zero absorbance. Figure 3.2b shows the band gap profile plot for the base glass. From this, the band gap of the glass was determined to be ~3.8±0.2 eV.

The UV-Vis absorption spectra of the individual glasses are discussed below in separate sub-headings.

1. Cr doped Glass

Figure 3.3a and 3.3b show the optical absorption and band gap profile of the Cr glass samples. From this, the indirect band gap of the system was found out to be 3.6±0.2 eV. The absorption spectrum of the Cr-glass showed weak absorption bands at 385 and 470 nm and a broad absorption band at 650 nm. In general, Cr in its 3+ oxidation state (d^3 configuration) has large octahedral site preference energy (OSPE) and thus prefers to stabilize in an octahedral geometry where it exhibits three absorption bands due to three spin-allowed transitions $^4A_{2g} \rightarrow {}^4T_{2g}$ (F), $^4A_{2g} \rightarrow {}^4T_{1g}$ (F) and $^4A_{2g} \rightarrow {}^4T_{1g}$ (P).

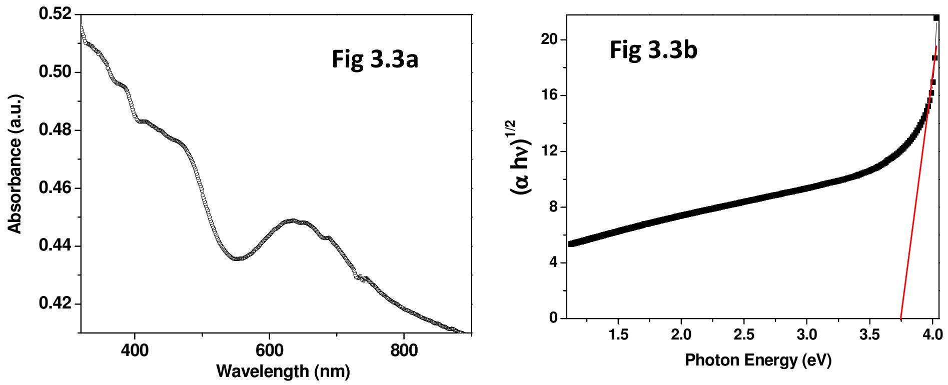

Figure 3.3a. Absorption spectrum of the Cr-glass; Figure 3b. Band gap profile of the Cr-glass

In the present case, the broad band observed at 650 nm was assigned to the transition $^4A_2 \rightarrow {}^4T_2$ (F). The other two bands at 470 and 385 nm were assigned to $^4A_2 \rightarrow {}^4T_1$ (F) and $^4A_2 \rightarrow {}^4T_1$ (P) transitions respectively. The crystal field parameter Dq was evaluated from the 650nm band and was found out to be 1538 cm^{-1}. This value is in the expected range for Cr^{3+} ions in octahedral geometry [8]. Table 3 presents a comparison of the experimental and reported values of various spectroscopic parameters of the different transition metal glasses. The value of Dq is also related to the position of the other two absorption bands by the following equations [8].

$$E\,(v_2) = 15Dq + 7.5B - ½(225B^2 + 100Dq^2 - 180DqB)^{1/2} \qquad (2)$$

$$and\ E\,(v_3) = 15Dq + 7.5B + ½(225B^2 + 100Dq^2 - 180DqB)^{1/2} \qquad (3)$$

Here B is one of the inter-electronic repulsion parameters known as the Racah parameter. By solving these two equations, the value of B was evaluated to be 731 cm^{-1} which is in agreement with the theoretical values for d^3 ions in distorted octahedral geometry [8].

2. Cu doped Glass

The UV-visible absorption spectrum and the band gap profile for the copper incorporated glass are shown in figure 3.4a and 3.4b respectively. A single absorption band in the wavelength region 700-750 nm observed in this case is assigned to d-d transition in Cu^{2+}. The free ion term for Cu^{2+} (d^9) is ^2D. In octahedral crystal field it splits into ^2E_g and $^2T_{2g}$ with ^2E_g being the lower level. Due to Jahn–Teller effect the ^2E_g level splits into $^2A_1$ and $^2B_1$, and $^2T_{2g}$ level into ^2E and $^2B_2$. Therefore Cu^{2+} is rarely found in regular octahedral site. Here the broad absorption band observed is attributed to $^2B_1 \rightarrow {}^2B_2$ transition of Cu^{2+} in a distorted octahedral geometry [9]. The broadening of this band may be attributed to the super position of three-electron transition in d orbitals corresponding to $^2B_1 \rightarrow {}^2E$, $^2B_1 \rightarrow {}^2A_1$ and $^2B_1 \rightarrow {}^2B_2$ transitions [10]. By applying the Davis and Mott theory, the band gap for the Cu-glass was determined to be 3.5±0.3 eV.

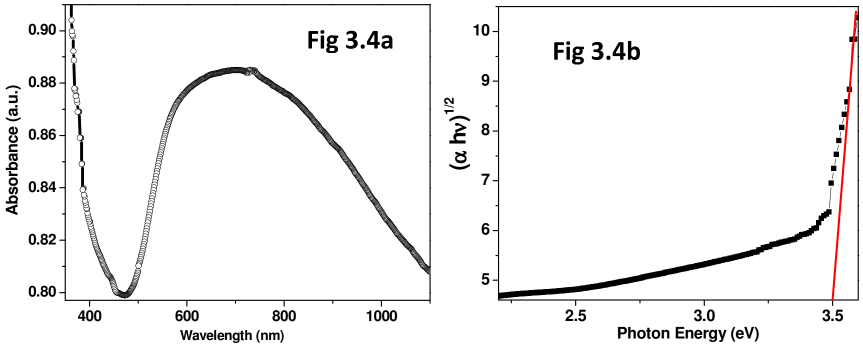

Figure 3.4a. Absorption spectrum of the Cu-Glass; Figure 4b. Band gap profile for the Cu-glass

3. Fe doped Glass

Figures 3.5 a and b show the absorption and band gap profile spectrum respectively for the Fe incorporated borosilicate glass. The indirect band gap for system was evaluated by previously discussed procedure and was found to be 3.2±0.3 eV. The absorption spectrum is characterized by a weak absorption band at 448 nm which is attributed to Fe^{3+} in distorted octahedral symmetry as discussed below.

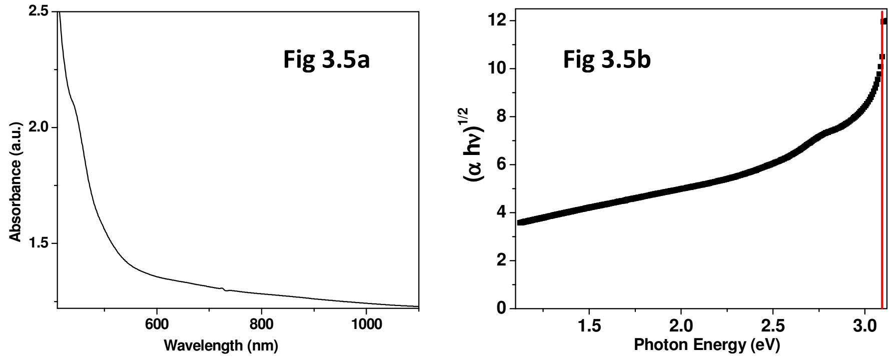

Figure 3.5 a. Absorption spectrum for the iron doped glass; Figure 5 b. Band gap profile for the Fe-glass

For iron in its 3+ oxidation state (d^5 configuration), there are no spin-allowed transitions. Accordingly in the absorption spectrum, only weak bands occur corresponding to spin-forbidden transitions. The 448 nm band observed in this case was attributed to the $^6A_{1g}(S) \rightarrow {}^4T2_g$ (G) transition. This observed band position was compared with those found for many glassy systems containing iron, which indicated that Fe ions are indeed present in 3+ state in a distorted octahedral geometry [11–13]. It is worth noting here that the ionic radius of Fe^{+3} ion (0.064 nm) is closer to that of Na^+ ion (0.097 nm) as compared to that of Ba^{2+} ion (0.134 nm). So it can be assumed that, Fe^{+3} ions occupy the network modifier sites of sodium ions in these glasses.

The Mn incorporated sodium-barium borosilicate glasses were intensely colored and no UV-Vis absorption studies could be performed on the samples. The absorption spectra for such samples were recorded by PS technique as described earlier in the experimental section.

In case of Eu and Gd glasses also, the UV-Vis spectra could not be recorded because of sample limitations. In these glasses, the excitation spectra obtained from PL studies were treated as equivalent to absorption spectra.

C. Photoacoustic Spectroscopic (PS) Investigations

The normalized absorption spectrum recorded for 1 % Mn doped glass by photoacoustic spectroscopy is shown in figure 3.6.

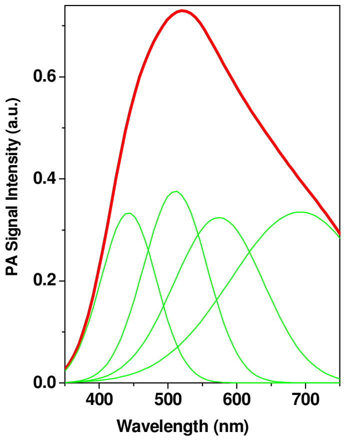

Figure 3.6. Normalized PS spectrum for the Mn-glass

The broad absorption in the range 480-580 nm with a peak around 520 nm also revealed a few shoulders. Based on the current literature data for Mn, it was not possible to fit such a broad absorption peak into a single species. Therefore the broad band was fitted into multiple peaks by a Gaussian fitting program. The best fit was obtained only with four Gaussian peaks at ~ 448, 520, 575 and 690 nm as shown in the figure.

It was not possible to directly correlate the observed peaks to one type of Mn ion. Therefore, to unambiguously assign the observed peaks in case of Mn, a concentration variation study was performed and samples with 0.1, 0.25, 0.5, 1 and 2.5 % of Mn were prepared and the individual PS spectra were analyzed. Figure 3.7 shows the variation of the peak-area under each PS spectrum as a function of Mn concentration. From the spectrum it was observed that, the 448 and 520 nm peaks behave similarly showing saturation of the signal intensity above 1% Mn, while 575 and 690 nm peaks were observed to increase upto 2.5% Mn.

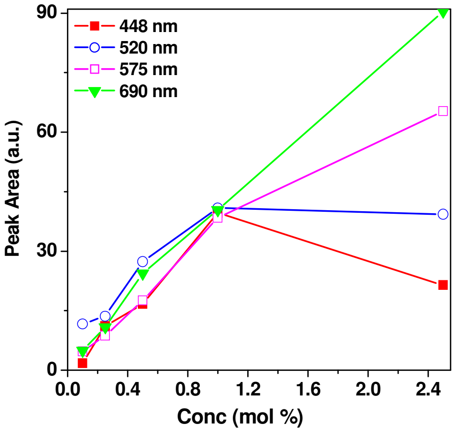

Figure 3.7. Plot of concentration of Mn with the normalized PS signal intensity

Literature reports on alkali borosilicate and zinc phosphate glasses have reported absorption peaks at 445 and 505 nm and assigned them to $^6A_1g(S) \rightarrow {}^4T_{2g}$ (G) and $^6A_Ig(S) \rightarrow {}^4T_Ig(G)$ transitions of Mn^{2+} ions respectively [14, 15]. In sodium tetraborate and Li-Na and Na-K mixed borate glasses also a broad absorption centered around 505 nm was reported and attributed to $^6A_{1g}(S) \rightarrow {}^4T_{1g}(G)$ transition of Mn^{2+} ions [16, 17]. Therefore, in the present study of Na-Ba-borosilicate glass, the absorption peaks at 448 and 520 nm were attributed to $^6A_1g(S) \rightarrow {}^4T_{2g}$ (G) and $^6A_Ig(S) \rightarrow {}^4T_Ig(G)$ transitions of Mn^{2+} respectively. In addition a shoulder like structure was observed in glass samples at

~550 nm which on Gaussian fitting lead to observation of peaks around 575 and 690 nm. Maksimova et al have studied optical absorption spectra of Mn doped KI and KBr in the visible region and observed absorption and excitation spectra peaks at 575 and 690 nm [18]. These peaks were attributed to ligand-to-metal charge transfer (LMCT) transitions of MnO_4^- and MnO_4^{2-} respectively. The peaks obtained in the experiments are in good agreement with the work reported by Maksimova et al., thus these two were attributed to MnO_4^- and MnO_4^{2-} species in the borosilicate glass. Because of the unavailability of the absorbance data, the band gap profile could not be obtained for the Mn-glass. A comparison of the band gaps of the different transition metal doped glasses is given on table-3.2. From the table it can be seen that, on incorporation of metal ions, the overall band gap of the glass decreases. This is due to the formation of additional levels in between the valence and conduction band of the host glass which is well reported. In case of Mn, since no UV-Vis absorption data could be obtained, the band gap profile could not be evaluated.

The results of the absorption maxima obtained for the transition metal incorporated glasses are summarized in table-3.3.

D. Photoluminescence (PL) Studies

The borosilicate base glass without any dopant ion did not show any PL spectrum. The Pl investigations of the doped glasses are discussed below.

1. Cr doped glass

Figure 3.8 shows the PL spectrum of the Cr-glass sample at room temperature. Characteristic peak due to Cr^{3+} is seen at 780 nm due to the transition $^4T_2$-$^4A_2$. Cr^{5+} signal could not be observed with the present set of instrument as its emission usually occurs in the μm region. Graft et al [28] have observed this kind of PL spectrum for Cr^{3+} ion previously.

Glass Sample	Base Glass	Cr-Glass	Cu-Glass	Fe-Glass
Band Gap (eV)	3.8	3.6	3.5	3.2

Table-3.2:Band gap profile of the glasses

Glass sample	Absorption Maxima (nm)	Dq (cm^{-1})/ Geometry	References
Cr-glass	650 (650) 470 (450) 385 (370)	1538 (1574)	10, 19
Cu-glass	700-750 (750)	Distorted Oh	20
Fe-glass	448 (450)	Distorted Oh	21, 22
Mn-glass	448 & 505 (445 & 520)	Mn^{2+}	23,24,25,26
	575 (575)	MnO_4^-	27
	690 (690)	MnO_4^{2-}	27

Table-3.3: Absorption maxima of the different glasses, The figures in the bracket are the literature values

2. Cu doped glass

Cu in its divalent state is photoluminescence inactive. However, Cu^+ is PL active. In the PL studies of the Cu-glass, no signal was observed suggesting the absence of any Cu^+ species.

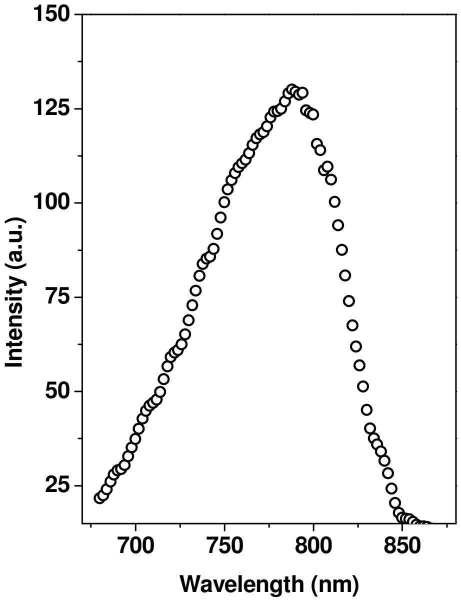

Figure 3.8. PL spectrum of the Cr incorporated alkali barium borosilicate glass

3. Fe doped glass

The PL spectrum for the Fe incorporated glass (figure 3.9) showed a broad band at ~630 nm attributed to the $^4T_1$ (^4G) → $^6A_1$ (^6S) transition of Fe^{3+} in tetrahedral coordination. The PL decay time for the transition was calculated to be 1.03 ms which is in accordance with the reported values for Fe in trivalent state [29].

4. Eu doped glass

The PL spectrum (figure 3.10) of the Eu doped glass with 243 nm excitation showed peaks at 578, 591, 611, 653 and 704 nm due to transition of electrons from $^5D_0$ state to the ^7F_J (J = 0 to 4 respectively) states typical of Eu^{3+}.

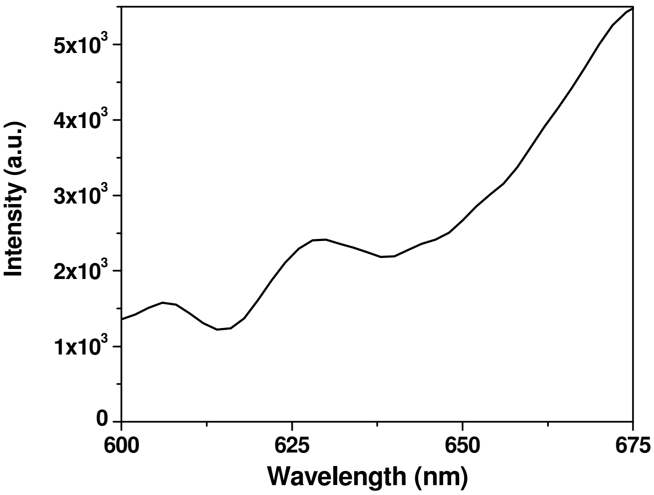

Figure 3.9. PL spectrum for the Fe incorporated borosilicate glass

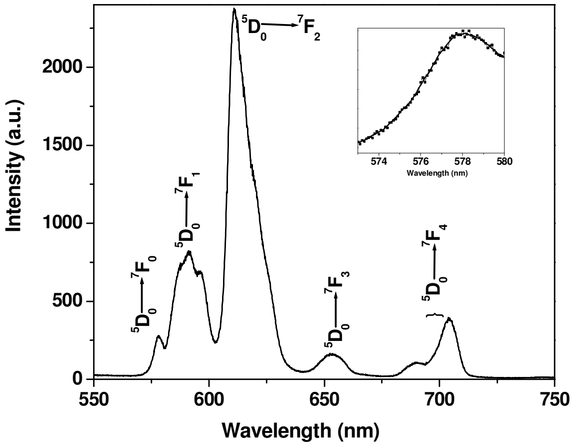

Figure 3.10- Emission spectrum for Eu doped borosilicate glass (λ_{ex} = 243 nm). The inset figure shows the $^5D_0 \rightarrow {}^7F_0$ transition at 578 nm.

Here, the red emission observed at 611 nm involving $\Delta J = \pm 2$ transition is an electric dipole transition, while the orange emission at 591 nm is a typical magnetic dipole allowed transition ($\Delta J = \pm 1$). The bands at 653 and 704 nm are due to forbidden $^5D_0 \rightarrow {}^7F_3$ and electric dipole allowed $^5D_0 \rightarrow {}^7F_4$ transitions respectively. The $^5D_0 \rightarrow {}^7F_0$ transition seen at 578 nm is a completely forbidden transition (shown separately as figure 15 inset). Peaks corresponding to radiative transitions to higher ^7F_J states ($^7F_5$ and $^7F_6$) were not observed in the present glass system. No additional peaks were observed in the wavelength range 400-550 nm indicating the absence of transitions from higher ^5D_n levels of Eu^{3+}. Moreover, this also meant absence of Eu^{2+}.

The excitation spectrum of the borosilicate glass with Eu^{3+} at λ_{em} = 611 nm is shown in figure 3.11. The prominent band at 243 nm is due to the Eu^{3+}-O^{2-} charge transfer [30,31] and the other smaller bands seen at 320, 362, 383 and 395 nm are assigned to the f-f transitions from the $^7F_0$ ground state to $^5H_3$, $^5L_9$, $^5G_3$ and $^5L_6$ levels respectively [32]. The PL decay time for the Eu^{3+} doped samples was evaluated to be 2.7 ms.

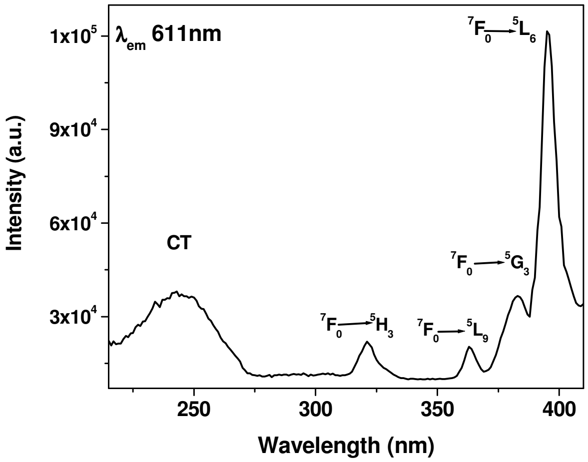

Figure 3.11- Excitation spectrum for the Eu incorporated borosilicate glass (λ_{em} = 611 nm).

5. Gd doped glass

The PL emission spectrum for the Gd-glass samples, recorded at 250 nm excitation is shown in figure 3.12. The spectrum comprises of a sharp transition at 310 nm and a small kink at 307 nm. The emission at 310 nm is due to the forced electric-dipole transition of the lowest excited state of $^6P_{7/2}$ to the ground state $^8S_{7/2}$ of the Gd^{3+} ions, while the emission at 307 nm is due to the magnetic-dipole transition $^6P_{5/2} \rightarrow {}^8S_{7/2}$ [33, 34]. In case of Gd-glass sample, the decay time value was obtained to be 3.5 ms which is in accordance with the reported values [35, 36]. The decay time curves for both Eu and Gd glasses are shown in figure 3.13.

In case of the Gd incorporated glass, the occurrence of 310 nm emission in predominance, due to the forced electric-dipole transition, suggest that the metal ion is in a lower symmetric environment [37].

Thus, in both the RE (Eu and Gd) doped glass it was observed that, the metal ion is in a lower symmetric environment. The results obtained in this work allow us to suppose that, although the RE^{3+} ions are immersed in an amorphous matrix, some degree of local order persists in the vicinity of these ions. Moreover, it seems that there exists a unique environmental site distribution for the RE ions in the borosilicate glass.

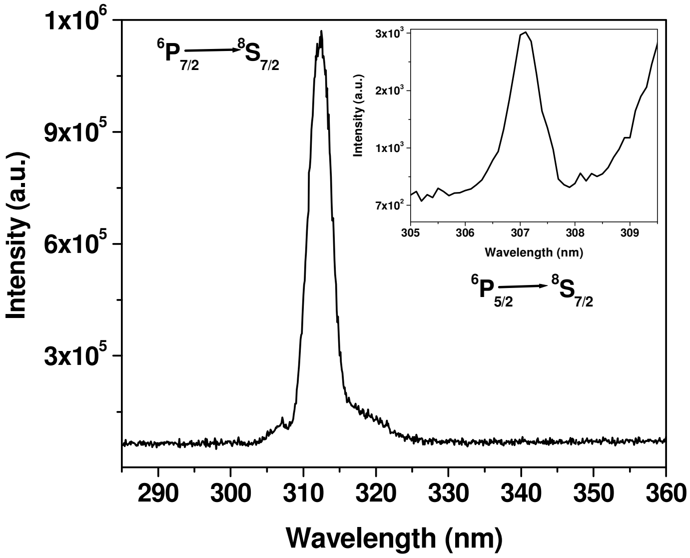

Figure 3.12. Emission spectrum for Gd doped borosilicate glass (λ_{ex} = 250 nm). The inset figure shows the transition at 307 nm.

6. Judd-Ofelt Analysis of the Eu-Glass samples-:

The Judd–Ofelt (J-O) analysis of the emission spectrum is a powerful tool for calculating the parity-forbidden electric-dipole radiative transition rates between the various levels of a rare earth ion [38, 39]. Since, for the present study, the J-O parameters have been estimated by PL studies, it could only be done for the Eu-glass. For all these calculations, the corrected spectra (with respect to source and detector response) were taken into consideration. Through these analyses, the local environment around the metal ion and the M–L bond covalency can be interpreted. Apart from this, the radiative transition rate (A_R), radiative lifetimes (τ_R) and luminescence branching ratios (β_R) can also be computed. It is possible to determine the J-O intensity parameters Ω_λ (where $\lambda = 2,\ 4$ and 6 etc.) based on the emission spectral data as shown by various authors [40-43].

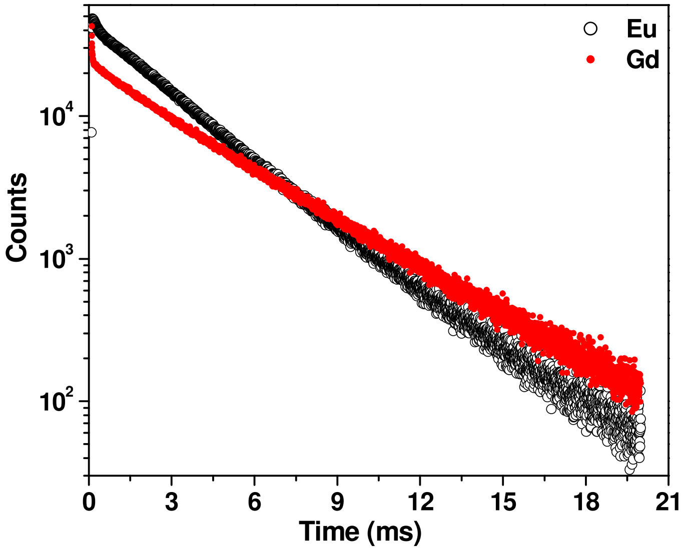

Figure 3.13. Decay time curves for Eu and Gd in the alkali borosilicate glasses

For a particular transition, the emission intensity (I) can be considered as proportional to the area under the emission curve for that transition. Also, the intensity will be proportional to the radiative decay rate of the transition (A_R).

$$I = hcv\ A_R N \ \alpha \text{ (Area under the curve)} \qquad (4)$$

Here $hc\nu$ is the energy separation in the initial and final levels. N is the population of the $^5D_0$ level (in case of Eu^{3+}). The $^5D_0 \rightarrow {}^7F_{2,4 \text{ and } 6}$ transitions are electric dipole allowed whose radiative decay rates can be represented by the following equations as shown by Malta et al [44].

$$A_{R(ed)}= \left\{\left(\frac{64\pi^4 e^2 \upsilon^3}{3h\ (2J+1)}\right)\chi\right\}\sum_J \Omega_J \langle \| \ U^{(J)} \ \| \rangle^2 \qquad (5)$$

Here the factor $\chi = \frac{n(n^2+2)^2}{9}$ is known as the Lorentz local field correction factor (that converts the external electromagnetic field into an effective field at the location of the active center in the medium) and n is the refractive index of the glass medium. $\|U^J\|$are the doubly reduced matrix elements corresponding to the $^5D \rightarrow {}^7F_J$ transitions of Eu ion; e is the electron charge and v is the transition energy in cm^{-1}. Neglecting the J-J mixing, it is found that, the intensities of the transitions solely depend on the respective matrix elements.

For the present glass system, the index of refraction was calculated by standard Gladstone and Dale fomula as suggested by Larsen and Burman [45] and also illustrated in Lange's Hand book of Chemistry [46].

For the calculations of Ω_J values in Eu incorporated borosilicate glass, the intensity of $^5D \rightarrow {}^7F_1$ transition, which is a magnetic dipole allowed transition, was taken as the reference. The transition rate ($A_{R(md)}$) of this magnetic dipole allowed transition is represented by the following equation [47].

$$A_{R(md)} = \left\{\left(\frac{64\pi^4 \nu^3}{3h(2J+1)}\right)\right\} n^3 S_{md} \tag{6}$$

Here S_{md} is the magnetic-dipolar transition line strength and is independent of host matrix. For the present system, its value was taken as 9.6×10^{-42} esu^2 cm^2 as reported by Werts et al [42] and Weber et al [48].

The total radiative decay rate (A_R) value was calculated from the ratio of the sum of the areas under the $^5D_0 \rightarrow {}^7F_J$ transitions$\left(\sum \int I_J dv\right)$, to area under the curve of the $^5D_0 \rightarrow {}^7F_1$ transition$\left(\int I_1 dv\right)$.

$$\frac{\left(\sum \int I_J dv\right)}{\left(\int I_1 dv\right)} = \frac{A_R}{A_{Rmd}} \tag{7}$$

The J-O intensity parameters, Ω_J were calculated from the respective A_{Red} values as per equation 5. The values for the reduced square matrix elements $\|U^{(J)}\|$ for the $^7F_2$ and $^7F_4$ transitions were taken as 0.0032 and 0.0023 respectively [42, 49–51].

Since, the $^5D_0 \rightarrow {}^7F_6$ transition was not observed in the glass samples, its J-O parameters could not be evaluated.

The total radiative lifetime can be represented as the reciprocal of the total radiative decay rate i.e. $\tau_{R} = \frac{1}{A_R}$. From the experimental decay time (τ_f) and τ_R values, the τ_{NR} i.e. the non radiative life time was calculated by the following formula.

$$\frac{1}{\tau_f} = \frac{1}{\tau_R} + \frac{1}{\tau_{NR}} \tag{8}$$

Similarly, the branching ratios $\left(\beta_J = \frac{A_J}{\sum A_J}\right)$ for the different excited states and the overall quantum efficiency $\left(\eta = \frac{\frac{1}{\tau_R}}{\frac{1}{\tau_f}}\right)$ were calculated by standard procedures. All these parameters for the Eu^{3+} ion in the borosilicate glass host are listed in table 3.4. The ${}^5D_0 \rightarrow {}^7F_3$ transition could not be accounted for by either the magnetic or electric dipole mechanisms. Its presence is considered to be a small deviation from theory at the level used in this work. However, some workers say that these transitions ‘borrow’ intensity from the ${}^5D_0 \rightarrow {}^7F_2$ transitions through higher order perturbations by the crystal field and show bands in the emission spectrum [41].

Transition	A_{Red} (s^{-1})	A_{Rmd} (s^{-1})	Ω_J (10^{-20} cm^2)	β_J (%)	η -	A_{total} (s^{-1})	τ_R (µsec)
${}^5D_0 \rightarrow {}^7F_1$	0	55.3	-	18.2	82	304	3.29
${}^5D_0 \rightarrow {}^7F_2$	213	0	6.57	70.1			
${}^5D_0 \rightarrow {}^7F_4$	27.4	0	1.81	9.03			

Table-3.4: J-O intensity parameters and radiative properties of the Eu^{3+} ion in the sodium barium borosilicate glass matrix.

The asymmetric ratio for the Eu^{3+} ion, (‘A’) is defined as the ratio of the intensity of the ${}^5D_0 \rightarrow {}^7F_2$ and the ${}^5D_0 \rightarrow {}^7F_1$ transitions (I_{611}/I_{591}). The electric dipole transition to ${}^7F_2$ is a hypersensitive transition, which is sensitive to the symmetry of the Eu^{3+} chemical environment. The intensity of the transition increases with increasing covalence of the ligands or decreasing site symmetry. On the contrary, the magnetic dipole transition is chosen as a reference because it is much less sensitive to Eu^{3+} environment. Gatterer et al have reported ‘A’ values between 3 and 4.2 for sodium borate, silicate or borosilicate glasses [52]. Calculated ‘A’ value for the present glass system is ~3 and agrees with the study of Gatterer et al. indicating the expected Eu^{3+} presence in low- symmetry sites.

The local site symmetry of the Eu^{3+} ion can also be characterized by the line position and the full width at half-maximum (FWHM) data of the $^5D_0$–$^7F_0$ emission band. This transition becomes allowed only cases where the site symmetry of the metal ion is C_{nv} or lower, due to the presence of a linear term in the Hamiltonian of the respective crystal field, and gains strength from mixing of J values in one or both of the levels described earlier [53]. In the present case, the band is centered at 578 nm with FWHM of 120 cm^{-1}. This value is close to that of Eu^{3+} in sodium borosilicate glasses as reported by Pucker et al [54]. As shown by Ollier et al, a lower value of the FWHM infers a smaller site distribution of the RE ions [55]. Here in case of the barium borosilicate glass, the FWHM is fairly large indicating a fairly large site distribution for the RE ion.

The site symmetry of the Eu^{3+} ion can also be determined from the number of Stark components observed as described below. For every J level, the maximum numbers of Stark components that one might expect are (2J + 1). In general, with decrease in the symmetry of the electric field, the number of Stark components into which a band is split, increases. Here in this case, for the F_1 transition, at least 3 components at 587, 591 and 596 nm are observed. Similarly for the F_2 transition, components at 610, 619 and 626 nm are observed. For the F_4 transition, 2 components at 689 and 704 nm are seen. The presence of multiple components can be either due to the presence of Eu^{3+}-ion in lower symmetry or due to the presence of 2 types of Eu^{3+}-species in higher symmetries. However, the presence of a single component for the F_0 transition, suggests that, there is only one type of Eu^{3+}-ion in a lower symmetry. Brecher et al have given a detailed account of the relationship of the symmetry of the Eu ion and the number of observed components in the emission spectrum [56]. Based on this, it can be argued that, the rare earth metal ion must be in symmetry equal to C_2.

The J-O intensity parameters (Ω_J) of the Eu^{3+} ion in the glass matrix reveal information regarding the covalence and surrounding of the metal ion. Jorgensen and Reisfeid have discussed the physical meaning of these parameters in one of their papers [57]. The parameter Ω_2 is related to the covalency and structural changes in the vicinity of the Eu^{3+} ion (short range effect) and Ω_4 is related to the long-range effects. A larger value of Ω_2 is an indication of a high covalence of the metal-ligand bonds and more distortion in the symmetry around the Eu^{3+} sites in that matrix compared to a matrix where the Ω_2 value is smaller [58, 59]. Large values for Ω_4 can be expected for organic ligands, because of low rigidity of these matrices.

The current trend in the J–O parameters ($\Omega_2 > \Omega_4$) has also been observed for various other glass matrices such as phosphate glass, sodium tellurite-phosphate glass, calcium alumino-borate glass and zinc borosilicate glasses etc. This confirms the covalency existing between the Eu^{3+} ions and surrounding oxygen ions. In table 3.5, a comparison of the J-O intensity parameters of Eu^{3+} in different glass hosts is presented.

Host	Ω_2 (10^{-20} cm^2)	Ω_4 (10^{-20} cm^2)	Ref.
Sodium Barium borosilicate Glass	6.57	1.81	Present Work
Zinc borosilicate Glass	7.75	4.10	60
Silicate Glass	5.61	3.47	61
Lithium barium borate glass	6.81	4.43	62
Zinc Borate Glass	9.5	7.0	63
Sodium telluro-phosphate Glass	5.29	1.89	64
Calcium alumino borate Glass	3.36	2.1	65
Phosphate Glass	4.1	1.2	66

Table-3.5: Comparison of the J-O intensity parameters for the $^5D_0 \rightarrow {}^7F_2$ and $^5D_0 \rightarrow {}^7F_4$ transitions of Eu^{3+} in various glass hosts.

E. Electron Paramagnetic Resonance (EPR) Studies

The EPR spectrum for the base glasses without any metal showed a very weak line at g ~ 4.300. This was attributed to Fe^{3+} in tetrahedral or lower geometry in the base glass. This iron impurity might be coming from the SS containers used for glass quenching in the glass preparation stage.

1. Cr doped glass

The room temperature experimental and simulated EPR spectrum of Cr-glass is shown in figure 3.14. While carrying out the EPR data analysis, the g values obtained by using the field marker (DPPH) were taken as inputs for the simulation experiments. The Hamiltonian parameters giving best correlation between experimental and simulated spectra were taken as the final parameters.

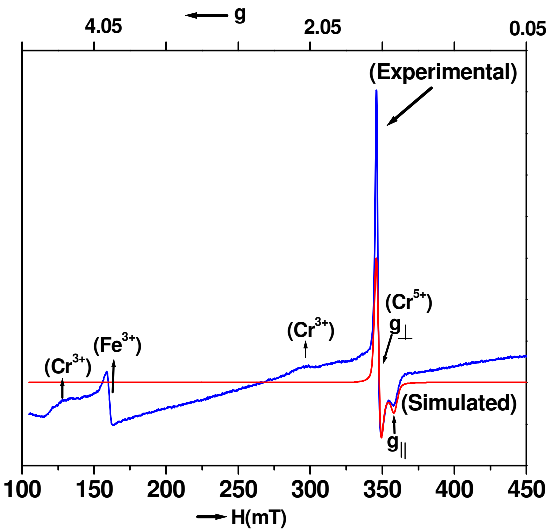

Figure 3.14. Room temperature experimental and simulated EPR spectrum of Cr-glass, the simulation was done for the 5+ species only, the upper axis shows the corresponding 'g' values for the resonances.

Apart from the Fe^{3+} signal at g=4, the spectrum shows a broad and weak signal at g ~ 2.02 with a positive shoulder at g_{eff} = 5.15 along with an intense and sharp signal at g=1.98. The weaker band at lower field adjacent to the iron signal, and the g =2.02 signal is attributed to isolated Cr^{3+} ions in rhombic or lower symmetry subjected to strong crystal field effects as suggested by Landry et al [67] and Ardelean et al [68]. Since Cr^{3+} contains three unpaired electrons (S=3/2) it is expected to give three fine transition in its EPR spectrum. However, the identifications of all fine transitions of Cr^{3+} is difficult because of its large zero field splitting (D=500 mT) and low intensities of fine transitions. These signals were analyzed using the following spin Hamiltonian parameters.

$$H = \beta H.g.s + D[S_z^2 - 1/3S(S+1)] + E(S_x^2 - S_y^2) \qquad (9)$$

Here *D* and *E* are the axial and orthorhombic crystal field terms respectively.

The broad line shapes observed can be attributed to the presence of short range ordering along with various small distortions of the local environment of the ions from site to site. Moreover, the symmetry axes of the ligand fields relative to the direction of the applied magnetic field are randomly oriented making the line shapes highly broadened. However, in case of a polycrystalline or single crystal samples of Cr, one does not come across this kind of broad resonance. For the intense and sharp signal, a best fit could be obtained via simulation assuming axial symmetry of the species with $g_{\perp}$=1.98 and $g_{\parallel}$=1.97. The resonance line having very narrow line width (ΔH< 1 mT) was attributed to Cr^{5+}. The formation of Cr^{5+} might be due to the partial oxidation of Cr^{3+} during the process of melting of the alkali barium borosilicate glass. These types of resonance signals arising from Cr^{5+} are well reported in other glassy matrices [69-73]. It is reported that, in oxide glasses usually Cr^{5+} ions give narrow resonance lines with g= 1.98.

2. Cu doped glass

The room temperature EPR spectrum for the Cu incorporated borosilicate glass (shown in figure 3.15) can be best interpreted by assuming axial symmetry of g and A tensors ($g_{||}$ $g_{\perp}$, $A_{\perp}$ and $A_{\perp}$). The spectrum shows four weak parallel components in the low field region and four well resolved perpendicular components in the high field region. Though the perpendicular components are not clear in the first derivative spectrum, it was well resolved in the second derivative spectrum (Figure 3.15 inset). The Hamiltonian parameters for the system calculated by simulation studies are as follows $g_{||}$ = 2.344 and $g_{\perp}$ = 2.0729, the hyperfine coupling parameters $A_{||}$ = 14 mT and $A_{\perp}$ = 2.8 mT. The line width (Δ_{pp}) for both the parallel and perpendicular components was =7 mT (70 Gauss). Due to the Jahn-Teller effect, a regular octahedron can be tetragonally distorted with a d_{x2-y2} or d_{z2} ground state for elongated or compressed octahedra respectively. In the present case the trend of the g-value ($g_{||} > g_{\perp} > g_e$=2.0023) indicates that the unpaired electron occupies d_{x2-y2} orbital ($^2B_{1g}$ state) i.e. z-elongated case [74]. From the Hamiltonian parameters, the dipolar term (*P*) and the Fermi-contact term (*k*) are calculated using the following expressions [74].

$$P = 2\gamma_{Cu}\beta_e\beta_N(r^{-3}) \text{ and } k = (A_{iso})/P + \Delta g_{av} \qquad (10)$$

Where, γ_{Cu} is the magnetic moment of copper ion, β_e is Bohr magneton, β_N is the nuclear magneton and *r* is the distance from the central nucleus to the electron.

$$A_{iso} \text{ (in cm}^{-1}) = (A_{||} + 2\,A\perp)/3 \text{ and } \Delta g_{av} = g_{av} - g_e \text{ and } g_{av} = (g_{||} + 2g\perp)/3$$

The Fermi-contact term, *k* is a measure of the polarization produced by the uneven distribution of d-electron density on the inner core s-electron. In our case, the value of *P* and *k* were found to be 0.036 cm^{-1} and 0.301which is the general order.

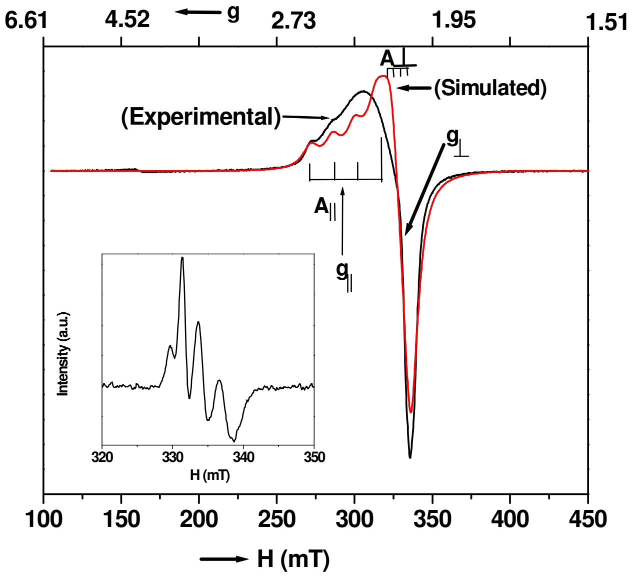

Figure 3.15. Room temperature experimental and simulated EPR spectra for the Cu-glass, the inset shows the spectrum in second derivative mode, the top axis shows the ‘g’ scale.

The absorption and the EPR data can be correlated to get an insight into the environment of Cu^{2+} ions in the glassy system. In an elongated octahedron case, the relationship in between the axial g values and the in plane sigma bonding parameter α^2, is given by the following expression as shown by Kivelson and Neiman [19].

$$\alpha^2 = [A_{//}/0.036] + (g_{//} - 2.0023) + 3/7\,(g_{\perp} - 2.0023) + 0.04 \qquad (11)$$

The value of α^2 was evaluated to be 0.9125. To evaluate the other bonding parameters orbital reduction factors were taken into account as follows [75].

$$K_{//} = (g_{//}-2.0023)\, E_{d-d} / 8\, \lambda_0 \text{ and } K_{\perp} = g_{\perp} - 2.0023)\, E_{d-d} / 2\, \lambda_0 \qquad (12)$$

Here λ_0 is the spin–orbit coupling constant for the free ion (~ 828 cm^{-1}), and $K_{||} = \alpha^2\beta^2$ and $K_{\perp} = \alpha^2\gamma^2$, where, β^2 is the in plane pi bonding parameter and γ^2 is the out of plane pi bonding parameter of the Cu(II) system. E_{d-d} is the electronic transition energy for the Cu^{2+} ion calculated from the absorption spectrum.

Significant information about the nature of bonding of copper (II) in glass matrix can be derived from the magnitude of $K_{||}$ and $K_{\perp}$. In case of a pure σ–bonding system, $K_{\perp} \sim K_{||}$, whereas $K_{||} < K_{\perp}$ implies considerable in-plane π-bonding, while for out of plane π-bonding $K_{||} > K_{\perp}$. In the present case, the values of $K_{||}$ and $K_{\perp}$ were evaluated to be 0.6970 and 0.5755, respectively, suggesting the presence of covalency in the system with out of plane π-bonding. Furthermore, the values of β^2 and γ^2 were calculated to be 0.7638 and 0.6307 respectively, which are much less than 1 (the value for 100% ionic bonding and decreasing with increasing covalency) and thereby confirming the covalent nature of the bonding in the glass.

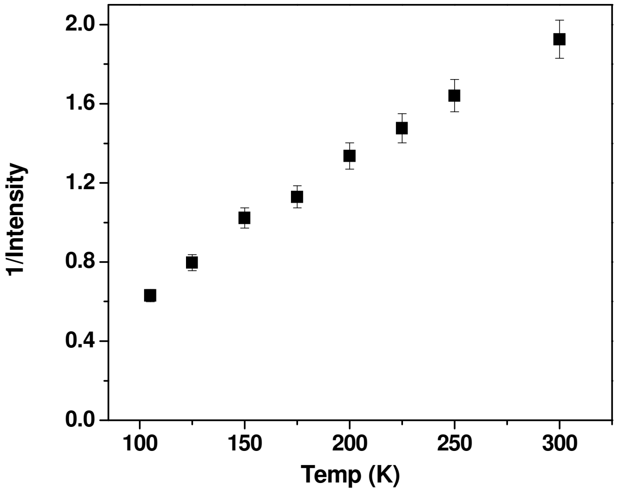

Figure 3.16. Temperature dependence of the EPR spectral intensity of Cu-glass

Figure 3.16 shows the temperature dependence of the EPR spectral intensity of Cu-glass in the range 100 – 300 K. The plot of reciprocal of EPR signal intensity versus temperature yields a straight line passing through origin. This indicates that the Cu^{2+} ions follow Curie –Weiss behaviour indicating paramagnetic nature of the sample.

3. Fe doped glass

For Fe in +3 state (d^5 = $^6S_{5/2}$ ground state), as there is no spin-orbit interaction, the *g* value is expected to lie very near to the free-ion value of 2.0023. However, *g* values much greater than 2.00 are often encountered; particularly an isotropic *g* value at 4.2 occurs which arises when the local symmetry around the paramagnetic ion is very low [76-78].

When Fe^{3+} ions are placed in a crystal field environment, the ^6S ground state splits into three Kramer's doublets i.e. $|\pm 1/2>$, $|\pm 3/2>$ and $|\pm 5/2>$. The resonance signal at $g \approx 4.2$ results from the middle Kramer's doublet $|\pm 3/2>$ [11].

The room temperature EPR spectrum for the Fe doped sodium barium borosilicate glass is shown in figure 3.17. The spectrum consists of two well-defined signals at g= 4.2 (sharp and highly intense) having line width $\Delta_{pp} \approx$ 10 mT (100 Gauss) and g = 2.0 (a broad signal) having line width of $\Delta_{pp} \approx$100 mT (1000 Gauss). Similar to Cr doped glass, in case of Fe-glass also, large values of 'g' can be best interpreted by the equation 9.

Here, *D* and *E* are the axial and rhombic structure parameter, $S = 5/2$ and E/D has a value in between 0 and 0.33.

As discussed earlier, this type of spectrum is typical of Fe^{3+} in lower symmetries. Particularly, the resonance at $g \approx 4.2$ is attributed to the isolated Fe^{3+} ions in tetrahedral or rhombic symmetry sites [21]. The $g \approx 2.0$ resonance may be attributed to either Fe^{3+} ions interacting by dipole–dipole interaction in sites of less distorted octahedral field [22].

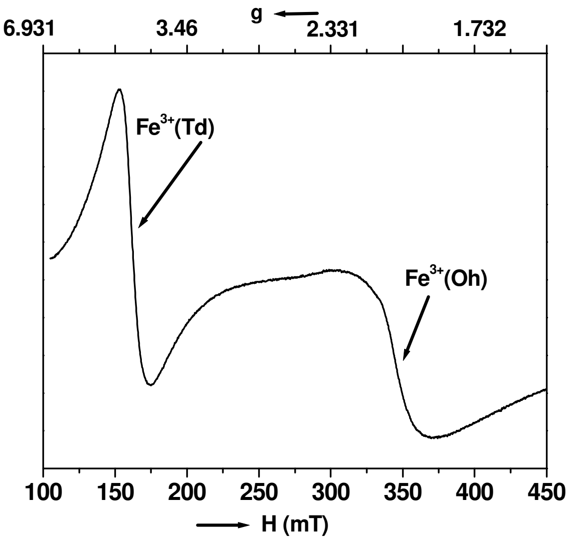

Figure 3.17. Room temperature EPR spectrum for the Fe-glass, the top X axis shows the 'g' scale

4. Mn doped glass

Figure 3.18 shows the EPR spectrum of 1 mol% Mn-glass recorded at room temperature. The spectrum shows a broad resonance consisting of six hyperfine lines with the centre at g = 2.00 along with shoulders around g= 3.3 and 4.3 along with the previously discussed g=4.3 line due to Fe^{3+}.

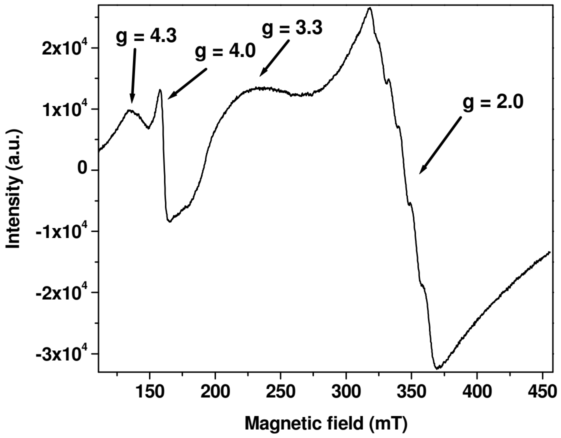

Figure 3.18 Room temperature EPR spectrum of 1 mol % Mn in borosilicate glass

The broad resonance with six hyperfine structures at g=2.0 with A = 8.5 mT was due to Mn^{2+} with I = 5/2. Similar types of signals were also observed in various glassy matrices like tetraborate, zinc and lead phosphate, lithium borosilicate glasses etc [14, 15, 17 and 24]. In case of Mn^{2+} (d^5, ^6S ground state) an axial distortion of octahedral symmetry will give rise to three Kramer's doublets |±5/2>, |±3/2> and |±1/2> whose degeneracy would be lifted on applying Zeeman field. In the case of most transition metal ions, the crystal field splitting is normally much larger than the Zeeman splitting and thus, the resonances observed are due to transitions within the Zeeman field split Kramer's doublets. The observed resonance signals at g = 3.3 and 4.3 are attributed to the rhombic surroundings of the Mn^{2+} ions arising from the transition in between the middle Kramer's doublets [79]. Whereas the well reported resonance at g = 2.0 is due to the lower Kramer's doublet transitions of Mn^{2+} ions in octahedral symmetry. The magnitude of the hyperfine splitting parameter (A) provides valuable information regarding the covalency between the central metal ion and the surrounding atoms. This is because; the strength of the hyperfine splitting is mainly dependent on the electronegativity of the neighboring atoms surrounding the central metal ion. A smaller value of the hyperfine splitting parameter would mean more covalency in the bonding [80]. In the present case the higher value of A (8.5 mT) suggests that the bonding in between the Mn^{2+} ions and O^{2-} ions is ionic in nature.

From the overall discussion it is clear that, all the metal ions are stabilized in lower symmetries (mostly tetrahedral or distorted octahedral) as network modifiers with partially covalent bonding with the surrounding oxygen ligands.

The results of other spectroscopic techniques such as Positron Annihilation Spectroscopy (PAS), Fourier Transform Infrared spectroscopy (FTIR) and micro Raman spectroscopy on the glass samples are not discussed in this chapter. These are left to be discussed in the respective chapters along with the changes after irradiation.

5. Eu and Gd doped glass

In the Eu doped glass no EPR signal, except the g=4.3 signal, was observed. This ruled out the formation of divalent Eu. Figure 3.19 shows the EPR spectrum of the Gd incorporated borosilicate glass matrix at room temperature.

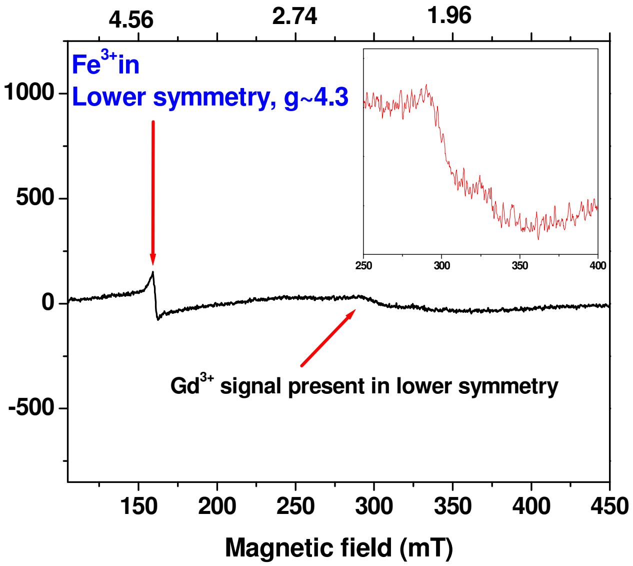

Figure 3.19. Room temperature EPR spectrum of the Gd doped glass. The inset shows the magnified signal due to Gd^{3+} ; the top axis shows the ‘g’ scale

The EPR spectrum of Gd^{3+}, an ‘*S*’ state ion, is well reported in literature where the line shapes are very much dependent on the ion concentration [81]. Usually in glass matrices, Gd^{3+} ions show the so called ‘U’ shaped spectrum with lines at ‘g’ = 6.0, 2.8 and often 2.0 [82]. The first two sets of lines are often attributed to diluted Gd^{3+} ions present in the matrix. Also, some papers report a broad asymmetric line at g=2.8 or 4.8 due to the presence of diluted Gd^{3+} spins in different sites [83]. But the line observed in most cases is the broad resonance (line width, Δ~ 600 mT) around g = 2. This broad resonance line is due to the magnetic clusters containing Gd^{3+} ions in the glasses.

In case of the present borosilicate glass also the g=2 line is attributed to spin concentrated or clustered Gd^{3+} ions. The observed broadening in this line comes from the magnetic dipole-dipole interactions between the Gd ions. Similar features for Gd ions were reported by Martino et al for a silica glass prepared via sol-gel process [84] and by Kliava et al for an alumina borosilicate glass [85]. As reported by them, the resonance of clustered Gd^{3+} ions is expected at close to free electron resonance values and indeed it occurs in our glass samples. The signal is generated due to the Gd^{3+} linked with each other by exchange interactions through the oxygen bridges present in the glass network. We did not observe any other signal due to the Gd ions in the glass matrix.

This suggest that there is a solubility limit for the Gd^{3+} ions in the glass and most of the Gd_2O_3 ions are remaining as magnetic clusters.

3.4. Conclusion

Alkali based barium borosilicate glasses having similar composition to the Trombay nuclear waste base glasses were incorporated with individual transition metal ions and rare earths. These were characterized by various spectroscopic techniques prior to any irradiation. Using these techniques, the oxidation states and coordination geometries of all the metal ions in the glass were determined. It was observed that Cr is stabilized in the glass matrix in two oxidation states namely, 3+ and 5+ in distorted octahedral geometries. The Racah parameter values were calculated from the absorption studies. Cu ions in the borosilicate glass got stabilized as Cu^{2+} where the lone electron resides in d_{x2-y2} orbital. It was found that the Cu^{2+} ions are interacting via a paramagnetic interaction through the oxygen linkage. From the correlation of the absorption and EPR data, bonding parameters were evaluated for the system. In case of Fe-glass it was found that iron gets stabilized in 3+ oxidation state both in tetrahedral and octahedral geometries. In case of Mn incorporated barium borosilicate glass, it was found out that, apart from the usual 2+ oxidation state, Mn gets stabilized in the matrix in the form MnO_4^- and MnO_4^{2-} as well. Both the RE ions were stabilized in their trivalent state in the glass matrix. In case of Eu-glass, the site distribution was found to be fairly large in glass and the asymmetric ratio was found to be quite high indicating the presence of Eu in highly asymmetric environment. In case of Gd glass also, it was observed that, the metal ion is stabilized in a highly asymmetric environment as Gd_2O_3 clusters. Spectral analysis of the Eu-glass was carried out to evaluate the J-O intensity parameters and various radiative properties. These properties suggested the existence of short range ordering in the glass with existence of higher degree of covalence in between the rare earth ion and oxygen ligands prior to irradiation. These findings will serve as input for the study of radiation induced changes in the borosilicate glass matrices.

References

1. R. C. Ewing, W. J. Weber, F. W. Clinard, Prog. Nucl. Energy 29 (1995) 63.
2. W.J.Weber, R.C.Ewing, C.A.Angell, G.W.Arnold, A.N.Cormack, J.M.Delaye, D.L.Griscom, L.W.Hobbs, A.Navrotsky, D.L.Price, A.M.Stoneham, M.C.Weinberg, J. Mater. Res. 12 (1997) 1946.
3. U. Natura, D. Ehrt, Glastech. Ber. Glass Sci. Technol. 72 (1999) 295.
4. J.D.Lee, Concise Inorganic Chemistry, Fifth Edition, Blackwell Science, 1999, USA.
5. F. The´venet, G. Panczer, P. Jollivet, B. Champagnon, J. Non-Cryst. Solid 351 (2005) 673.
6. H. Li, J.D. Vienna, D.E. Smith, P. Hrma and M. Gong, Ceram. Trans. 72 (1997) 399.
7. E.A.Davis and N.F.Mott, Philos. Mag. 22 (1970) 903.
8. Inorganic Chemistry, J. E. House, Academic Press, ISBN-0123567866, 9780123567864, (2008).
9. A.S.Rao, J.L.Rao, S.V.J.Lakshman, J. Phys. Chem. Solids 53 (1992) 1221
10. M.V.N.P.Rao, V.Ravikumar, L.S.Rao, P.V.Rao, M. S. Reddy, N. Veeraiah, J. Alloys Compd. 472 (2009) 489
11. A. Murali, J.L. Rao, G.L. Narendra, T. Harinathudu Opt. Mater. 7 (1997) 41.
12. T. Abrita, F.S. Barrros, J. Lumin. 40 (1988) 187
13. T. Bates, in: J.D. Mackenzie (Ed.), Modern Aspects of the Vitreous State 2, Butterworths, London, 242 (1962).
14. R.V.S.S.N. Ravikumar, K. Ikeda, A.V. Chandrasekhar, Y.P. Reddy, P.S. Rao, Jun Yamauchi, Journal of Phys. Chem. Solids 64 (2003) 2433

15. R.P.S. Chakradhar, G. Sivaramaiah, J.L. Rao, N.O. Gopal, Spectrochim. Acta Part A 62 (2005) 761
16. A. Murali, R.P. S. Chakradhar, J. L. Rao, Physica B 358 (2005)19.
17. R.P. S. Chakradhar, B. Yasoda, J.L. Rao, N.O. Gopal, J. Non-Cryst. Solids 353 (2007) 2355.
18. T.I. Maksimova , K. Hermanovich, J. Hanuza, and U. Happek,, Phys. Stat. Sol. (c) 2 (2005) 322
19. D. Kivelson and R. Neiman, J. Chem. Phys. 35 (1961) 149
20. N. Iwamoto, Y. Mokino, S. Kasahara, J. Non-Cryst. Solids 55 (1983) 113
21. J.L.Rao, A.Murali and E.D.Rao, J.Non Cryst Solids 202 (1996) 215
22. T. Castner Jr., G.S. Newell, W.C. Holton, C.P. Slichter, J. Chem. Phys. 32 (1960) 668
23. X. Feng, H. Li, L.L. Davis, L. Li, J.G. Darab, M.J. Schweiger, J.D. Vienna, B.C. Bunker, P.G. Allen, J.J. Bucher, I.M. Craig, N.M. Edelstein, D.K. Shuh, R.C. Ewing, L.M. Wang and E.R. Vance, Ceram. Trans. 93 (1999) 409.
24. A. S. Rao, B. Sreedhar, J. L. Rao and S.V.J. Lakshman, J. Non-Cryst. Solids 144 (1992) 169.
25. E. Malchukova, B. Boizot, D. Ghaleb and G. Petite, J. Non-Cryst. Solids 352 (2006) 297.
26. L. Li, H. Li, M. Quian and D.M. Strachan, J. Non-Cryst. Solids 283 (2001) 237.
27. X. Fan, M. Wang and G. Xiong, J. Mater. Sci. Lett. 12 (1993) 1552.
28. M.Graft, G.Boulon, G. Panczer, Y.Guyot, R.Reisfeld, S.Votyakov and G.Bulka, J.Lumin 87-89 (2000)1118.
29. N.Zotov, Y.Yanev and B.Piriou, Phys Chem Minerals 29 (2002) 291

30. Y.P.Naik, M.Mohapatra, N.D.Dahale, T.K.Seshagiri, V.Natarajan and S.V.Godbole, J. Lumin. 129 (2009) 1225.
31. X.Y.Chen and G.K.Liu, J. Solid State Chem. 178 (2005) 419.
32. G. H. Dieke, Spectra and Energy levels of rare earth ions in crystals, Editors- H. M. Crosswhite and H. Crosswhite, Interscience Publishers, John Wiley and Sons, New York, USA, 1968.
33. E.J. Bosze, G.A. Hirata, L.E. Shea-Rohwer and J. McKittrick, J. Lumin. 104 (2003) 47.
34. Yu-Chun Li, Yen-Hwei Chang, Yee-Shin Chang, Yi-Jing Lin and Chih-Hao Laing, J. Phys. Chem. C 111 (2007) 10682.
35. H. Song, D. Chen, W. Tang, Y. Peng, Displays 29 (2008) 41.
36. Y. C. Li, Y.S. Chang, Y.C. Lai, Y.J. Lin, C.H. Laing, Y.H. Chang, Mater. Sci. Engg. B 146 (2008) 225.
37. Y. C. Li, Y.H. Chang, Y.S. Chang, Y.J. Lin and C.H. Laing, J. Phys. Chem. C 111 (2007) 10682.
38. B. R. Judd, Phys.Rev. 127 (1962) 750.
39. G. S. Ofelt, J.Chem.Phys. 37 (1962) 511.
40. L. Sarakha, C. Forano and P. Boutinaud, Opt. Mater. 31 (2009) 562.
41. L. Liu and X. Chen, Nanotechnol. 18 (2007) 255704.
42. M. H. V. Werts, R. T. F. Jukes and J. W. Verhoeven, Phys. Chem. Chem. Phys. 4 (2002) 1542.
43. W. Shipeng, Z. Xiaoping, H. Shui, Z. Liqun and L. Li, J. Rare Earths, 26 (2008) 787.
44. O.L. Malta, M.A. Couto dos Santos, L.C. Thompson and N.K. Ito, J. Lumin. 69 (1996) 77.

45. E.S.Larsen and H.Berman, The Microscopic Determination of the Nonopaque Minerals, 2nd edition, U.S. Geol. Survey Bull. 848. Washington D.C. USA, 1934.
46. LANGE's Handbook of Chemistry, Editor- John A. Dean, Eleventh Edition, 10.258. McGraw-Hill Book Company, USA, 1973.
47. H. E. Heidepriem and D. Ehrt, J. Non-Cryst. Solids 208 (1996) 205.
48. M. J. Weber, T. E. Varitimos and B. H. Matsinger, Phys. Rev. B 8 (1973) 47.
49. W. T. Carnall, P. R. Fields and K. Rajnak, J. Chem. Phys. 49 (1968) 4412.
50. W. T. Carnall, P. R. Fields and B. G. Wybourne, J. Chem. Phys. 42 (1965) 3797.
51. S. Kuboniwa and T. Hoshina, J. Phys. Soc. Jpn. 32 (1972) 1059.
52. K. Gatterer, G. Pucker and H.P. Fritzer, Phys. Chem. Glasses 38 (1997) 293.
53. R. Reisfeld, E. Greenberg, R. N. Brown, M-G. Drexhage and C. K. Jorgensen, Chem. Phys. Lett. 95 (1983) 91.
54. G. Pucker, K. Gatterer, H.P. Fritzer, M. Bettinelli and M. Ferrari, Phys. Rev. B 53 (1996) 6225.
55. N. Ollier, G. Panczer, B. Champagnon, G. Boulon and P. Jollivet, J. Lumin. 94/95 (2001) 197.
56. C. Brecher, H. Samelson and A. Lempicki, J.Chem.Phys.42 (1965) 1081.
57. C.K. Jorgensen and R. Reisfeld, J. Less-Common Met. 93 (1983) 107.
58. R. Reisfeld, E. Zigansky and M. Gaft, Mol. Phys. 102 (2004) 1319.
59. K. Binnemans, K. Van Herck and C. Gorller-Walrand, Chem. Phys. Lett. 266 (1997) 297.
60. K. Annapurna, M. Das, P. Kundu, R.N. Dwivedi and S. Buddhudu, J. Mol. Struct. 741 (2005) 53.
61. S.Hazarika and S.Rai, Opt. Mater. 27 (2004) 173.

62. H. Lin, D. Yang, G. Liu, T. Ma, B. Zhai, Q. An, J. Yu, X. Wang, X. Liu and E. Y.-B. Pun, J. Lumin. 113 (2005) 121.
63. M. Bettinelli, A. Speghini, M. Ferrari and M. Montagna, J. Non-Cryst. Solids 201 (1996) 211.
64. D. U. Maheswari, J. S. Kumar, L.R. Moorthy, K. Jang and M. Jayasimhdri, Physica B 403 (2008) 1690.
65. P. Abdul Azeem, M. Kalidasan, K. Rama Gopal and R.R. Reddy, J. Alloys Compd. 474 (2009) 536.
66. Heike Ebendorff-Heidepriem and Doris Ehrt, J. Non-Cryst. Solids 208 (1996) 205.
67. R. J. Landry, J. T. Fournier, and C. G. Young, J. Chem. Phys. 46 (1967) 1285.
68. I. Ardelean, Gh. Iionca, M. Peteanu, E. Barbos, and E. Indrea, J. Mater. Sci. 17 (1982) 1988.
69. R.P.S.Chakradhar, J.L.Rao, G.Sivamaiah and N.O.Gopal, Phys. Stat. Sol. B 242 (2005) 2919
70. Shigeki Morimoto, Sasithorn Khonthon, Yasutake Ohishi, J. Non-Cryst. Solid 354 (2008) 3343.
71. J.Wong and C.A.Angell Appl Spectrosc. Rev. 4 (1971) 155.
72. N.S.Garif'yanov Sov. Phys. Solid State 4 (1963)1795.
73. R. Bruckner, N.Sammet and H. Sockhorst J. Non-Cryst. Solids 40 (1980) 273.
74. S. P. Devi, S. M. Devi, N. S. Devi, R.K.H.Singh, M. Mohapatra, R.M. Kadam, Inorg. Chem. Comm. 11 (2008) 1441.
75. O. I. Singh, M. Damayanti, N. R. Singh, R.K. H. Singh, M. Mohapatra, R.M. Kadam, Polyhedron 24 (2005) 909.

76. T. Castner Jr., G.S. Newell, W.C. Holton, C.P. Slichter, J. Chem. Phys. 32 (1960) 668

77. J.M. Yanezlimon, J.F. Perezrobles, J. Gonzalez-hernandez, Y. V. Vorobiev, J.A. Romango, F.C.G. Gandra, E.C. Dasilva, J. Sol-Gel Sci. Technol. 18 (2000) 207.

78. I. Ardelean, M. Peteanu, S. Filip, V. Simon, G. Gyorffy, Solid State Commun. 102(1997) 341.

79. R. S. Drago; Physical Methods in Inorganic Chemistry, Chapter 10, Electron Paramagnetic Resonance Spectroscopy pp 328; Affiliated East West Press Pvt.Ltd.

80. J.A.Weil, J.R.Bolton, J.E.Wertz, Electron Paramagnetic Resonance Elementary Theory and Practical Applications, New York: Wiley (1994)

81. Alex I. Smirnov and S. Sen, J. Chem. Phys. 115 (2001) 7650

82. S. Simon, I.Ardelean, S.Filip, I.Bratu, I.Cosma, Sol. State Comm. 116 (2000) 83.

83. P. Colomban, J. Non-Cryst. Solids 323 (2003) 180

84. D.DiMartino, N.Chiodini, M.Fasoli, F.Moretti, A.Vedda, A.Baraldi, E. Buffagni, R.Capelletti, M.Mazzera, M.Nikl, G.Angella, C.B.Azzoni, J. Non-Cryst. Solids 354 (2008) 3817

85. J.Kliava, I.S.Edelman, A.M.Potseluyko, E.A.Petrakovskaja, R.Berger, I.Bruckental, Y. Yeshurun, A.V.Malakhovskii and T.V.Zarubina J. Phys.: Condens. Matter 15 (2003) 6671

Chapter-IV

Spectroscopic investigations of the gamma irradiated borosilicate waste glasses

4.1. Introduction

As discussed earlier, at BARC Trombay, India, the high level radioactive waste (HLW) generated after reprocessing of the spent nuclear fuel is being routine fixed in borosilicate based glass matrices [1]. The fission/activation products and the actinides present in the HLW undergo radioactive decay accompanied by emission of ionizing radiations. These radiations may interact with the constituents of the glass matrix leading to changes in the long term physical and chemical properties of the material [2]. The impingement of the ionizing radiation on the glass may lead to the changes in the oxidation states and coordination environment of the metal ions present in the glass [3]. The formation of defects in the glass structure has also been related to the interaction of the ionizing radiation in the glass matrix [4]. At higher radiation doses, the possibility of phase separation in the glass also exists [5].

The ionizing radiations of interest are α, β and γ. However, for the first hundred years, the β activity dominates the total radioactivity. Nevertheless, in order to fully understand the radiation damage in the glass matrix, one can not ignore the effect of gamma radiation. The gamma photons, which are mostly generated during the beta decay of the fission products, primarily interact with the glass matrix via photoelectric effect and Compton scattering. Absorption of these gamma ray photons in the glass matrix results in the formation of electron-hole pairs which lead to the formation of metastable defect centers [6]. Moreover, since the gamma rays have higher penetrating power, their effect occurs throughout the glass waste form.

Several literature reports are available on the subject of gamma radiation induced changes in borosilicate glass matrices [7-10]. A comprehensive review has been published by Weber et al. that summarize the work carried out on the aluminoborosilicate glasses especially designed for the vitrification of nuclear waste in USA [11]. Recently, McGann et al. have reported an exhaustive study on the effects of gamma radiation on variety of model borosilicate based nuclear waste glasses containing iron [12]. Most of the reports suggest that, upon irradiation, the glasses undergo changes in their structure leading to formation of defect centers, voids or disorders accompanied by volume changes, phase separation or gas accumulation.

In the previous chapter characterization of the glass matrix before irradiation was discussed in detail. This chapter discusses the gamma radiation induced changes in these glass matrices as studied by spectroscopic techniques by employing suitable probe ions i.e. Eu^{3+} and Fe^{3+}. These ions are excellent structural probes for studying the local environment. Eu in its trivalent state is considered as a possible surrogate for the trivalent minor actinides. Moreover, it can mimic the trivalent plutonium Pu(III) in glassy matrices, which was found to be more soluble in borosilicate glasses than the usual Pu(IV). On the other hand, the element iron is expected to present in the Trombay waste glass in substantial amounts. It is expected to come in the waste stream from the ferrous sulfamate added during the PUREX process as a reducing agent. Moreover, it can also come in the HLW as a process pick-up and corrosion products (total salt content in the stored Trombay HLW- 317gm/L) [1].

4.2. Experimental

The details of the glass sample preparation are given in chapter-3. The base glass and the doped glass (with transition metal and rare earth) were subjected to gamma irradiation with varying irradiation time. The irradiations were done in two ^{60}Co gamma chambers with dose rates of 1 kGy/hr and 8kGy/hr as per the requirement. All the samples were irradiated with cumulative doses of 2, 50, 250 and 900 kGy. The irradiated glass samples were characterized by XRD, PL, EPR, FTIR and PAS techniques whose details are presented earlier. Photoluminescence (PL) experiments were carried out on the Edinburgh Time Resolved Fluorescence Spectrometer unit. For EPR experiments the Bruker

ESP 300 spectrometer was used. The 'g' values for the respective species were calibrated relative to a 2,2 diphenyl-1 picryl hydrazil (DPPH) reference standard having g = 2.0036. The computer simulation program 'SIMFONIA' from Bruker, which is based on perturbation theory, was used to simulate the EPR spectra and compared with the experimentally obtained spectra. For positron annihilation spectroscopic (PAS) measurements, ^{22}Na positron source in the form of NaCl folded in kapton foil was sandwiched between the two identical pieces of borosilicate glass samples. Positron annihilation lifetime measurements were carried out using plastic scintillation detectors coupled to fast-fast coincidence system with a time resolution of 235 ps as measured with ^{60}Co source in ^{22}Na energy window setting. Data analysis was carried out using PATFIT program [13].

IR absorption spectra of the glass samples before and after irradiation were recorded at room temperature in the 400-4000 cm^{-1} range using a Bruker Vertex 80V Fourier transform infrared (FTIR) spectrometer by the KBr pellet technique (2 % sample in KBr powder). The spectra were obtained at a resolution of 4 cm^{-1} using a globar source, KBr beam splitter and DTGS detector. The spectrum of each sample was normalized with the spectrum of the blank KBr pellet.

4.3. Results and Discussion

The XRD patterns of the irradiated base as well as the doped glass samples were similar to the respective unirradiated samples. This indicated the absence of any crystalline phase in the irradiated samples. After gamma irradiation, the glass samples became colored due to the formation of color/defect centers. Thus normal UV-Vis absorption studies could not be performed on these samples. The results of the other spectroscopic techniques on the irradiated glasses are discussed below.

A. Studies on the base glass

1. PL investigations

Figure 4.1 shows the PL spectra of the gamma irradiated base glass samples with 171 nm excitation at varying dose. The spectrum is characterized by the presence of weak but broad peaks at 229, 257, 507 and 687 nm and a shoulder at 457 nm. The PL peak intensities increased with increase in the radiation dose. As discussed earlier in chapter-3 (Section 3.3 D; Page-11), the unirradiated base glass did not show any peaks in the PL spectrum.

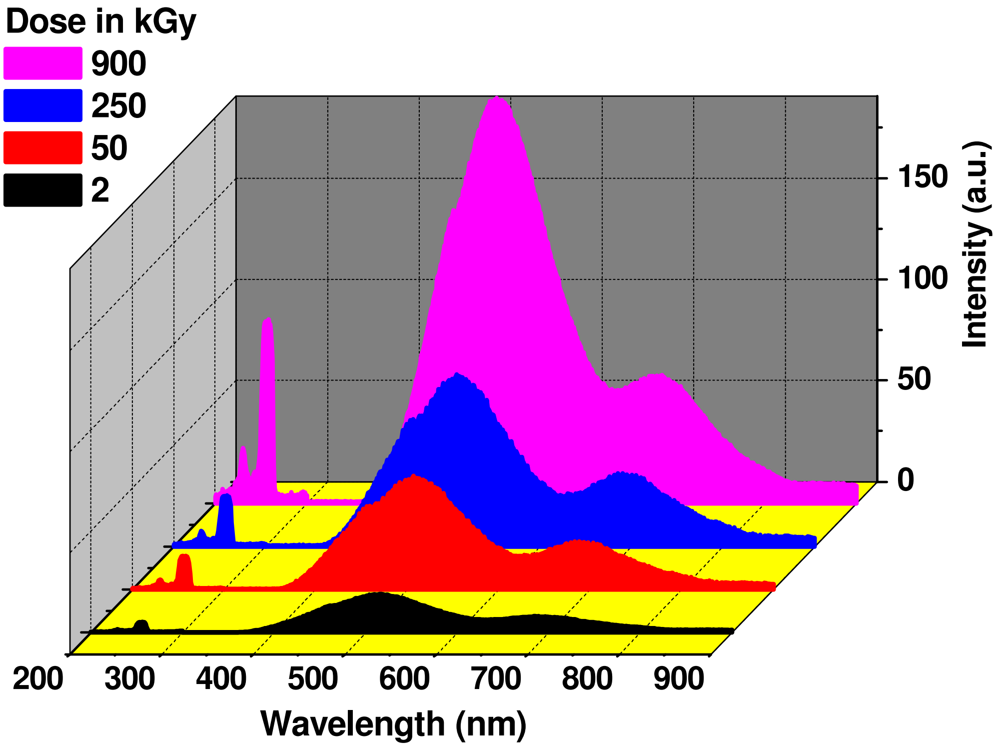

Figure 4.1 PL spectrum of the gamma irradiated borosilicate base glass with varying dose

The radiation induced luminescent centers in borosilicate glasses have been reported in literature by many authors. Blasse has a given a comprehensive review on the luminescence centers in various types of glassy matrices and other related solids [14]. Kristianpoller in his classical work has studied the photoluminescence centers in unirradiated quartz under UV excitation [15]. Malchukova et al have investigated the gamma irradiated borosilicate glasses doped with a rare earth ion, namely, Sm^{3+} [16]. Nuccio et al have carried out PL studies on gamma and electron beam irradiated silica glasses and showed the formation of various types of point defects [17]. Based on the literature, the five peaks observed were assigned to various defect centers as follows. The peaks at 687 and 507 nm were assigned to the non-bridging-oxygen hole centers (NBOHC) as shown by Cannas et al [18]. The two emission bands at 457 nm and 257 nm were attributed to the well known oxygen deficiency centers

(ODC) as reported by Nuccio et al and Cannas et al [17, 18]. The emission band at 229 nm was attributed to an E' centre such as ≡Si˙. The generation of NBOHC and E' centers were attributed to the bond cleavage occurring at regular Si–O sites due to the impinging electron beam on the glass. The different bands and their assignments are presented in table 4.1 along with their literature references.

Wavelength (nm)	Assignment (defect centre)	Ref.
229	E' centre	14, 15, 17
257	ODC	14, 17
457	ODC	17
507	NBOHC	16, 18
687	NBOHC	16, 18

Table 4.1 PL band positions of the irradiated glasses and their assignments along with the literature references.

2. EPR investigations

Figure 4.2 shows the room temperature X band EPR spectrum of the gamma irradiated borosilicate base glasses. The spectrum is characterized by two sets of signals, one at g ~2.0 and the other at g ~4.3. In the unirradiated glass sample except the sharp and intense signal at g ca 4.3 due to trivalent Fe in lower symmetry, no other signal was observed as already discussed in chapter-3. Thus the line at g ca 2.0 was only attributed to the various paramagnetic centers generated due to gamma irradiation. This 'g = 2.0' line was very complex in nature and consisted of superposition of several contributions from different paramagnetic centers induced by external irradiation. The free radicals formed during the radiolysis were identified on the basis of their g factors and hyperfine coupling constants (A). The deconvoluted spectra were used for obtaining the spin Hamiltonian parameters of the paramagnetic defects.

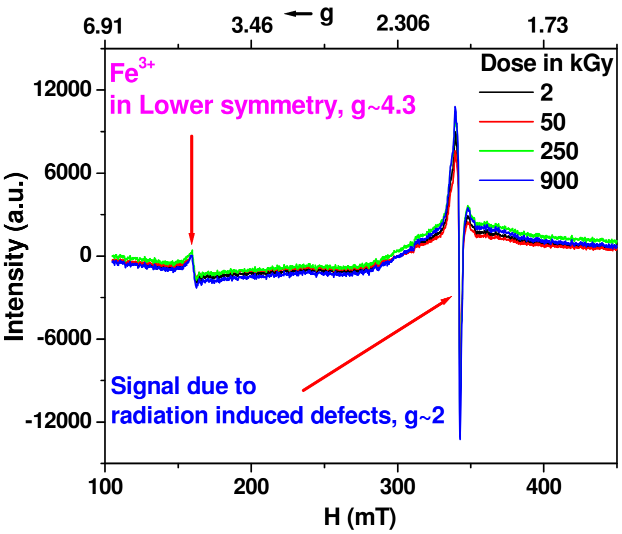

Figure 4.2. EPR spectra of the gamma irradiated glasses at varying gamma doses; the upper scale shows the spectrum in 'g' scale

According to the reported literature, in irradiated borosilicate glasses, the main radical expected to be formed is boron oxygen hole centre (BOHC) [19, 20]. Figure 4.3 shows the EPR signal at g~2.0, generated due to the defect centres in the 900 kGy gamma irradiated glass samples in a smaller scale.

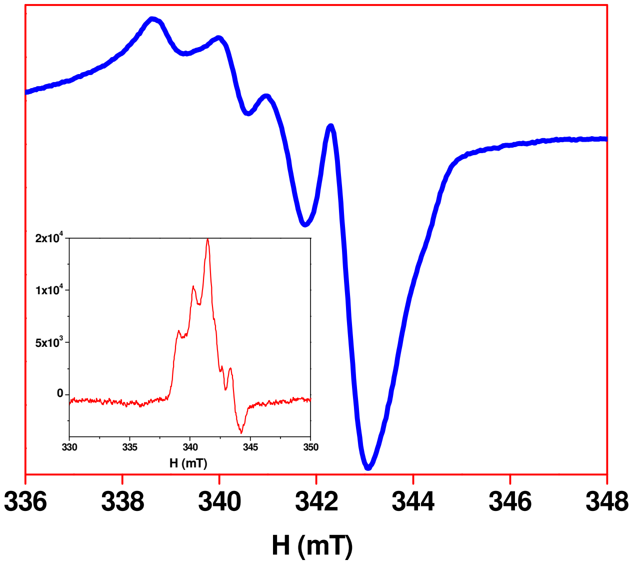

Figure 4.3. EPR signal at g = 2.00 in 900 kGy irradiated samples; the inset shows this in double derivative mode

Major part of the EPR signal showed a well resolved quartet hyperfine structure that was identified as BOHC. The observed hyperfine structure in present case was attributed to the interaction of unpaired electron of the radical with the most abundant isotope of boron, ^{11}B (I=3/2, natural abundance 80.2%). The hyperfine structure due to ^{10}B nucleus (I=3; isotopic abundance 19.8%) is unresolved and adds to the line width of EPR signal ($\Delta H = 0.7$ mT). In close proximity to the BOHC signal, an isotropic signal with g = 2.001 and line width 0.25 mT was observed. This signal is clearly seen when the spectrum is recorded in second derivative mode (shown as figure 4.3 inset). This was attributed to the well known electron trap (ET) centre which can be due to an electron trapped on silicon atom ($\equiv Si^{\cdot}$) [21]. The various EPR parameters for the radicals are given in table-4.2.

EPR Spin Counting Technique

EPR spectroscopy presents a quantitative technique to calculate the number of spins (concentration) participating in a resonance. This can be achieved by comparing the area under the absorption curve with that of a standard compound of known concentration. As shown by Weil et al. the following equation can be used to calculate the number of species under resonance which takes care of the experimental parameters of both sample and standard [22].

$$N = \frac{(A_x)(Scan_x)^2 G_{std}(B_m)_{std}(g_{std})^2[S(S+1)]_{std}(P_{std})^{1/2}}{(A_{std})(Scan_{std})^2 G_x(B_m)_x(g_x)^2[S(S+1)]_x(P_x)^{1/2}}[std] \tag{4.1}$$

Where *A* is the area under the absorption curve which can be obtained by double integrating the first derivative EPR absorption curve. '*Scan*' is the magnetic field corresponding to unit length. *G* is the gain, B_m the modulation field width and '*g*' the g-factor. '*S'* is the spin of the probe atom or ion in its ground state and *P* is the applied microwave power. The subscripts '*x*' and '*std*' represent the corresponding quantities for defect centre signal in the glass samples and the standard/reference. In this case, we have used $CuSO_4.5H_2O$ as the standard. The quantity [*std*] represents the number of Cu^{2+} spins present in a known weight of standard that was used in the study. Putting the respective values in equation 4.1, the defect concentration in the 900 kGy gamma irradiated sample was calculated to be 2.8×10^{17} spins / 100 mg.

Paramagnetic species	g_1	g_2	g_3	A_1 (mT)	A_2 (mT)	A_3 (mT)	Δ_1 (mT)	Δ_2 (mT)	Δ_3 (mT)	L/G
BOHC	2.0350	2.0105	2.0020	0.85	1.35	1.35	1.5	0.5	0.5	0.5
E'	2.0014	2.0015	2.09	-	-	-	0.25	0.25	0.25	0.5

Table 4.2: Spin-Hamiltonian parameters for the radicals formed in the gamma irradiated glass. Here 'g_i' (i =1,2 and 3) are the individual 'g' values, 'A_i' are the hyperfine coupling constants, Δ_i are the line widths of the EPR spectrum and L/G is the relative Lorentzian to Gaussian ratio used to simulate the EPR spectrum.

Taking the average molecular weight of the borosilicate glass into consideration, this spin concentration equals to ~ 350 ppm in a 100 mg sample. This suggests that at 900 kGy, the defects centers are very small in number to create any significant damage to the glass.

3. IR investigations

Figure 4.4 shows the baseline corrected infrared absorption spectra for the glass after gamma irradiation. All the spectral features of the IR bands are typical of structural silicate and borate chains. The observed bands can be attributed to specific groups or vibrations given in the literature [23-26]. The main band observed here ranging from 800 to 1200 cm^{-1} corresponds to the combined stretching vibrations of Si-O-Si and B-O-B tetrahedral networks [27]. The weaker but significantly clear band at 700-800 cm^{-1} is attributed to the bending vibrations of bridging oxygen among the trigonal BO_3 groups [28, 29]. The broad band with medium intensity centered at ~ 500 cm^{-1} consists of overlapping vibrations of Si-O-Si bending modes and alkali cations at their network sites. The bands occurring in the region 1200 to 1600 cm^{-1} region are attributed to stretching vibrations of BO_3 units with non-bridging oxygens (NBOs) [30]. The broad band extending from 3200 to 3500 cm^{-1} is attributed to molecular water [31].

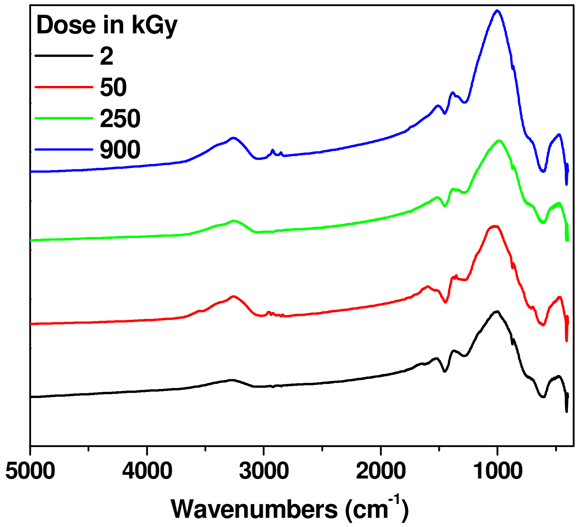

Figure 4.4. FTIR data in full scale for the gamma irradiated base glass samples

The IR active vibrations of the borate and silicate units usually occur in the wave number region higher than 550 cm^{-1}; therefore we focused the IR region 600-1800 cm^{-1}. As it is already discussed, the borosilicate glass network can be described as a structure where the network nodes are occupied by four fold silicon or boron and three fold boron atoms. The Si-O stretching frequency in SiO_4 is known to occur at about 1060 cm^{-1} where as for the B-O unit in BO_4, it falls in the region 1000 cm^{-1}.

Upon irradiation, the main peak position, due to the silicate and borate network, shifts from ~1100 cm^{-1} to ~1000 cm^{-1} and the band get broadened indicating that, there is a significant change in the network. This is mainly because of the breaking of Si-O bonds leading to the formation of super structural units with NBOs. With increase in the radiation dose, the band at ~780 cm^{-1} became broader and shifted to lower wave number suggesting the changes taking place in the glass structural framework. The intensity of the bands appearing in the region 1300-1700 cm^{-1} was enhanced after irradiation indicating the increase in the formation of NBOs after irradiation.

4. PAS investigations

Positron annihilation spectroscopy has been widely used as an important non destructive tool to study the defects in metals and semiconductors as well to study the free volume related microstructure in different crystalline and amorphous solid molecular substances. Because of their light mass and positive charge, positrons are sensitively trapped at vacancy-type defects and give us very useful information about their size, concentration and electronic structures. Several groups have studied the positron annihilation behavior in silica and other glassy materials [32-34]. A borosilicate based glassy system can be visualized as a continuous random network of tetrahedra of the glass network forming elements e.g. Si and B, joined at the corners such that each silicon is bonded to four oxygen atoms and each oxygen bridges between two silicon or boron atoms (known as the bridging oxygen). The bond angle of a regular Si-O-Si bond in amorphous borosilicate glass varies largely from 109 ° to 180° [35, 36] and hence the resulting structure has large open spaces or voids. When positron is introduced into such an amorphous material with large void spaces, a fraction of thermalized positron may form positronium (a bound-state of an electron and positron) and localizes in the void space. Positronium (Ps) is formed either as spin-singlet *para* positronium (p-Ps) or spin triplet *ortho* positronium (o-Ps) with a ratio 1:3. In vacuum, p-Ps decays into two photons with intrinsic lifetime 0.125 ns and o-Ps decays into three photons with a large intrinsic lifetime 140 ns. However, in the presence of matter, o-Ps can seek out electron with opposite spin from the surface of the void and annihilates through two-photon mode known as *pick-off* annihilation with lifetime range ~1-10 ns. Thus, the o-Ps *pick-off* annihilation rate (or lifetime) and their intensity can give valuable information about the void size and their number density. Positron annihilation lifetime results for the gamma irradiated borosilicate glass samples are shown in Fig 4.5. Here the graph shows the variation in the *pick-off* life time in nano sec with dose. It is clear from the figure that o-Ps *pick-off* lifetime (τ_p) in irradiated sample is higher than that in unirradiated sample and it increases with the radiation dose. The increase in o-Ps lifetime is related to the increase in free volume size inside the borosilicate glass sample due to the effect of gamma irradiation. The free volume size of the glass samples (R) are calculated from *pick-off* lifetime (τ_p) using the Tao-Eldrup equation shown in equation 4.2 [37, 38] as follows.

$$\tau_p = \frac{1}{2}\left(1 - \frac{R}{R+\Delta R} + \frac{1}{2\pi}\sin\frac{2\pi R}{R+\Delta R}\right)^{-1} \tag{4.2}$$

Here τ_p is measured in ns and R (radius of the spherical free/defect volume) is in Å. The ΔR (1.66 Å) is the electron layer thickness inside the wall of the spherical free volume.

Since IR and PAS are spectroscopic technique for the bulk which will hardly change on doping, these were not used to study the doped glasses.

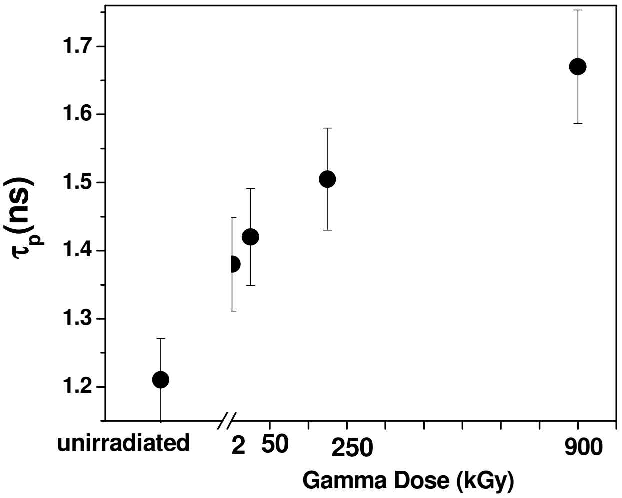

Figure 4.5. Variation of *pick-off* lifetime (τ_p) with gamma dose

B. Studies on the Eu doped glass

1. PL investigations

Figure 4.6 shows the emission spectra of the Eu doped glass samples after γ irradiation. The assignments to the various peak positions observed in the spectrum have been done in chapter-3. Upon irradiation, no significant changes in the line position or intensity of the peaks were observable. However, one noteworthy observation here was the change in the asymmetric ratio (‘A’) for the Eu^{3+} ion. This is defined as the ratio of the intensity of the $^5D_0 \rightarrow {}^7F_2$ and the $^5D_0 \rightarrow {}^7F_1$ transitions (I_{611}/I_{591}). The electric dipole transition ($^5D_0 \rightarrow {}^7F_2$) is hypersensitive in nature than the magnetic dipole transition ($^5D_0 \rightarrow {}^7F_1$). Thus ‘A’ value gives the information regarding the symmetry and the covalence of the rare earth ion site. Its value increases with increasing covalence of the ligands or decreasing site symmetry. The ‘A’ values obtained for the borosilicate glasses obtained before and after irradiation are presented in table-4.3. It can be seen that upon irradiation, the values increased indicating a decrease in the site symmetry of the rare earth ion in the glass after irradiation [39].

The local site symmetry of the RE ion can also be characterized by the full width at half-maximum (FWHM) data of the $^5D_0 \rightarrow ^7F_0$ emission band. This transition becomes allowed only in cases where the site symmetry of the metal ion is C_{nv} or lower. A lower value of the FWHM infers a smaller site distribution of the RE ions. The values for the FWHM as a function of radiation dose are also listed in table-4.3. It is observed that, on irradiation, this value increases indicating that, on irradiation, the site distribution for the RE ion becomes broader along with a reduction in the symmetry.

From the emission data, the site symmetry of the metal ion can be obtained as shown in chapter-3 (Section 3.3, D.6; page-18). In the present case, it was observed that, the metal ion was present in a distorted geometry (close to C_2) in the glass before irradiation. J. de Bonfils et al. have calculated the changes in the ligand field parameter (B_2) of Eu^{3+} ion by fluorescence line narrowing spectroscopy as a function of radiation damage by heavy ion irradiation [40].

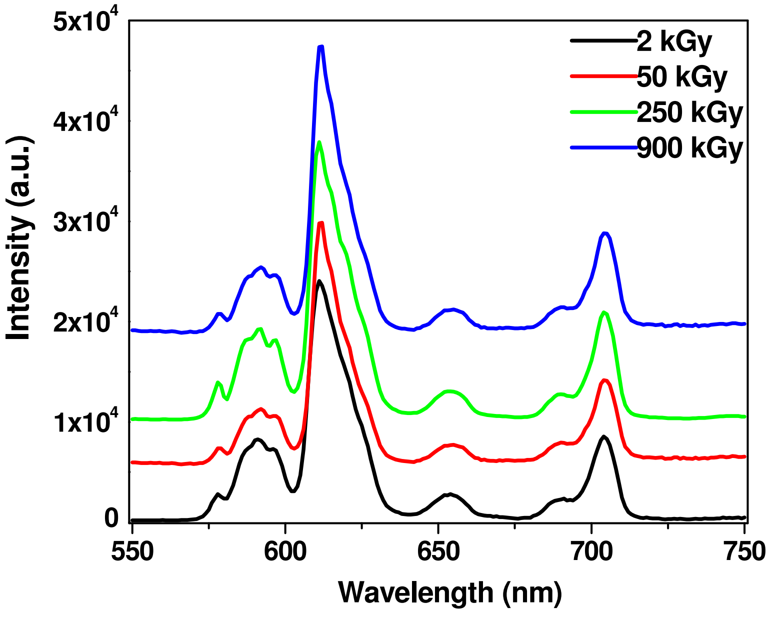

Figure 4.6 PL emission spectra of the borosilicate glasses irradiated with varying gamma dose

Sample	Unirradiated	2 kGy irradiated	50 kGy irradiated	250 kGy irradiated	900 kGy irradiated
Asymmetric ratio ($A = I_{611}/I_{591}$)	2.91	2.95	2.96	2.99	3.05
FWHM data of the $^5D_0 \rightarrow {}^7F_0$ emission band (cm^{-1})	120	122	140	152	168

Table 4.3: Comparison of the Asymmetric ratios and FWHM of the $^5D_0 \rightarrow {}^7F_0$ transition of Eu^{3+} species in glasses before and after gamma irradiation

They observed a decrease in site symmetry of the RE ion with increase in site distribution as a function of radiation dose. Because of instrumental limitation, we could not evaluate the changes in the ligand filed parameters as a function of dose. However, based on the trends in the 'A' and FWHM of the $^5D_0 \rightarrow {}^7F_0$ transition, it is believed that, with radiation dose, a reduction in the site symmetry with broader site distribution is taking place for the RE ion which is in accordance with the literature reports .

Most of the literature reports on irradiated borosilicate glasses with europium have reported the formation of Eu^{2+} or $(Eu^{3+})^-$ species in the glasses on irradiation [41-43].

However, in case of the present alkali barium borosilicate glasses, there was no PL signature of divalent Eu in the glass samples after irradiation. The formation of the divalent species in these glasses is attributed to the radiation induced reduction of the trivalent europium via electron trapping. But in the present barium based glass we did not find the presence of the divalent RE ion before or after gamma irradiation. This can be explained on the basis of the compositional difference existing among the different glasses. In the Trombay waste glass that we have studied, a significant amount of 'Ba' is present along with Fe^{3+}. The trivalent iron is known to act as electron trapping species when present in glasses. Olivier et al. have shown that, the presence of Fe^{3+} reduces the formation of defect centres in electron beam irradiated alkali borosilicate glasses [44]. It was observed by them that the transition metal ion itself traps the electrons and gets reduced to Fe^{2+}. Thus in our case also, it is believed that, the iron present in the glass traps electron restricting the radiation induced reduction of the rare-earth ion.

Before irradiation, the glass samples had shown a single exponential decay curve of 2.7 ms as discussed in chapter-3 (figure 3.13, page-15). However, all the samples after gamma irradiation showed bi-exponential decay curves with two life time values, one short lived and one long lived. This is shown in figures 4.7. Majority of the literatures available report bi-exponential decay times for Eu^{3+} in glassy matrices.

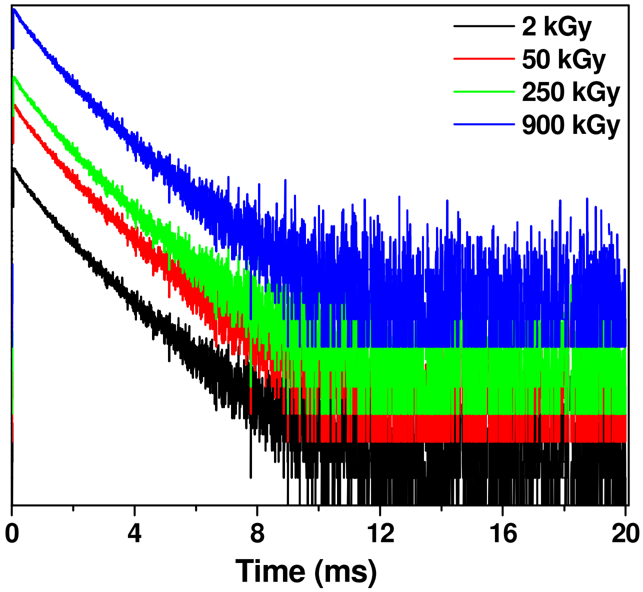

Figure 4.7 PL decay time spectra of the borosilicate glasses doped with Eu^{3+} as a function of gamma dose

Sample	Unirradiated	2 kGy	50kGy	250kGy	900kGy
τ_1(ms)	2.7±0.1 (100)	2.78±0.1 (90)	2.81±0.1 (85)	2.79±0.1 (80)	2.80 ±0.1 (75)
τ_2(ms)	---	1.3±0.1 (10)	1.3±0.1 (15)	1.3±0.1 (20)	1.3±0.1 (25)

Table 4.4: Comparison of the decay time values of the Eu^{3+} ion in borosilicate glass before and after irradiation. The figures in bracket indicate the relative percentages

One interesting observation here is that the relative percentage of the short lived component kept on increasing with radiation dose. This suggests that on irradiation, the RE ion is going preferentially to a site with lower symmetry. The decay time values of the glass samples as a function of the gamma dose are represented in table -4.4. A detailed time resolved emission spectrometric study (TRES) was carried out by giving suitable delay times in order to identify the two species responsible for the bi-exponential life times (shown in figure 4.7). However, the two emission spectra obtained from the TRES experiments were similar in nature and could not be differentiated.

Figure 4.8 shows the excitation spectrum of the irradiated glasses recorded with λ_{em} = 611 nm and normalized with respect to the f-f transition at 320 nm ($^7F_0 \rightarrow ^5H_3$). It can be observed from the figure that, the intensity of the charge transfer (CT) band at ~225 nm increases with the radiation dose. However, the intensity of the 320 nm band (f-f transition, $^7F_0$-$^5H_3$) remains same because of normalization. This indicates energy transfer from the defect centers, formed in the glass on gamma irradiation, to the rare earth ion. Due to this energy transfer the signatures of the defect centers could not be seen in the PL data which was otherwise observed in the base glass.

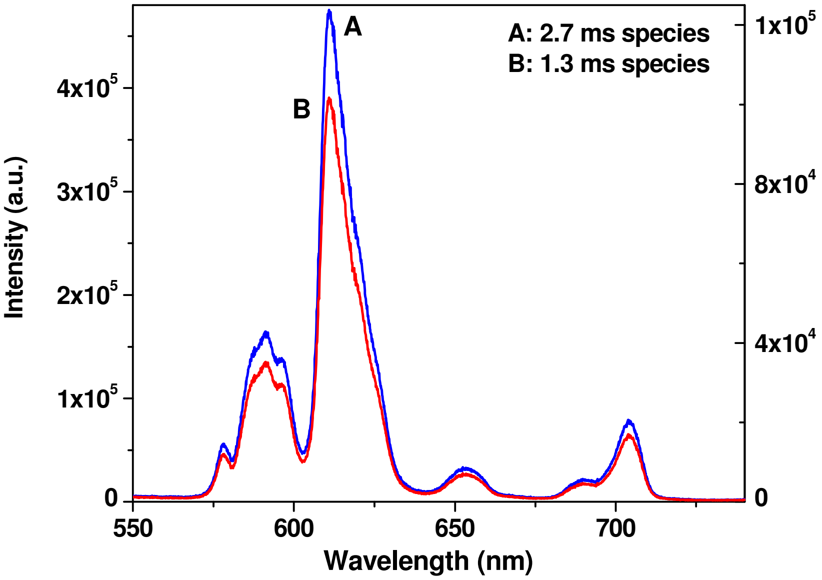

Figure 4.7: TRES spectrum of the irradiated Eu-glass sample showing the two species responsible for the two decay time values.

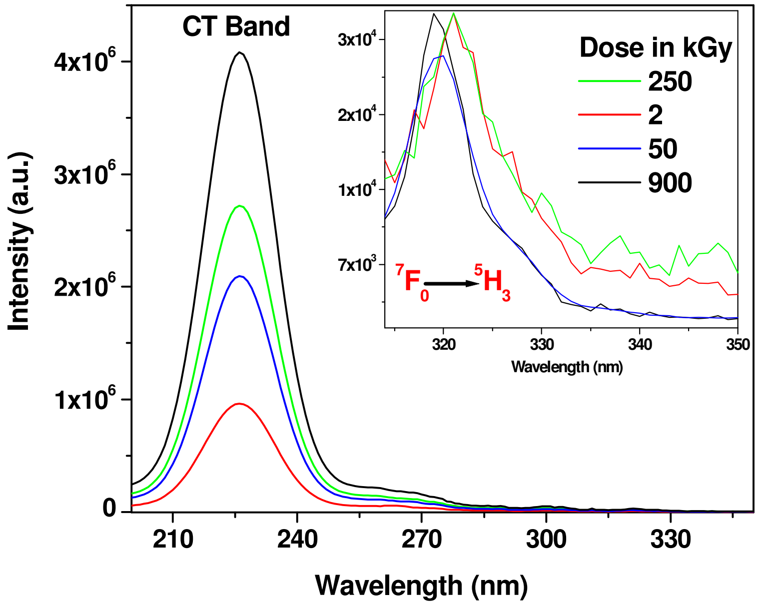

Figure 4.8. Excitation spectra of the irradiated glasses, the inset shows the peak at 320 nm corresponding to f-f transition.

2. Judd-Ofelt analysis of the emission spectra

The details of J-O analysis procedure have been discussed in chapter-3 (Page-14). Similar procedures were adopted to evaluate the parameters in the irradiated samples. A comparison of the JO parameters for the un-irradiated and gamma irradiated samples is shown in table-4.5. It is clear from the table that, there is no significant change in the values Ω_2 after irradiation. However, a significant change is observed in the value of Ω_4.

	Unirradiated		2 kGy		50 kGy		250 kGy		900 kGy	
Ω_J in 10^{-20} cm^2	Ω_2	Ω_4	Ω_2	Ω_4	Ω_2	Ω_4	Ω_2	Ω_4	Ω_2	Ω_4
Long lived species	6.57	1.81	6.55	1.83	6.58	1.85	6.56	1.87	6.57	1.90
Short lived species	-	-	6.59	2.2	6.56	2.38	6.58	2.45	6.58	2.58

Table 4.5: Comparison of the J-O intensity parameters of Eu^{3+} species obtained in glasses after gamma irradiation

The J-O intensity parameters (Ω_J) of the Eu^{3+} ion in the glass matrix reveal information regarding the covalence and surrounding of the metal ion. The parameter Ω_2 is related to the covalency and structural changes in the vicinity of the Eu^{3+} ion (short range effect) and Ω_4 is related to the long-range effects. A larger value of Ω_2 is an indication of a high covalence of the metal-ligand bonds and more distortion of the symmetry of the Eu^{3+} sites in that matrix compared to a matrix where the Ω_2 value is smaller [45, 46]. Large values for Ω_4 can be expected for organic ligands, because of low rigidity of these matrices. After irradiation of the glasses by gamma radiation, though there is no change in the symmetry and short range ordering in the glasses, as indicated from the trend observed for Ω_2, the long range ordering gets modified (as indicated from the Ω_4 values). This modification in the long range ordering could be manifested by the following two ways. First, the creation of defect centers due to gamma irradiation in the vicinity of the RE ion generates a large variation in the crystal filed which may bring about the modification in the long range ordering. Second, the breaking the Si-O and B-O bonds at regular sites also might be responsible for this modification.

3. EPR investigations

The room temperature EPR spectra of the irradiated glass containing Eu were similar to the base glass. The EPR stack plot of the gamma irradiated samples is shown in figure 4.9. It is observed that, there is no difference among the EPR spectra of the glasses irradiated with varying dose except the defect centre concentration.

The signal was analyzed in a similar manner as was done in case of the base glasses. Here also, the Hamiltonian parameters for the radicals generated due to gamma irradiation were evaluated which are listed below.

Paramagnetic species	g_1	g_2	g_3	A_1 (mT)	A_2 (mT)	A_3 (mT)	Δ_1 (mT)	Δ_2 (mT)	Δ_3 (mT)	L/G
BOHC	2.0355	2.0115	2.0025	0.87	1.33	1.36	1.5	0.5	0.5	0.5
E'	2.0010	2.0010	2.0010	-	-	-	0.25	0.25	0.25	0.5

Table-4.6 Hamiltonian parameters of the BOHC and E' centre radicals

It is seen that the parameters are similar to that of the base glass. The spin counting technique was also employed in this case to find out the defect centre concentration formed. For the glass irradiated with 900 kGy, the total defect centre concentration was evaluated to be 300 ppm. This also suggests that the bulk of the glass remains unaffected up to a gamma dose of 900 kGy.

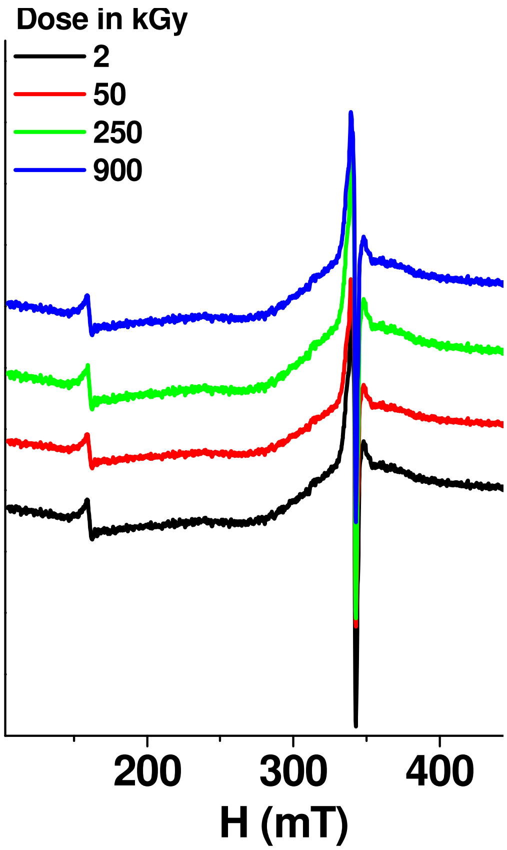

Figure 4.9. EPR stack plot for the irradiated Eu-glass samples.

It is worth noting that, we did not observe the formation of divalent Eu in the glass from EPR technique. This is in agreement with the PL data also which indicated the absence of divalent europium.

C. Studies on the Fe doped glass

The Fe doped glass after irradiation by gamma rays became intensely colored so it was not possible to record its emission or excitation spectra.

1. EPR investigations

In chapter 3 the EPR investigations of the Fe-glass prior to irradiation has been discussed in detail. It was observed that, before irradiation, iron gets stabilized as Fe^{3+} in both tetrahedral and octahedral environments. Figure 4.10 presents the room temperature EPR stack plot for the gamma irradiated borosilicate glass with 2.5 mol% iron. The spectrum shows two sets of lines at g ~ 4.3 and g ~ 2.0 as observed in case of the base glass and Eu incorporated glass.

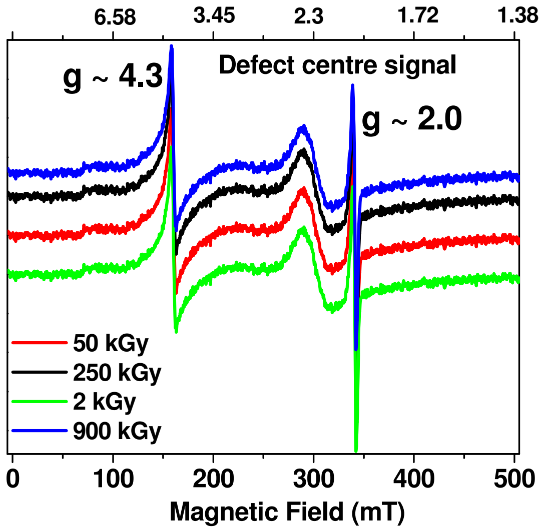

Figure 4.10. EPR stack plot of the gamma irradiated Fe incorporated glass; the upper X-acis shows the 'g' scale

As already discussed, the sharp and highly intense signal at g = 4.3 with line-width $\Delta_{pp} \approx 10$ mT is due to the isolated Fe^{3+} ions at tetrahedral or rhombic (lower) symmetric sites. The other signal at 'g' = 2.0 is a sharp line sitting on a broad signal with line-width $\Delta_{pp} \approx 100$ mT. This signal was absent in the unirradiated sample and thus it is attributed to the defect centers generated in the glass. The broad signal with 100 mT line width is also reported for the unirradiated glass and attributed to Fe^{3+} ions in sites of less distorted octahedral field [47]. The larger width of the signal could be due to the dipole–dipole interactions or super exchange interactions within the Fe^{3+} ion pairs.

2.Analysis of the defect center signals

In the irradiated base glasses, formation of BOHC and E' centers after gamma irradiation was established. In order to probe the formation of any other radicals in the Fe-glass, an EPR temperature variation experiment was planned.

Figure 4.11 presents the temperature variation of EPR signal generated due to defect centers in the Fe doped glass. For clarity, all the spectra are presented in double derivative mode. From this figure, it is observed that, upon annealing the glass sample at 500 K, most of the peaks in the EPR signal disappear due to electron hole recombination. Only one signal with 'g' values (obtained from simulation) g_1=2.0428, g_2=2.0120 and g_3=2.004 could be seen in the spectrum. This type of radical has previously been reported in glassy SiO_2 formed due to the breaking of a peroxy linkage (≡Si-O-O$^\bullet$) or by the capture of the O^{2-} radical on three fold coordinated Si atom [48]. Based on this, we name this radical as an Oxy radical.

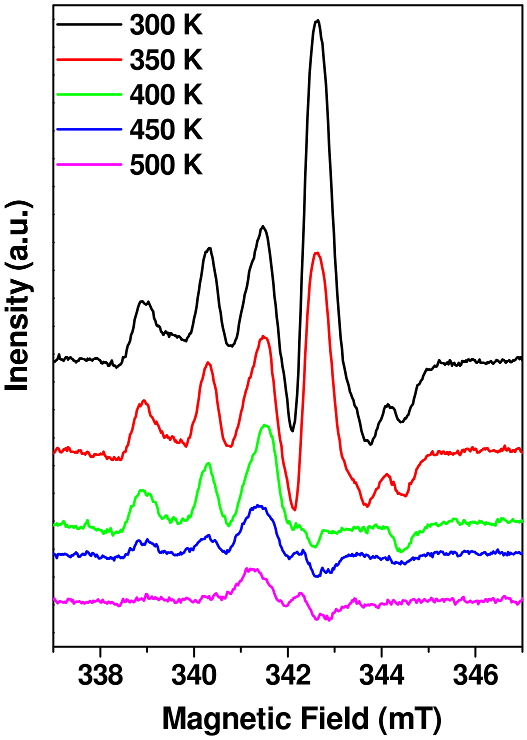

Figure 4.11. EPR spectra of defect centers generated in the irradiated borosilicate glass (doped with 2.5 mol% iron) as a function of temperature in double derivative mode

In addition to the oxy radical, another radical with 'g' values g_1=2.013, g_2=2.0088 and g_3=2.0023 could be observed which was named as hole centre (HC). This is due to a hole trapped on one or more oxygen atoms in the glass network. This particular type of species has been reported in X-ray irradiated alkali silicate glasses [49]. Moreover, in irradiated K_2O-SiO_2 glasses this type of 'HC' hole center has been identified and characterized unambiguously by Griscom using enriched SiO_2 with 95% ^{29}Si (I=1/2) and 33% ^{17}O(I=5/2) [50]. The intense and isotropic signal observed at g = 1.99 disappeared very quickly on annealing the sample beyond 400 K. This signal was having a negative 'g' shift compared to free electron g value of 2.0023 and was named an 'ET' centre. Based on the characteristics, it was attributed to either an F^+ center or an electron self trapped on a cation [51]. From the figure it can be seen that, the EPR signal intensity for the defect centers decrease on annealing at higher temperatures. This suggests the annealing of the radiation induced defect centers at higher temperatures.

Figure 4.12 shows the individual EPR spectra of all the radicals discussed above. The spectra are de-convoluted and generated using the Bruker SIMFONIA program. The respective spin Hamiltonian parameters are listed in Table 4.7. In this figure, the graph A shows the spectrum for the BOHC radical and the graph B shows that for the 'HC' and Oxy radicals. Graph C represents the experimental (black) and simulated spectrum (red) generated by addition of all the EPR signals from the different paramagnetic species.

Through these analyses, the exact chemical nature of the defect centers generated in the glass samples after gamma irradiation could be identified by EPR. The breaking of the Si-O-Si bond at regular sites was responsible for the formation of the Oxy Radical and E' center; where as breaking of the B-O-B bond was responsible for the formation of the BOHC radicals.

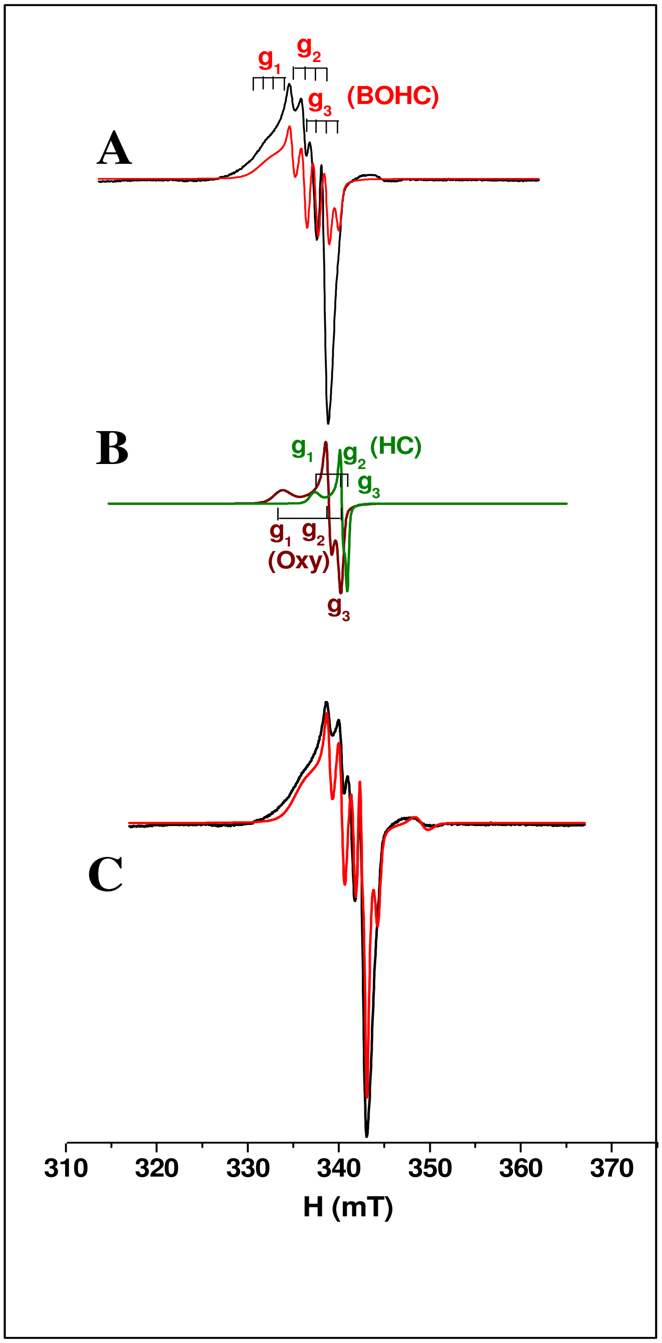

Figure 4.12. A-Room temperature experimental (black line) and simulated (red line) EPR spectra of the BOHC radical; B- experimental (brown line) and simulated (green line) EPR spectra of the peroxy and HC radicals. All the spectra were recorded with receiver gain = $3.2x10^4$ and microwave power = 6.30 mW.

Species	g_1	g_2	g_3	A_1 (mT)	A_2 (mT)	A_3 (mT)	Δ_1 (mT)	Δ_2 (mT)	Δ_3 (mT)	L/G
BOHC	2.0355	2.0115	2.0025	0.87	1.33	1.36	1.5	0.5	0.5	0.5
Oxy	2.0428	2.0120	2.004	-	-	-	1.5	0.5	0.5	0.2
HC	2.0213	2.0035	2.0000	-	-	-	1.0	0.3	0.3	0.2
E’	2.0010	2.0010	2.0010	-	-	-	0.25	0.25	0.25	0.5
ET	1.99	1.99	1.99	-	-	-	0.75	0.75	0.75	0.2

Table-4.7. Spin-Hamiltonian parameters for the different radicals formed in the irradiated glass.

3. Effect of iron content on the defect centre concentration

There are many reports in literature which suggest that the number of defect centers produced in the glasses by virtue of irradiation, decrease on doping with a particular metal ion. Griscom et al. have studied iron doped phosphate glasses by EPR and shown that Fe ions reduce the production of paramagnetic defects under irradiation [52]. Similar results have also been reported by Olivier et al. where a reduction in the amount of defects formed as a function of iron concentration in electron beam irradiated aluminoborosilicate glasses was observed [44].

Figure 4.13 shows the room temperature EPR spectra of iron doped alkali barium borosilicate glasses irradiated at the same dose (250 kGy) as a function of iron content. It was observed that the g=4.3 signal due to Fe^{3+} tends to saturate for sample with Fe content more than 1 mol%. One glance at the figure also reveals that, upon increasing the iron content in the glass, the EPR signal intensity at g~2.0, responsible for the defect centers decreases.

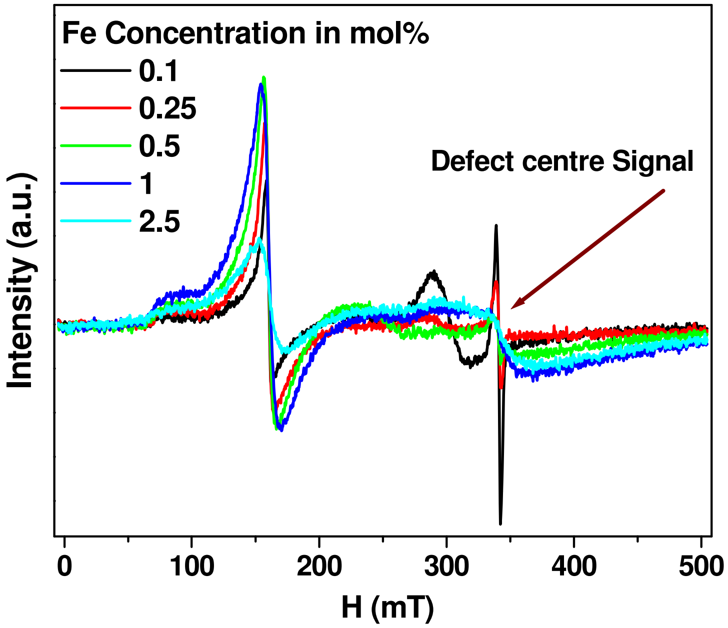

Figure 4.13. Room temperature EPR spectra of iron doped alkali barium borosilicate glasses irradiated at the same dose (250 kGy) as a function of iron content.

Through the spin counting technique, described earlier (page-6), the defect centre concentration and Fe^{3+} content was evaluated. The defect concentration calculated using the spin counting equation as a function of iron content in the glass is represented in figure 4.14.

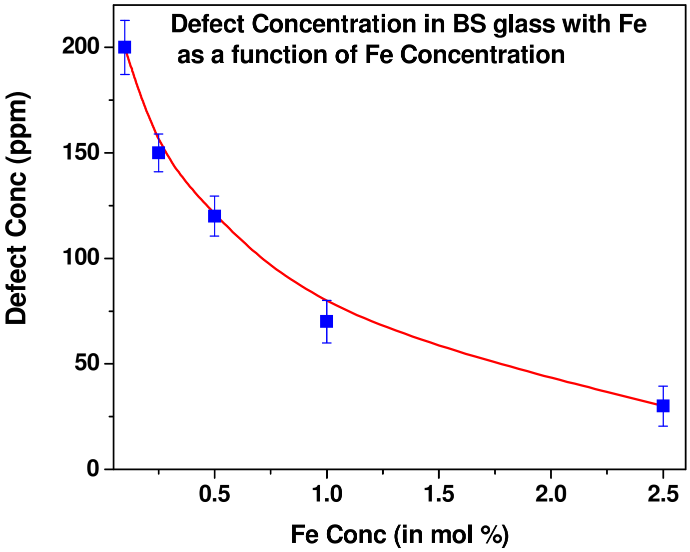

Figure 4.14. Defect centre concentration as a function of iron (Fe_2O_3) concentration.

It is observed from the figure that, the defect centre concentration reduces drastically upon increasing the iron content in the glass for the same radiation dose. Similar type of observations have also been reported by several authors in different types of glasses viz. Camara et al. in case of silicate glasses and Bogomolova et al. in case of fluoride glasses [53, 54]. McGann et al. have also reported similar reduction in the defect centre signal in iron doped HLW and ILW (intermediate level waste) glasses [12]. However, in these reports the extent of reduction in the defect centre concentration was quite significant as compared to the Trombay waste glass, even for small amounts of iron incorporation. This difference might be due to the difference in the glass composition. The Trombay waste base glass without any metal ion incorporation is known to contain 'Fe' ions as an impurity**.** Explanation for this type of reduction in the number of defect centers has been given by Debnath [55] and later by Olivier et al. [44]. According to Debnath, the hopping processes between ferrous and ferric ions in the glass are mainly responsible for this reduction in defects. Due to this hopping, the excitons produced during the electronic excitation are consumed and are not available for defect production. Olivier et al. have attributed this type of behavior in iron doped aluminoborosilicate glasses to the electron trapping process of the ferric ions occurring during the irradiation according to the reaction: $Fe^{3+} + e^{-} \rightarrow Fe^{2+}$. In case of UK HLW and ILW glasses also, the reduction in the defect centre signal has been attributed to this process [12]. These types of charge trapping processes have also been observed previously in borosilicate glasses with Zr^{4+}, Cr^{6+} and U^{4+} [56]. For the present nuclear waste glass of alkali barium borosilicate composition, we also attribute this reduction in the defect centre concentration to the later process of charge trapping. To further prove this, the Fe^{3+} content in the iron doped glasses before and after irradiation was calculated using similar spin counting equation. Figure 4.15 represents the Fe^{3+} content in the iron doped glass as a function of iron (Fe_2O_3) doping.

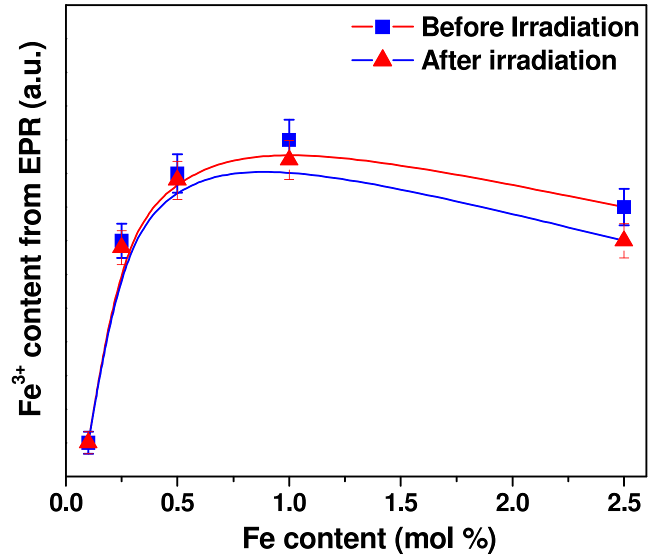

Figure 4.15. Fe^{3+} content as a function of iron content before and after irradiation

From the figure it is clear that, for the same gamma dose, the trivalent iron content in the glass reduces after irradiation. This indicates that, the trivalent iron traps one electron and gets converted to the divalent iron. The later being a non-Kramer ion (EPR silent), its signature is not seen in the EPR spectra. Moreover, a one-to-one correlation can also be seen in the reduction in the number of defect centers and reduction in the trivalent iron content. This proves that, indeed, the charge trapping process of the trivalent iron is responsible for the reduction in the defect centre concentration in the gamma irradiated borosilicate glasses.

4.4. Conclusion

Spectroscopic investigations were carried out on gamma irradiated alkali borosilicate glasses having similar composition to the Trombay waste base glass. The irradiations were done at 2, 50, 250 and 900 kGy. PL, PAS, FTIR and EPR studies were done on these samples in order to characterize the radiation induced changes taking place in the matrix. In addition, Eu and Fe were incorporated in the glass as local structural probes for studying radiation damage. It was observed that on gamma irradiation, boron based oxy hole centers are formed in the glass along with E’centers. A detailed EPR study revealed the formation of at least five different radical centers in the glass after gamma irradiation. PAS studies revealed the increase in the free volume in the glasses due to gamma irradiation. Judd-Ofelt parameters were evaluated for the Eu ion in the irradiated glasses. The trend in the J-O parameters suggested that on irradiation, there was no change in the short range ordering of the metal ions. However, the long range ordering of the Eu ions got modified along with its site distribution. It was observed that, for the same gamma dose, incorporation of more iron in the glass, reduces the formation of defect centers. This was attributed to charge trapping process of trivalent Fe ions present in the matrix. An EPR spin counting technique was employed to evaluate the defect centre concentration in the glasses formed due to gamma irradiation. It was observed that, the total defect centre concentration in the 900 kGy irradiated sample was only~350 ppm. This suggested that although there is formation defect centers along with increase in free volume size on irradiation, bulk of the glass remains unaffected.

References

1. C. P. Kaushik, R. K. Mishra, P. Sengupta, A. Kumar, D. Das, G. B. Kale and Kanwar Raj, J. Nucl. Mater., 358(2006) 129.
2. W. J. Weber, Nucl. Inst. Meth. Phys. Res. B 32 (1998) 471
3. R. C. Ewing, W. J. Weber, F. W. Clinard, Prog. Nucl. Energy 29 (1995) 63.
4. D.R. Cousens, S. Myhra, J. Non-Cryst. Solids 54 (1983) 345
5. K Sun, L M Wang , R C Ewing, W J Weber, Nucl. Inst. Meth. Phys. Res. B 218 (2004) 368
6. T Mizutani, J. Non Cryst Solids, 181 (1995) 123
7. M Arora, S. Baccaro, G. Sharma, D. Singh, K.S. Thind, D.P. Singh, Nucl. Inst. Meth. Phys. Res. B 267 (2009) 817
8. F.H. ElBatal, Y.M. Hamdy, S.Y. Marzouk, Mater. Chem. Phys. 112 (2008) 991
9. S. Baccaro, M. Arora, G. Sharm Nucl. Inst. Meth. Phys. Res. B 260 (2007) 613
10. G. Sharma, V.Rajendran, K.S.Thind, G. Singh, A. Singh, Physica B 404 (2009) 3371
11. W.J.Weber, R.C.Ewing, C.A.Angell, G.W.Arnold, A.N.Cormack, J.M.Delaye, D.L.Griscom, L.W.Hobbs, A.Navrotsky, D.L.Price, A.M.Stoneham, M.C.Weinberg, J. Mater. Res. 12 (1997) 1946.
12. O. J. McGann, P. A. Bingham, R. J. Hand, A. S. Gandy, M. Kavčič, M. Žitnik, K. Bučar, R. Edge, N. C. Hyatt, J. Nucl. Mater. 429 (2012) 353.
13. P. Kirkegaard, N. J. Pedersen, M. Eldrup, PATFIT-88, Risø-M-2740 Roskilde, Denmark, 1989.
14. G. Blasse, Prog. Solid St. Chem. 18 (1988) 79.
15. N. Kristianpoller, J. Lumin. 31/32 (1984) 299.
16. E. Malchukova, B. Boizot, D. Ghaleb, G. Petite, Nucl. Inst. and Meth. A 537 (2005) 411.
17. L. Nuccio, S. Agnello, R. Boscaino, B. Boizot, A. Parlato, J. Non-Cryst. Solids 353 (2007) 581.
18. M. Cannas, L. Vaccaro, B. Boizot, J. Non-Cryst. Solid 352 (2006) 203.

19. B.Boizot, G.Petite, D.Ghaleb, G.Calas, J. Non-Cryst. Solids 283 (2001) 179.
20. G. Kordas, J. Non-Cryst. Solids 351 (2005) 2358.
21. R.A.Weeks, J.Appl.Phys. 27 (1956) 1376.
22. J.A.Weil, J.R.Bolton, J.E. Wertz, Electron Paramagnetic Resonance: Elementary Theory and Practical Applications, John Wiley and Sons, New York, USA, (1994).
23. P.F. McMillan, A. Grazechnik, H. Chotalla, J. Non-Cryst. Solids 226 (1998) 239.
24. F. H. El Batal, A. H. Ashour, Mater. Chem. Phys. 77 (2002) 677
25. Y. B. Saddeek, M.S. Gaafar, S. A. Bashier, J. Non-Cryst. Solids 356 (2010) 1089
26. V.S. Yalmali, D.S. Deshingkar, P.K. Wattal, S.R. Bharadwaj, J. Non-Cryst. Solids 353 (2007) 4647
27. F.H.A. Elbatal, M.M.I. Khalil, N. Nada, S.A. Desouky, Mater. Chem. Phys. 82 (2003) 375
28. L. Stoch, M. Sroda, J. Mol. Struct. 511 (1999) 77.
29. E.I. Kamitsos, Phys. Chem. Glasses 44 (2003) 79.
30. J. Krogh-Moe, Phys. Chem. Glasses 6 (1965) 46.
31. H. Dunken, R.H. Doremus, J. Non-Cryst. Solids 92 (1987) 61.
32. M. Hasegawa, M. Tabata, M. Fujinami, Y. Ito, H. Sunaga, S. Okada, S. Yamaguchi, Nucl. Inst. and Meth. B 116 (1996) 347.
33. S. Damrefaer, T. Bretagnon, D. Kerr, J. Appl. Phys. 74 (1993) 884.
34. M. Hasegawa, M. Tabata, T. Miyamoto, Y. Nagashima, T. Hyodo, M. Fujinami, S. Yamaguchi, Mat. Sci. Forum, 269 (1995) 175.
35. W.H. Zachariasen, J. Am. Chem. Soc. 54 (1932) 3841.
36. R.A.B. Devine, Nucl. Instrum. Meth. B 91 (1994) 378.
37. S. J. Tao, J. Chem. Phys. 56 (1972) 5499.
38. M. Eldrup, D. Lightbody and J. N. Sherwood, Chem. Phys. 63 (1981) 51.
39. K. Gatterer, G. Pucker, H.P. Fritzer, Phys. Chem. Glasses 38 (1997) 293.

40. J. de Bonfils, G. Panczer , D. de Ligny , S. Peuget and B. Champagnon, J. Nucl. Mater. 362 (2007) 480
41. S. Baccaro, A. Cecilia, M. Montecchi, M. Nikl, P. Polato, G. Zanella, R. Zannoni, J. Non-Cryst. Solids 315 (2003) 271
42. G. Pucker, K. Gatterer, H. P. Fritzer, M. Bettinelli, M. Ferrari, Phys. Rev. B 53 (1996) 6225.
43. N. Ollier, G. Panczer, B. Champagnon, G. Boulon, P. Jollivet, J.Lumin. 94/95 (2001) 197.
44. F.Y. Olivier, B. Boizot, D. Ghaleb, G. Petite, J. Non-Cryst. Solids 351 (2005) 1061
45. C.K. Jorgensen and R. Reisfeld, J. Less-Common Met. 93 (1983) 107.
46. R. Reisfeld, E. Zigansky and M. Gaft, Mol. Phys. 102 (2004) 1319.
47. I. Ardelean, M. Peteanu, S. Filip, V. Simon, G. Gyorffy, Solid State Commun. 102 (1997) 341.
48. H. Hosono and Y. Abe, J. Non-Cryst. Solids, 95/96 (1987) 717.
49. D. A. Dutt, P. L. Higby and D. L. Griscom, J. Non-Cryst. Solids 130 (1991) 41.
50. D. L. Griscom, Nucl. Inst. and Meth. B, 1 (1984) 481
51. H. Hosono, N. Asada and Y. Abe, J.Appl Phys. 67 (1990) 2840
52. D. L. Griscom, C. I. Merzbacher, R. A. Weeks and R. A. Zuhr, J.Non-Cryst.Solids 258 (1999) 34
53. B. Camara and H. J. Oel, J. Non-Cryst. Solids 65 (1984)161
54. L. D. Bogomolova, F. Caccavale, V. A. Jachkin, N. A. Krasilnikova, N. O. Taguilsteva, O. A. Trul, J.Non-Cryst. Solids 255 (1999) 149
55. R. Debnath, J.Mater.Res., 16 (2001) 127
56. N. Ollier, "Verres de confinement de déchets nucléaires de type SON68 et leurs produits d'altération" spectroscopie de l'uranium et des terres rares", PhD Thesis, Lyon 1 University, France, 2002

Chapter-V

Spectroscopic investigations of the electron beam irradiated borosilicate waste glasses

5.1. Introduction

A major portion of the radioactivity present in the high level waste (HLW) comes from the short lived fission and activation products. These are mainly beta emitters having half lives ranging from few tens to few hundreds of years. As discussed already, borosilicate glass matrices used for fixing the waste, experience radiation damage because of this radioactive decay. These damages can significantly alter the glass structure which may influence their long term leaching behavior as suggested by many researchers [1-4]. Electron beam irradiations can simulate these effects of beta irradiation in HLW glasses to a great extent if not in totality. Several effects such as the rates of alkali ion exchange in radiation fields do show a non-Arrhenius behavior depending on both the irradiation dose and dose rate as suggested by Ojovan and Lee [5]. Nevertheless, many literature reports are available where nuclear waste glasses of varying compositions were irradiated by high energy electron beams to simulate the beta irradiation effects [6-21]. Among these, the reports from Ecole Polytechnique, France on the French nuclear waste glasses are noteworthy [6-18]. They have investigated different sets of virgin as well as doped glasses irradiated with electron beam by various spectroscopic techniques. Transition metal ions such as Cr^{3+} and rare earth ions such as Ce^{3+}, Sm^{3+}, Eu^{3+}, Gd^{3+} and Er^{3+} have been incorporated in the waste glass and the radiation damage was investigated using these ions as local structural probes. The migration and aggregation of alkali ions in these glasses under the influence of electron beam irradiation was also investigated by this group [7-9]. Iwata and Nishi have investigated the effect of electron beam irradiation on the impact value of the glass up to a dose of 0.43 MGy. The authors have also carried out EPR investigations of the glasses and verified the fact that an increase in the boron content of the glass enhances the resistivity to radiation damage [22]. Recently, Wang et al have reported the radiation induced damage and the recovery effects of GG17 (alkali alumino borosilicate) glasses irradiated with 1 MeV electron beam [23]. In addition to the creation of defect centers and modification of the glass network and structure [24], electron beam irradiation is also known to change other properties of the glass matrices such as density [25], surface morphology [26], Young's modulus and hardness [27] and mechanical properties [28]. In the last chapter, the gamma irradiation effects in the base glass as well as the doped glasses were investigated by various spectroscopic techniques. In this chapter the spectroscopic investigations of electron beam irradiated base glass has been reported. The irradiated glasses have been investigated by photoluminescence (PL), EPR, IR and positron annihilation spectroscopic techniques.

5.2. Experimental

The description of the sample preparation has been presentedin chapter-3. For electron beam irradiation, the glass samples were cut into discs of 10 mm diameter and polished on both sides. The irradiations were done at room temperature in an industrial 2 MeV and 20kW electron beam accelerator facility, ILU 6 (Budker Institute of Nuclear Physics, Russia) at Vashi, Navi Mumbai, India. For the present set of experiments, irradiations were carried out in a stationary mode under 1.8 MeV of energy and 400 mA of current. The samples were irradiated for varying time periods so as to get cumulative doses of 10^5, 10^6 and 10^8 Gy (J/kg). The irradiated glass samples were characterized by XRD, PL, EPR, FTIR and PAS techniques whose details are presented in chapter-2.

5.3 Results and Discussion

There were no changes in the XRD patterns for the electron beam irradiated glasses and the unirradiated glasses discussed in chapter 3. This indicated the absence of any crystalline phase in the irradiated samples. As with gamma irradiation, in case of electron beam irradiation also, because of formation of color/defect centers in the glass, the samples became dark colored and hence no absorption studies could be performed on the samples. The results of the other spectroscopic techniques on the electron beam irradiated glasses are discussed below.

A. PL investigations

In the gamma irradiated glasses, formation of non bridging oxy-hole centers, E’ centers and oxygen deficiency centers were observed. Figure 5.1 depicts the PL emission spectrum of the irradiated glasses as a function of dose with 190 nm excitation wavelength. The spectra look similar to that of the gamma irradiated ones except for the relative intensities of the peaks. The five peaks were assigned to different defect centers produced by radiation damage. The peaks at 685 and 505 nm were attributed to the non-bridging-oxygen hole centers. The bands at 455 nm and 255nm were attributed to oxygen deficiency centers and the emission from the E’ centre was observed at 229 nm. Here also, the generation of the NBOHC and E’ centers was attributed to the breaking of Si-O bonds at regular sites of the silicate network as a result of electron beam irradiation.

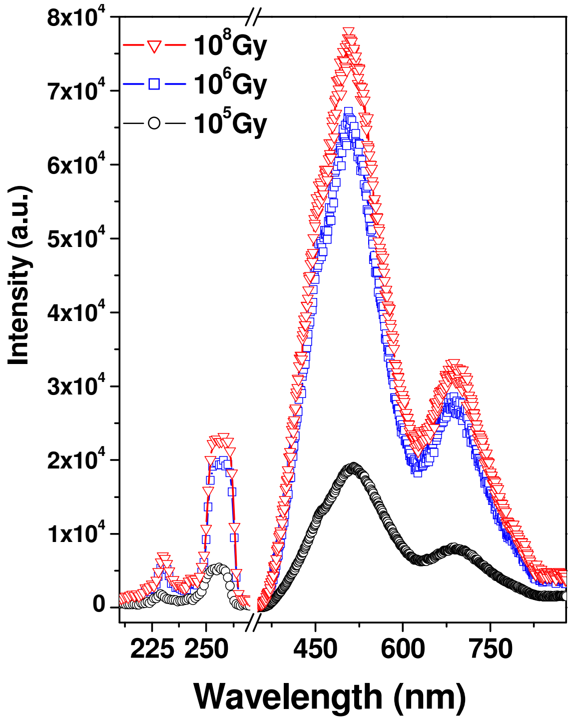

Figure 5.1 PL spectra of the electron beam irradiated base glasses as a function of radiation dose with λ_{ex} = 190 nm

B. EPR investigations

The X-band EPR spectra of the electron beam irradiated glass samples as a function of dose are shown in figure 5.2. The spectra are similar to that of the gamma irradiated glasses. There are two sets of signals one at g =4.3 and the other at g =2.0. As shown in chapter-3, the unirradiated samples did not show any signal except for the g=4.3 signal attributed to Fe^{3+} in lower symmetric environment. Thus the signal at g=2.0 was attributed to the defect centers generated due to electron beam irradiation.

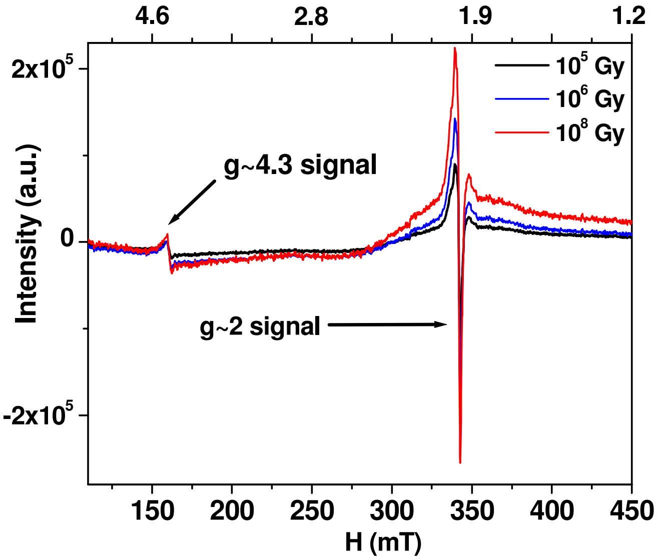

Figure 5.2 Room temperature EPR spectra of the electron beam irradiated glass samples as a function of dose; the upper axis (X) shows the ‘g’ scale.

It was seen that the nature of the paramagnetic defects formed on irradiation remained almost same on irradiation with higher doses. However, the intensity of EPR signal increased almost twice on increasing the dose from 10^5 Gray to 10^8 Gray suggesting that the paramagnetic defect concentration strongly increases as a function of irradiation dose. Figure 5.3 shows the EPR signal generated due to defect centres in the borosilicate glasses in a smaller scale. This ‘g ~ 2’ signal was consisting of superposition of several contributions from different paramagnetic centers induced by external irradiation. The free radicals formed during the radiolysis were identified on the basis of their g factors and hyperfine coupling constants (A). The de-convoluted spectra were used for obtaining the spin Hamiltonian parameters of the paramagnetic defects.

Several literature reports are available on the EPR investigations of electron beam irradiated borosilicate glass samples [29-34]. Most of these reports suggest the formation of paramagnetic defect centers such as boron oxygen hole center (BOHC), silicon hole centers (SHC), E' center and F^+ center etc in the glasses upon irradiation. The EPR signals due to different radicals were separated using different microwave powers (microwave power saturation) and their thermal stabilities.

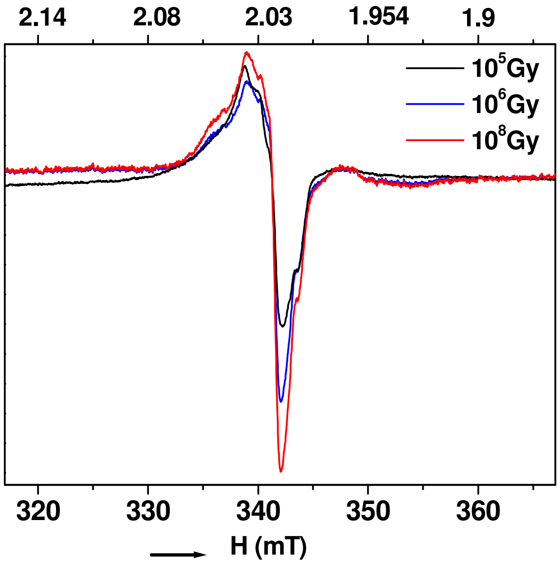

Figure 5.3 EPR spectra showing signal due to the defect centers as a function of dose in a smaller scale.

The EPR signal intensity of 10^8 Gy irradiated samples as a function of annealing temperature is shown in figure 5.4 (in second derivative mode). Major part of the signal at g ~ 2 showed a well resolved four line structure that was identified as coming from a BOHC. This signal was also observed in case of gamma irradiated glasses as described in chapter-4. The isotropic signal with g = 2.0010 and line width 0.25 mT was attributed to an E' centre. The 500 K annealed sample showed very less number of peaks due to electron hole recombination reactions. However, one signal with orthorhombic geometry having g_1=2.0425, g_2=2.0120 and g_3=2.005 was observed which was attributed to ≡Si-O-O$^\bullet$ radical (Oxy radical). These g-values were also confirmed from simulation experiments. In addition to this, another radical; HC_1 (g_1=2.015, g_2=2.0035 and g_3=2.0025); consisting of a hole trapped on one or more oxygen atoms in the glass network was observed. This type of centre is identical to that reported in X-ray irradiated alkali silicate glasses and also observed in the gamma irradiated Fe doped glasses [35]. Griscom has also identified and characterized this type of hole centers unambiguously in irradiated potassium silicate glasses [36]. On further annealing the sample beyond 400 K, the intense and isotropic signal observed at g=2.00 vanished (figure 5.4). This signal with a negative g shift with respect to the free electron g value of 2.0023 was attributed to an F^+ centre. This might be due to an electron self trapped on a cation such as divalent Ba. Similar to the case of gamma irradiated glass, we name this centre as an ET centre.

In addition to these radical signals, most of which were also seen in the gamma irradiated glasses, a weak and isotropic signal was observed at a field corresponding to g = 1.9653. This signal was present in the glass even after annealing the samples at 500 K. This type of isotropic and weak signal was observed previously and reported to be due to electron trapped on alkaline ions or by Zr^{4+} ions ($Zr^{4+}+e^- \rightarrow Zr^{3+}$) in some particular cases [37].

In the present case, this signal is named as an impurity (IMP) that is due to an electron trap impurity. The radical signals discussed above were generated by the Bruker SIMFONIA program and given in figure 5.5. The respective spin Hamiltonian parameters are listed in Table 5.1.

Here the spectrum in figure 5.5 D represents the experimental (black) and simulated spectrum (red) generated by addition of all the EPR signals from the different paramagnetic species.

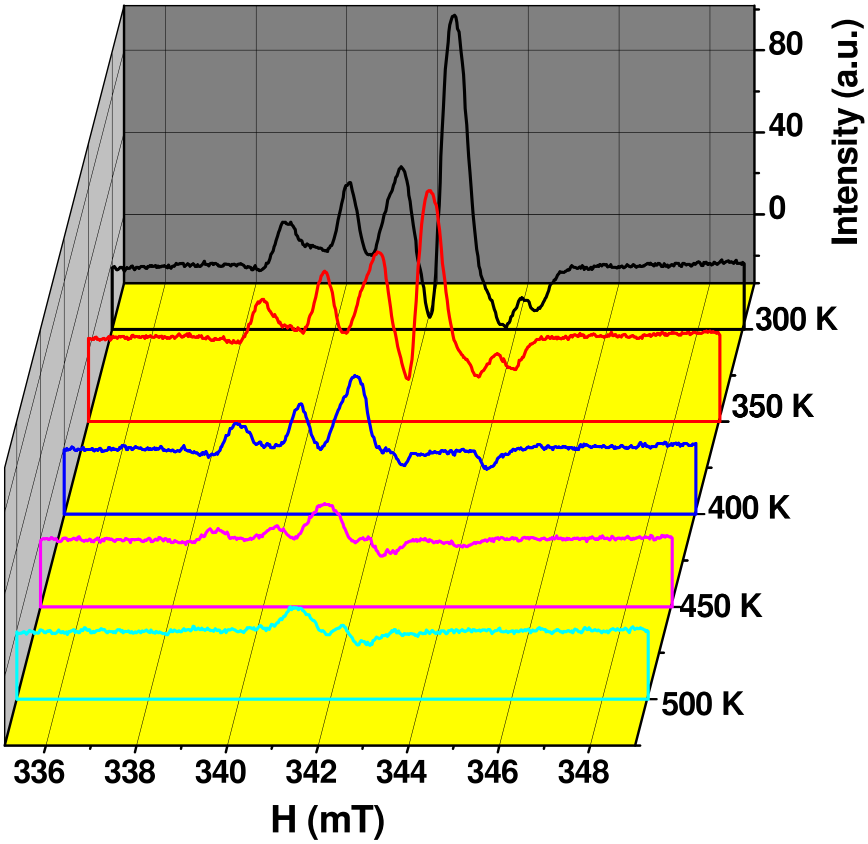

Figure 5.4 EPR spectra of the 10^8 Gy irradiated sample as a function of temperature

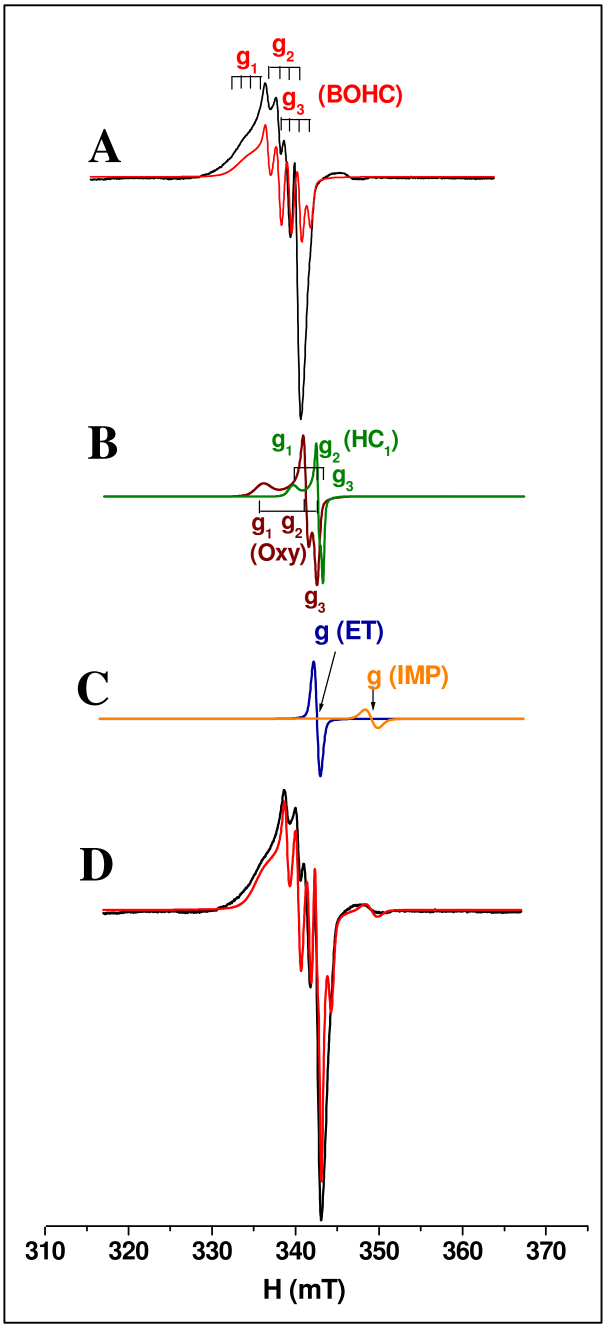

Figure 5.5 A- Room temperature experimental (black line) and simulated (red line) EPR spectra of the BOHC radical, B- experimental (brown line) and simulated (green line) EPR spectra of the oxy and HC radicals; C- experimental (blue line) and simulated (yellow line) EPR spectra of the ET and IMP radicals.

Paramagnetic species	g_1	g_2	g_3	A_1 (mT)	A_2 (mT)	A_3 (mT)	Δ_1 (mT)	Δ_2 (mT)	Δ_3 (mT)	L/G
BOHC	2.0355	2.0115	2.0025	0.87	1.33	1.36	1.5	0.5	0.5	0.5
Oxy	2.0425	2.0120	2.005				1.5	0.5	0.5	0.2
HC_1	2.0215	2.0035	2.0025				1.0	0.3	0.3	0.2
E’	2.0010	2.0010	2.0010				0.25	0.25	0.25	0.5
ET	2.0022	2.0022	2.0022				0.75	0.75	0.75	0.2
IMP	1.9653	1.9653	1.9653				0.15	0.15	0.15	0.5

Table-5.1 Spin-Hamiltonian parameters for the different radicals formed in the irradiated glass. Here ‘g_i’ (i =1,2 and 3) are the individual radicals ‘g’ values, ‘A_i’ are the hyperfine coupling constants, Δ_i are the line widths of the individual EPR spectrum and L/G is the relative Lorentzian to Gaussian ratio used to simulate the EPR spectrum

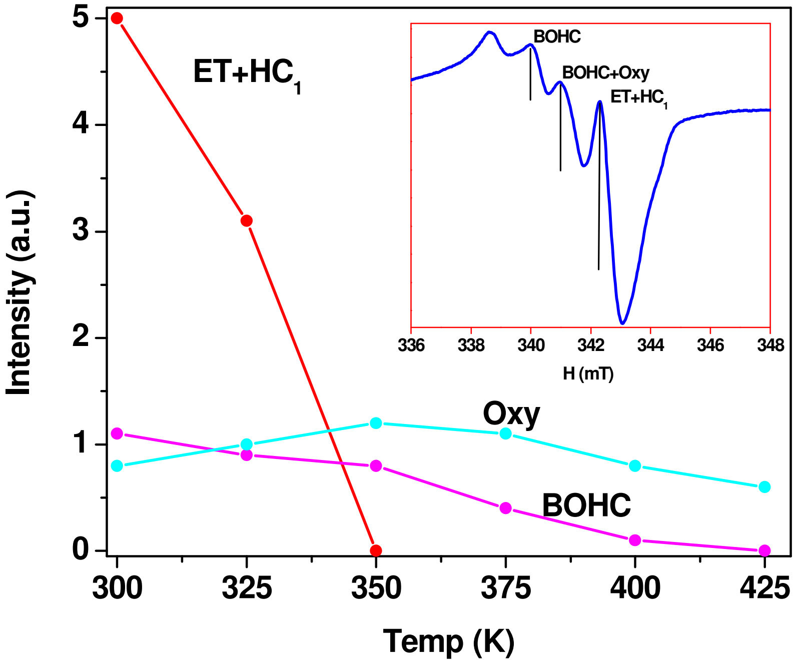

Figure 5.6- EPR signal intensities of the radicals as a function of annealing temperature. The inset figure shows the respective radical signal positions and their intensities chosen for the calculation.

The variation of EPR signal intensities of the radicals as a function of annealing temperature is shown in Figure 5.6. The intensity of the BOHC radical was estimated from the 2nd component of quartet hyperfine structure of 'g_2' component as this line is free from other radical signal and its intensity truly represents the intensity of BOHC. In order to remove the contribution of the BOHC resonance from the hole trapped center (Oxy), the intensities plotted for Oxy radical were calculated by subtracting the intensity of BOHC + Oxy intensity from BOHC intensity. As indicated above, the ET+HC$_1$ signal decays very quickly as a function of annealing temperature. The Oxy radical intensity appears to increase at first, but this increase may be due to the removal of the overlapping BOHC spectrum.

The EPR data obtained in this study allowed us to identify unequivocally the exact chemical nature of the defect centers formed in the nuclear waste glasses after electron beam irradiation. The formation of Oxy radicals and E' centers in the borosilicate glass can be attributed to the breaking of the regular Si-O-Si bonds due to irradiation. Similarly, the breaking of B-O-B bonds at regular sites leads to the formation of BOHC type of radicals in the system.

By using the EPR spin counting technique, already discussed in chapter-4, we have calculated the exact concentration of the defect centers formed in the glass as a result of irradiation. In this case, the defect concentration in the 10^8 Gy irradiated sample was calculated to be 2.8×10^{19} spins / 100 mg of the sample. Considering the average molecular weight of the glass, this total defect concentration in the glass comes to hundreds of ppm. The observation of clear hyperfine lines in the EPR spectra also states this fact though qualitatively.

C. IR Investigations

Figure 5.7 shows the infrared absorption spectra for the glass samples before and after irradiation. The active vibrations of the borate and silicate groups are expected to absorb in the wavenumber region higher than 550 cm^{-1} [38, 39] and thus only this region of interest is shown in the figure. The figure shows the following absorption bands:

(a) Small band at 700-800 cm^{-1},

(b) A very broad absorption band in the region 900-1200 cm^{-1},

(c) Another broad absorption band in the range 1250-1400 cm^{-1}

There was no significant change in the band positions of the irradiated samples as compared to the unirradiated ones. As discussed already, in borosilicate based glasses, the Si atom is thought of mainly as a part of tetrahedral SiO_4 units; where as the B atoms are believed to be a part of 3 fold or

4 fold coordinated borate groups as discussed earlier. The stretching vibrations of Si-O-Si in the SiO_4 tetrahedra are usually observed in the range 900-1200 cm^{-1} depending on the other cations present in the glass.

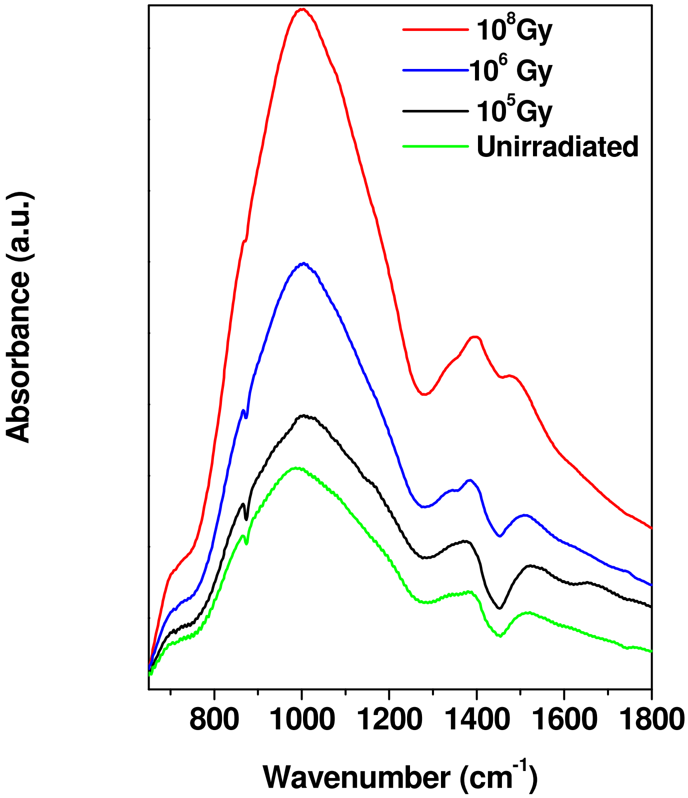

Figure 5.7- FTIR spectra for the unirradiated and electron beam irradiated sodium-barium borosilicate glass samples.

On the other hand, borate groups show two characteristic stretching bands, one derived from the B–O bond stretch in the trigonal BO_3 at about 1300-1500 cm^{-1} and the other due to B-O bonds in BO_4 tetrahedra in the region 950-1100 cm^{-1} [39,40]. In view of this argument, the broad absorption band observed in 900-1200 cm^{-1} region is assigned to the combined stretching vibrations of Si-O-Si and B-O-B tetrahedral networks. Similar types of features due to combined vibration of Si-O and B-O units have also been reported previously in alumino borosilicate, barium borosilicate, lead-borosilicate and sodium borosilicate glasses [38, 39, 41 and 42]. Similarly, the band at 1250-1400 cm^{-1} region is attributed to stretching vibrations of BO_3 triangular units with non-bridging oxygens (NBOs) [38, 41].

The weaker but significantly clear band at 700-800 cm^{-1} is attributed to the bending vibrations of the bridging oxygen between the trigonal BO_3 groups [40, 43].

D. PAS investigations

Positron annihilation lifetime results for the irradiated borosilicate glass samples as a function of electron dose are shown in figure 5.8. Graph 'A' shows the variation of the o-Ps (ortho-positronium) *pick-off* life time and the graph 'B' shows the variation in the o-Ps *pick-off* intensity.

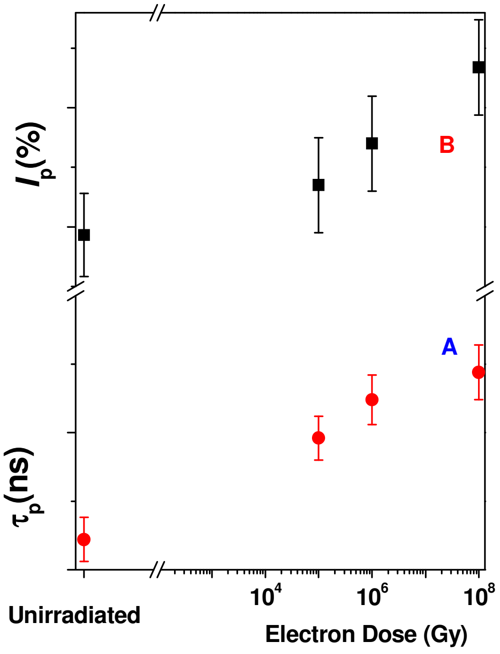

Figure 5.8-Variation of the pick off life time and pick off intensity of the irradiated samples with dose

The results showed that, the o-Ps *pick-off* lifetime (τ_p) and the *pick-off* intensity (I_p) in electron-irradiated samples are more than the unirradiated ones and it increases with the dose. The increase in o-Ps lifetime is related to the increase in free volume size inside the borosilicate glass samples due to the effect of electron irradiation. The free volume size of the glass sample (*R*) can be calculated from *pick-off* lifetime (τ_p) using the Tao-Eldrup equation shown below [44, 45].

$$\tau_p = \frac{1}{2}\left(1 - \frac{R}{R+\Delta R} + \frac{1}{2\pi}\sin\frac{2\pi R}{R+\Delta R}\right)^{-1} \tag{5.1}$$

Here τ_p is measured in ns and *R* (radius of the spherical free/defect volume) is in Å. The ΔR (1.66 Å) is the electron layer thickness inside the wall of the spherical free volume. The *pick-off* intensity was used to calculate the free-volume fraction (*f*) in the glass sample using the following relation [46].

$$f = cI_pV_f \tag{5.2}$$

Where *c* is the normalization constant and V_f (=$4/3\pi R^3$) is the free volume. *R* is the radius which can be obtained using equation 5.1. The *c* value was not measured in this work, but as it is a constant, the fractional free volume (*f*) must be proportional to the product ($I_p \times V_f$). It is seen in figure 5.9 that the value of ($I_p \times V_f$) increases with the electron radiation dose signifying the creation of new free volume sites with increase in radiation dose received by the sample. The values of the free volume size and fraction (without the proportionality constant) obtained from equations 5.1 and 5.2 are listed in table 5.2.

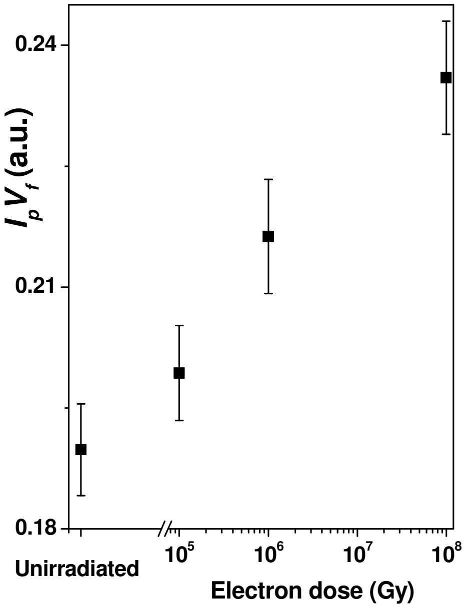

Figure 5.9- Variation of ($I_p{\times}V_f$) with radiation dose

Dose received by the glass sample	o-Ps pick off life time (ns)	Radius of the free volume (Å)	Free volume fraction ($I_p{\times}V_f$)
Unirradiated	1.11±0.06	1.83±0.02	0.188
10^5 Gy	1.48±0.08	2.32±0.05	0.199
10^6 Gy	1.62±0.09	2.48±0.07	0.216
10^8 Gy	1.72±0.1	2.58±0.09	0.235

Table-5.2: Positron annihilation data of the unirradiated and electron beam irradiated glass samples

The increase in the positron life time with irradiation suggested that, the positron annihilation process gets delayed because of its trapping in voids also referred to as free volume. As a result of irradiation, more and more such type of voids or defects trap the positron and inhibit the annihilation process thus increasing the life time. However, the overall glass network remains unaffected by the irradiation as confirmed from the IR data. EPR and PAS are microscopic techniques that can identify changes of the order of few tenth of ppm also. However, IR being a bulk technique provides information regarding changes taking place in the bulk.

It is worth mentioning here that, the high dose rate, because of high electron beam current used for the present investigation can cause some effects which might not actually be present in the HLW glasses irradiated at the same total dose. For example, the increased viscous flow due to nano scale quasi melting of both alumino borosilicate and sodium borosilicate glasses, on high energy electron beam irradiation has been reported by Möbus et al [47]. Insitu measurements might be useful to fully simulate the conditions of beta irradiation. However, the nature of radiation induced defect centers formed in the glasses will be identical irrespective of the means of irradiation as suggested separately by many authors, viz Weber et al [1, 2], Malchukova et al [15-18] and Boizot et al [9].

The formation of the defect centers discussed in the study (including the oxygen hole centers) do contribute to the unbinding of the alkali metals and results in an enhanced rate of ion exchange as shown earlier [48]. However, as seen from the present study, no major changes occur in the bulk of the glass. But more investigations on the Trombay waste glasses are required to establish an one to one correlation in between the radiation induced point defects and leaching of the glass matrix.

5.4 Conclusion

In summary, PL, EPR, IR and PAS investigations were carried out on electron beam irradiated Trombay nuclear waste base glasses to simulate the effects of beta irradiation. The PL data suggested the formation of NBOHC and E’-centers in the glasses after irradiation. EPR investigations were done on the samples to have a deep understanding regarding the defect centers formed in the irradiated glasses and get an idea about their chemical nature. These investigations suggested the formation of at least five different species in the irradiated glass samples. Exact Hamiltonian parameters for the radicals were evaluated by EPR simulation technique using SIMFONIA program. PAS studies indicated increase in the free volume size and fraction in the glasses after irradiation indicating more and more trapping of the positrons in the glass. Not much change in the glass network was observed from FTIR data. A spin counting technique was employed to evaluate the number of defect centers in the glass irradiated with highest electron dose. It was observed that even at 10^8 Gy, the number of defect centers are few hundreds of ppm. This in a way confirms the radiation stability of the barium borosilicate glasses routinely used for vitrifying the research reactor nuclear waste.

References

1. W.J.Weber, R.C.Ewing, C.A.Angell, G.W.Arnold, A.N.Cormack, J.M.Delaye, D.L.Griscom, L.W.Hobbs, A.Navrotsky, D.L.Price, A.M.Stoneham, M.C.Weinberg, J. Mater. Res. 12 (1997) 1946.
2. W.J. Weber, Nucl. Inst. and Meth. B 32 (1988) 471.
3. R. C. Ewing, W. J. Weber, F. W. Clinard, Prog. Nucl. Energy 29 (1995) 63.
4. D. M. Usher, J. Phys. C: Solid State Phys. 14 (1981) 2039.
5. M. I. Ojovan, W. E. Lee, J. Nucl. Mater. 335 (2004) 425
6. B. Boizot, G. Petite, D. Ghaleb, N. Pellerin, F. Fayon, B. Reynard, G. Calas, Nucl. Instrum. And Meth. B 166/167 (2000) 500
7. B. Boizot, G. Petite, D. Ghaleb, B. Reynard, G. Calas, J. Non-Cryst.Solid 243 (1999) 268
8. B. Boizot, N. Ollier, F. Olivier, G. Petite, D. Ghaleb, E. Malchukova, Nucl. Instrum. And Meth. B 240 (2005) 146
9. B. Boizot, G. Petite, D. Ghaleb, G. Calas, Nucl. Instrum. And Meth. B 141 (1998) 580
10. N. Ollier, B. Boizot, B. Reynard, D. Ghaleb, G. Petite, J. Nucl. Mater. 340 (2005) 209
11. N. Ollier, B. Champagnon, B. Boizot, Y. Guyot, J. Non-Cryst.Solid 323 (2003) 200
12. N. Ollier, B. Boizot, B. Reynard, D. Ghaleb, G. Petite, Nucl. Instrum. And Meth. B 218 (2004) 176
13. N. Ollier, B. Boizot, P. L'henoret, S. Guillous, G. Petite, J. App. Phys. 105 (2009) 113515
14. N. Ollier, J.-L. Doualan, V. Pukhkaya, T. Charpentier, R. Moncorgé, S. Sen, J. Non-Cryst. Solids 357 (2011) 1037
15. E. Malchukova, B. Boizot, D. Ghaleb, G. Petite, J. Non-Cryst. Solids 352 (2006) 297
16. E. Malchukova, B. Boizot, G. Petite, D. Ghaleb, J. Non-Cryst. Solids 354 (2008) 3592

17. E. Malchukova, B. Boizot, Mater. Res. Bull. 45 (2010) 1299
18. E. Malchukova, B. Boizot, G. Petite, D. Ghaleb, J. Non-Cryst. Solids 353 (2007) 2397
19. G. Buscarino, S. Agnello, F. M. Gelardi, R. Boscaino, Phys. Rev. B 80 (2009) 094202
20. M. Antonini, A. Manara, S.N.Buckley, S.N.Manthorpe, J. Phys. Chem. Solids 46 (1985) 281
21. G. Yang, G. Möbus, P. A. Bingham, R. J. Hand, Phys. Chem. Glasses: Eur. J. Glass Sci. Technol. B 50 (2009) 378
22. K. Iwata, Y. Nishi, Mater. Trans. 51 (2010) 121
23. Q. Wang, Z. Zhang, H. Geng, C. Sun, D. Yang, S. He, Z. Hu, Nucl. Instrum. And Meth. B 281 (2012) 1
24. O. Gedeon, J. Machacek, S. Charvatova, J. Non-Cryst. Solids 356 (2010) 2473
25. W. Primak, R. Kampwirt, J. Appl. Phys. 39 (1968) 5651
26. O. Gedeon, K. Jurek, I. Drbohlav, J. Non-Cryst. Solids 353 (2007)1946
27. O. Gedeon, J. Lukeš, K. Jurek, Nucl. Instrum. And Meth. B 275 (2012) 7
28. S. Nakano, S. Muto, T. Tanabe, Mater. Trans. 47 (2006) 112
29. P. Lombard, N. Ollier, B. Boizot, J. Non-Cryst. Solids 357 (2011) 1685
30. F.Y. Olivier, B. Boizot, D. Ghaleb, G. Petite, J. Non-Cryst. Solids 351 (2005) 1061
31. I. A. Shkrob, B. M. Tadjikov, A. D. Trifunac, J. Non-Cryst. Solids 262 (2000) 6
32. I. A. Shkrob, B. M. Tadjikov, A. D. Trifunac, J. Non-Cryst. Solids 262 (2000) 35
33. I. A. Shkrob, B. M. Tadjikov, S. D. Chemerisov, A. D. Trifunac, J. Chem. Phys. 111 (1999) 5124
34. D.L.Griscom, J. Non-Cryst. Solids 13 (1973/74) 251
35. D. A. Dutt, P. L. Higby, D. L. Griscom, J. Non-Cryst. Solids 130 (1991) 41.
36. D.L.Griscom, J. Non-Cryst. Solids, 64 (1984) 229.

37. D.L.Griscom, R.J.Ginther, J. Non-Cryst. Solids 113 (1989) 146.
38. Y. B. Saddeek, M.S. Gaafar, S. A. Bashier, J. Non-Cryst. Solids 356 (2010) 1089
39. V. Kumar, O.P. Pandey, K. Singh, Physica B 405 (2010) 204
40. L. Stoch, M. Sroda, J. Mol. Struct. 511–512 (1999) 77.
41. S. Baccaro, Monika, G. Sharma, K.S. Thind, Devinder Singh, A. Cecillia, Nucl. Inst. and Meth. B 260 (2007) 613.
42. K. El-Egili, Physica B 325 (2003) 340.
43. E.I. Kamitsos, Phys. Chem. Glasses 44 (2003) 79.
44. S. J. Tao, J. Chem. Phys. 56 (1972) 5499.
45. M. Eldrup, D. Lightbody and J. N. Sherwood, Chem. Phys. 63 (1981) 51.
46. Y. Kobayashi, W. Zheng, E. Yemer, J. McGervey, A. M. Jamieson and R. Simha, Macromol. 22 (1989) 2302.
47. G. Möbus, M. Ojovan, S. Cook, J. Tsai, G. Yang, J. Nucl. Mater. 396 (2010) 264.
48. M. I. Ojovan, A. Pankov, W.E. Lee, J. Nucl. Mater. 358 (2006) 57

Chapter-VI

Spectroscopic investigations of the heavy ion irradiated borosilicate waste glasses

6.1. Introduction

In Chapter-1, a detailed discussion regarding the various types of radiation sources in the high level waste (HLW) is presented. There are mainly two types of radiation sources in the HLW. Alpha particles, primarily coming from the minor actinides, such as, ^{237}Np, $^{241,\ 243}$Am, $^{242,\ 244,\ 245}$Cm and beta particles coming from the fission and activation products, such as, ^{90}Sr, ^{99}Tc, ^{129}I, ^{135,137}Cs, etc. Out of the two types of radiations mentioned above, alpha decays from the minor actinides are responsible for most of the atom displacements taking place in the nuclear waste glass. Many literature reports are available discussing the effects of alpha radiation damage on the nuclear waste glasses.

Weber et al. have given a comprehensive review of the studies in the field of radiation effects in glasses that are to be used for the immobilization of high-level nuclear waste and plutonium disposition [1]. The long-term effects of α-decay events have been simulated in a number of waste glass compositions by incorporating short-lived actinides such as ^{238}Pu ($t_{1/2}$ = 87.7 yrs) or ^{244}Cm ($t_{1/2}$ = 18.1 yrs) to achieve 10^{18} to 10^{19} α-decay events/gm in laboratory time periods of up to several years [2-7].

External heavy ion irradiation is also a convenient laboratory technique for simulating the alpha damages in the borosilicate glasses [8]. Several reports are available in the literature where heavy ion irradiation studies have been done on nuclear waste glasses to assess the effects of alpha decay on the structural properties of the glass matrix [9, 5-7].

Most of the literature reports cited above have revealed variations in the macroscopic properties of the glass matrix due to accumulation of alpha decay. Depending on the specific chemical composition, the nuclear waste glasses may undergo volume expansion or densification. Various mechanical properties of the glass matrix have also been reported to alter at about 2×10^{18} α/gm. Bonfils et al have studied a simplified French nuclear waste glass, that is, R7T7 glass, under gold ion implantation and reported the changes in the glass structure as a result of irradiation [10]. The authors have used Eu^{3+} as a local structural probe and followed the changes occurring in the Eu environment by fluorescence line narrowing spectroscopic technique. In another report, the authors have estimated the changes in the macroscopic properties of the irradiated glasses [11].

In another report by Peuget et al. the R7T7 glass was incorporated with varying amounts of $^{244}Cm_2O_3$ to study the cumulative effects of alpha dose and the dose rate [12].

The literature on the macroscopic and microscopic changes occurring in amorphous silica matrix under ion irradiation has been reviewed by Devine [13]. Analysis of defect centres generated by ion implantation in borosilicate and phosphate glasses has been described by Bogomolova et al. [14]. Matzke has published two comprehensive reviews on the damage produced in various waste matrices including borosilicate glasses due to alpha bombardment and actinide incorporation [15, 16]. The effect of He, Ar and Xe ion implantation in alkali borosilicate glasses has been studied by Arnold [17]. Sato et al. have compared the effects of gamma, electron and ion beam irradiation on simulated waste glasses [18].

The present chapter deals with the spectroscopic investigations of the radiation induced changes in the barium borosilicate (base) glasses irradiated with ^{4}He and ^{12}C beams.

6.2. Experimental

For the present set of investigations, the base glass composition was selected. The glass samples were cut into discs of 10 mm diameter and 1 mm thickness and polished prior to irradiation.

All the heavy ion irradiations were carried out at the 30^0 North beam line of BARC-TIFR pelletron facility located at Tata Institute of Fundamental Research (TIFR), Mumbai. The glass samples were wrapped in conducting (aluminum) foils to decrease the beam energy. The beam current was measured from the insulated target which acted as beam dump. The ratio of unsuppressed and suppressed beam current was obtained by measuring the beam current without and with the target respectively.

For ^{12}C irradiation, the beam energy was kept at 20 MeV (q=4+) with 150 nA average current. For the alpha beam, the energy was 12 MeV and the average beam current was 40 nA. Three sets of samples were irradiated for cumulative time periods so that the total dose received by the samples are $\sim 1\times10^{10}$ Gy, 7×10^{10} Gy and 1×10^{11} Gy. Since the penetration depth of the beam is restricted to few microns in the glass samples, the bulk spectroscopic techniques discussed in the previous chapters were not used in this case. Special surface techniques such as micro Raman spectroscopy and FTIR spectroscopy in ATR (attenuated total reflection) mode were used to study the radiation induced changes taking place in the glasses. Micro Raman investigations were done on a Horiba Jobin Yvon unit (HR-800), using an Ar^+ source of 514 nm and 40 mW power. The confocal hole opening was kept at 100 μ with a resolution of 1 cm^{-1} and

200 - 2000 cm^{-1} spectral range. FTIR studies were carried out using a Bruker - Vertex 80 V system.

6.3. Results and Discussion

A. Investigations by Raman spectroscopy

1. Alpha irradiation

Figure 6.1 shows the micro Raman spectra of the alkali barium borosilicate glasses prior to irradiation. Here, the broad and intense band observed at ~ 470 cm^{-1}, is attributed to the mixed bending and stretching modes of Si-O-Si [11, 19 and 20]. The smaller peaks observed in the range 600-790 cm^{-1} are attributed to the vibrations of metaborate units as suggested by Bonfils et al [11].

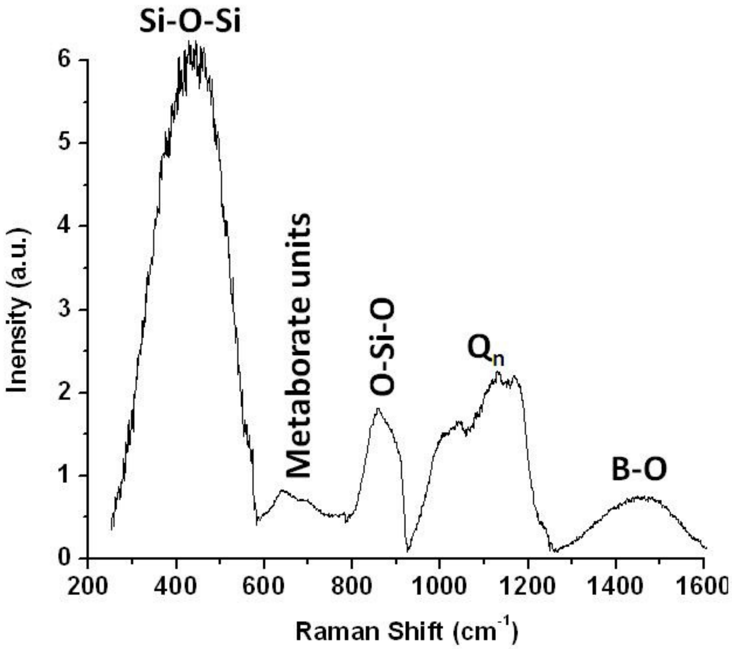

Figure 6.1 High resolution micro Raman spectrum of the unirradiated Trombay nuclear waste glass

The band observed at 850 cm^{-1}, is because of symmetric vibrations of 'Si' atoms around bridging oxygens ('O-Si-O' groups).

The broad band consisting of multiple peaks observed in the wavenumber range 900-1250 cm^{-1} is because of the Q_n species which refers to the SiO_4 with 'n' bridging oxygen. The small and broad band seen at ~1450 cm^{-1} is due to the characteristic vibration of B-O groups.

The broad band responsible for the Q_n species, observed at 900-1250 cm^{-1}, was deconvoluted to get the band positions of the Q_1-Q_4 species. This is represented in figure-6.2.

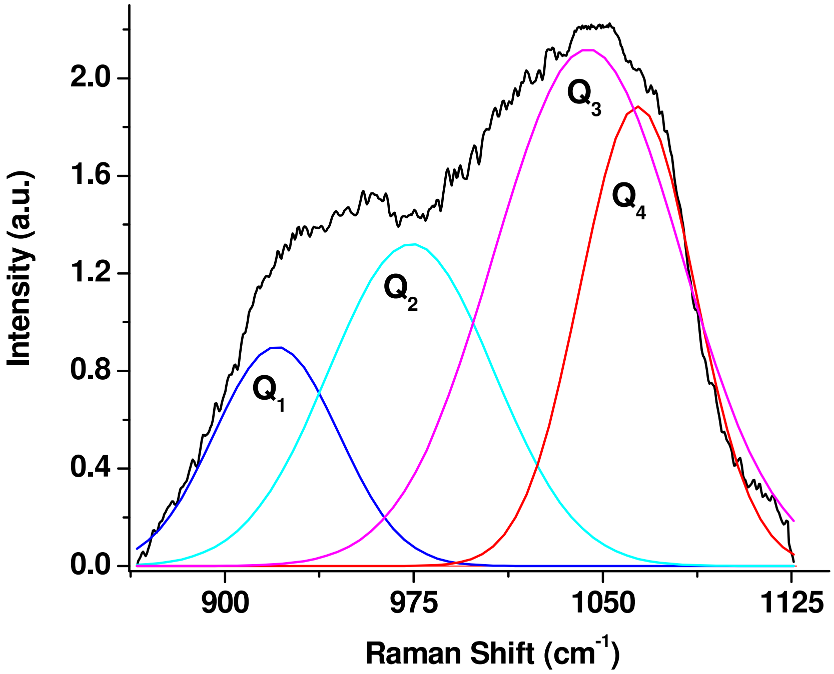

Figure 6.2 Deconvolution of the Q_n band into Q_1-Q_4 positions.

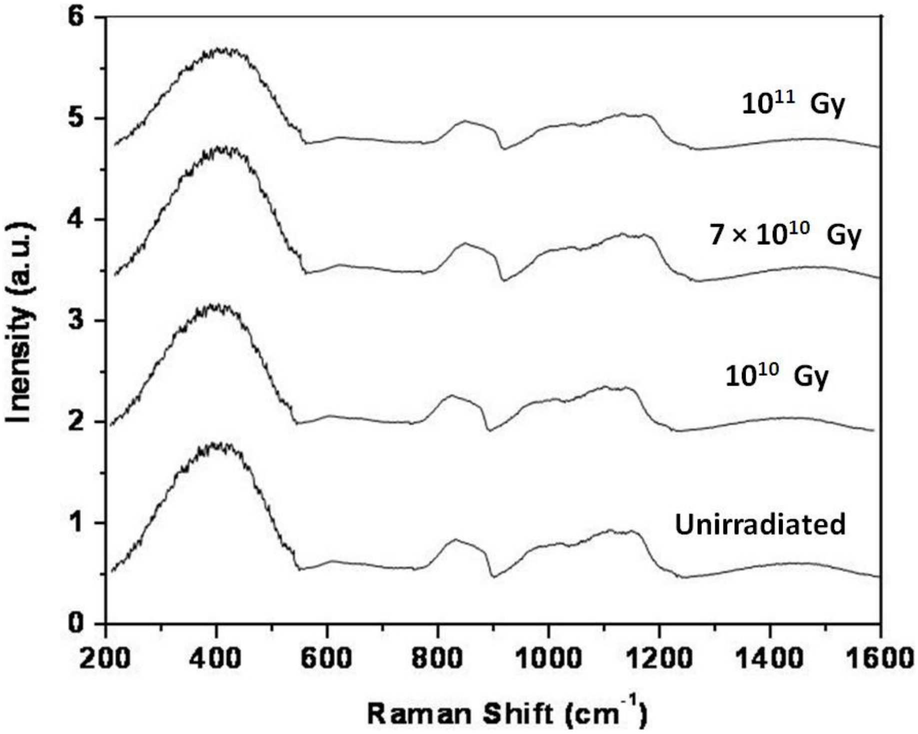

Figure 6.3 Raman spectra of the glass samples irradiated with ^{4}He as a function of dose

Figure-6.3 shows the Raman spectra of the glass samples after irradiation by ^{4}He beam with varying dose. It could be seen from the figure 6.3 that on irradiation, all the peaks were shifted by 10-25 cm^{-1} towards the higher wavenumber. This is more prominent in the vibrations of the Si-O-Si group (400 cm^{-1}). This shift is because of the reduction in the mean angle of the Si-O-Si bonds as a result of alpha irradiation [21].

It was also observed that, with increasing dose, the Q_n mean band position shifted towards a higher 'n' value indicating increase of the silicate network polymerization under alpha irradiation. Manara et al. attributed this type of structural evolution to the migration and aggregation of alkali ions during the irradiation [22]. In the report by Bonfils et al., a change in the Si-O-Si bond angle of the silicate network was observed due to the heavy ion (Au ions) implantation [11]. In addition, a change in the Q_n position was also witnessed in the glass which the authors related to the modifications in the silicate network. Similarly, in an earlier report by Ollier et al, it was shown from Raman investigations that electron beam irradiation in borosilicate glasses, increases the polymerization and molecular oxygen formation due to the migration of the alkali ions present in the glass [19]. In addition, we had also seen polymerization in the electron beam irradiated Trombay nuclear waste glasses as described in chapter-5.

It is inferred from the above Raman spectroscopic results that, alpha irradiation of the Trombay nuclear waste glass, modifies the glass network enhancing the alkali migration and higher extent of polymerization.

2. *^{12}C irradiation*

Figure 6.4 shows the Raman spectra of the ^{12}C beam irradiated glass samples. Compared to the alpha irradiated samples, the spectra of the carbon beam irradiated samples were noisy and broad. The peak positions of the various bands were similar to that observed for the alpha irradiated samples except the relative intensities of the peaks. In this case also, all the peaks were shifted by 10-25 cm^{-1} towards the higher wavenumber side in the irradiated samples as compared to the unirradiated sample. In figure 6.5 Raman spectra of the Q_3 species normalized with respect to the Q_2 species is presented. It is observed from the spectra that, the Q_3/Q_2 ratio is increasing with the dose along with a shift in the Q_3 position. This shift in the Q_n position was also observed in case of the alpha irradiated samples. This indicates an increase of the silicate network polymerization under ^{12}C beam irradiation as discussed earlier.

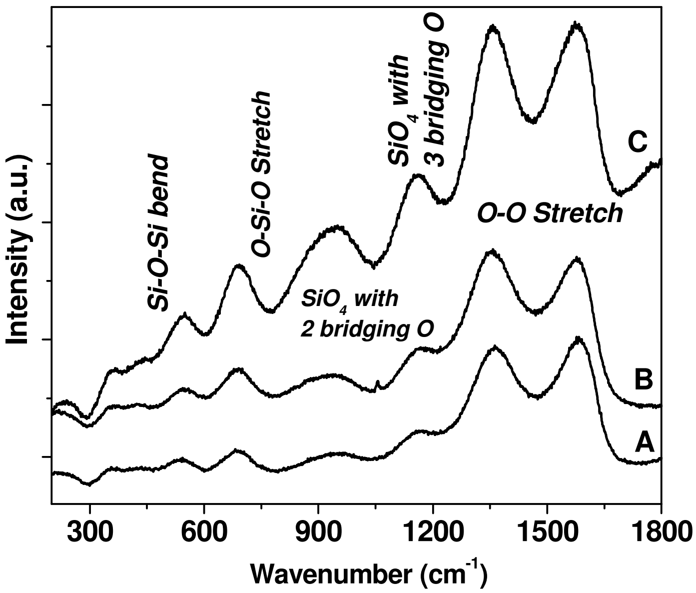

Figure 6.4 Raman spectra of the ^{12}C beam irradiated glass samples, A-10^{10} Gy, B-7×10^{10} Gy and C-10^{11} Gy

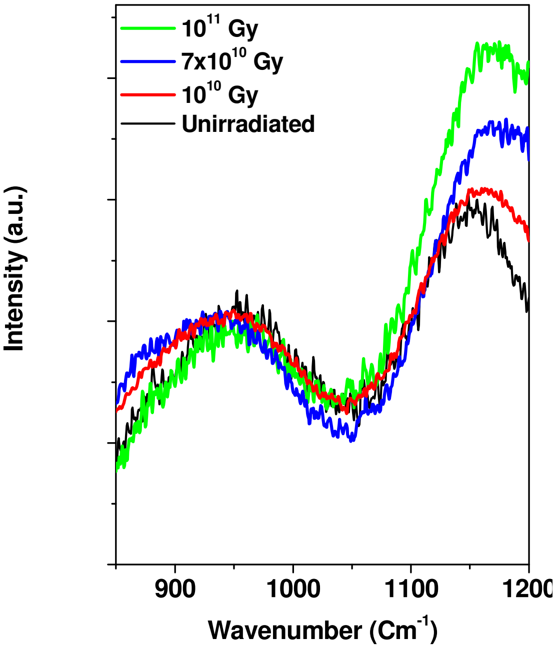

Figure 6.5 Raman spectra of the Q_3 species normalized with respect to the Q_2 species in the ^{12}C beam irradiated glasses

The intense and relatively narrow peak at 1550 cm^{-1} could not be identified conclusively. However, Boizot et al. have attributed similar peak to the O-O bond stretching of molecular oxygen in French nuclear waste glasses [23, 24]. On similar lines the peak was attributed to O-O vibration of molecular oxygen formed in the glass because of the heavy ion irradiation.

Thus, from the Raman investigations, migration of alkali ions in the irradiated glasses was confirmed along with formation of dissolved molecular oxygen.

B. Investigation by ATR-FTIR spectroscopy

1. Alpha irradiation

Figure 6.6 shows the infrared absorption spectra for the glass samples before and after alpha irradiation. In all the samples, the following absorption bands are observed.

(a) Small band at 600-750 cm^{-1},

(b) A very broad absorption band in the region 800-1200 cm^{-1},

(c) Another small but broad absorption band in the range 1225-1400 cm^{-1}

No significant change was observed in the band positions of the irradiated samples as compared to the unirradiated ones. A detailed discussion regarding the various IR absorption bands expected in the irradiated Trombay nuclear waste glasses was presented in chapter-5, based on which the broad absorption band observed in 800-1200 cm^{-1} region is assigned to the combined stretching vibrations of Si-O-Si and B-O-B four fold tetrahedral networks.

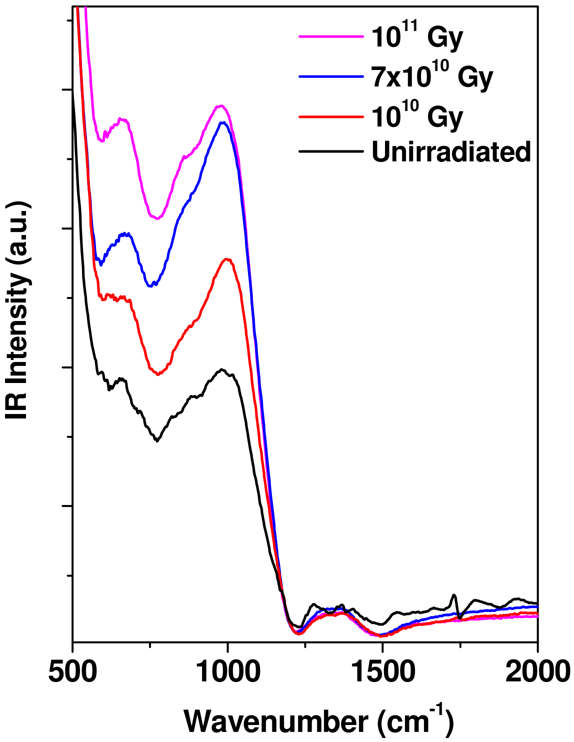

Figure 6.6 ATR-FTIR spectra of the ^{12}C beam irradiated borosilicate glasses

Similar types of features due to combined vibration of Si-O and B-O units have also been reported previously in aluminum, barium, lead and sodium borosilicate glasses [25-33]. Similarly, the band at 1225-1400 cm^{-1} region is attributed to the stretching vibrations of 3 fold BO_3 units with non-bridging oxygens (NBOs) [26, 27 and 33]. The band at 600-750 cm^{-1} is attributed to the bending vibrations of the bridging oxygen between the 3 fold BO_3 groups [34]. Absence of any significant change in the band positions suggested that the bulk of the glass remained unaffected after the irradiation.

2. ^{12}C beam irradiation

Figure 6.7 presents the FTIR spectra of the ^{12}C beam irradiated samples as a function of dose. As it was observed in case of the Raman experiments, in FTIR experiments also, the ^{12}C beam irradiated samples showed broad and noisy spectra. However the characteristic band due to the combined stretching vibrations of Si-O-Si and B-O-B four fold tetrahedral networks were clearly visible in the range 800-1200 cm^{-1}.

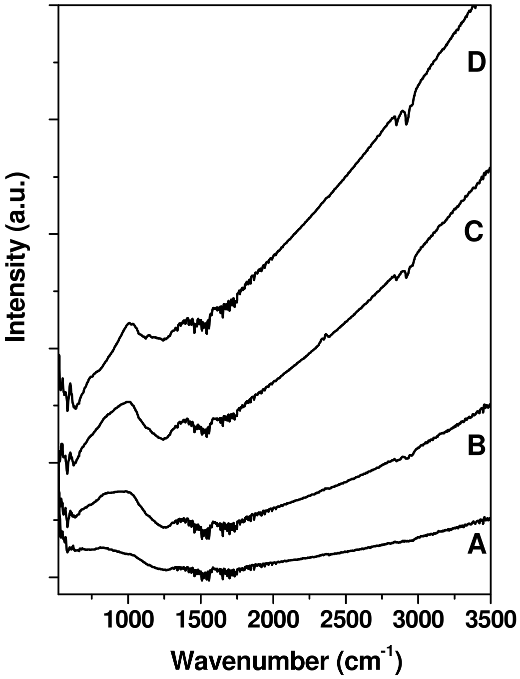

Figure 6.7 IR spectra of the ^{12}C beam irradiated glass samples as a function of dose; the cumulative doses (Gy) in the different samples were A(0), B(10^{10}), C(7×10^{10}) and D (10^{11}).

In the unirradiated sample, the peak corresponding to the stretching vibrations of NBOs, in the wavenumber range 1200-1400 cm^{-1}, was barely visible. However, on irradiation, the peak intensity increased suggesting the formation of more number of NBOs on irradiation.

The bending vibration of the bridging oxygens that was seen in the alpha irradiated sample could not be observed in this case due to poor resolution.

Thus, both the Raman and IR studies suggested similar type of changes in the glass samples after alpha and ^{12}C beam irradiations. While Raman studies suggested the breaking of the Si-O bonds at regular sites and migration of alkali ions, the IR studies suggested the formation of more and more number of NBOs in the irradiated samples which is a direct consequence of the breaking of the Si-O/B-O bonds.

However, the bulk glass network seemed to be unaffected. It may be noted here that, the high dose rate irradiation performed in the present case may cause some effects which might not be present in the actual HLW glasses. For this reason, insitu measurements are best suited where the actual conditions are simulated. Nevertheless, to start with, this type of exercise is best suited to simulate alpha damages as suggested by many workers [1, 6, 10 and 13]. The observations in the irradiated glasses in this case suggested the possible migration of the alkali ions, which may lead to an enhanced rate of ion exchange in the glass samples as suggested by Ojovan et al [35]. However, more investigations on the Trombay waste glasses are required to establish a one to one correlation between the heavy ion beam induced damage and leaching of the glass matrix.

6.4. Conclusion

To conclude, alkali barium borosilicate glasses were irradiated with alpha and ^{12}C beams to simulate the effects of heavy ion irradiation. The samples were irradiated for varying time period so that the total dose received by the sample was 1×10^{10}, 7×10^{10} and 1×10^{11} Gy. The radiation induced changes were investigated using micro Raman and FTIR spectroscopic techniques. The Raman investigations suggested a possible migration and segregation of the alkali ions along with modification in the glass network on irradiation. Formation of molecular oxygen and NBOs were also observed in the irradiated glass samples. However, the IR data suggested that the bulk of the glass matrix was unaffected even at the highest dose of 10^{11} Gy.

References

1. W.J.Weber, R.C.Ewing, C.A.Angell, G.W.Arnold, A.N.Cormack, J.M.Delaye, D.L.Griscom, L.W.Hobbs, A.Navrotsky, D.L.Price, A.M.Stoneham, M.C.Weinberg, J. Mater. Res. 12 (1997) 1946.
2. W. J. Weber, F. P. Roberts, Nucl. Technol. 60 (1983)178.
3. W. G. Burns, A. E. Hughes, J. A. C. Marples, R. S. Nelson, A. M. Stoneham, J. Nucl. Mater. 107 (1982) 245.
4. D. H. Day, A. E. Hughes, J. W. Leake, J. A. C. Marples, G. P. Marsh, J. Rae, B. O. Wade, Rep. Prog. Phys. 48 (1985) 101.
5. W. G. Burns, A. E. Hughes, J. A. C. Marples, R. S. Nelson, and A. M. Stoneham, in Scientific Basis for Nuclear Waste Management V, edited by W. Lutze (Mater. Res. Soc. Symp. Proc. 11, Pittsburgh, PA, 1982), p. 339.
6. R. C. Ewing, W. J. Weber, F. W. Clinard, Jr., Progress in Nuclear Energy 29 (1995) 63.
7. N. E. Bibler, in Scientific Basis for Nuclear Waste Management, edited by S. V. Topp (Mater. Res. Soc. Symp. Proc. 6, North- Holland, New York, 1982), p. 681.
8. G.W.Arnold, Radiat. Eff. 74 (1983) 151.
9. J.C.Dran, M.Maurette, J.C.Petit, Science 209 (1980) 1518
10. J. de Bonfils, G. Panczer, D. de Ligny, S. Peuget, B. Champagnon, J. Nucl. Mater. 362 (2007) 480.
11. J. de Bonfils, S. Peuget, G. Panczer, D. de Ligny, S. Henry, P.Y. Noël, A. Chenet, B. Champagnon, J. Non-Cryst. Solids 356 (2010) 388.
12. S. Peuget, J.-N. Cachia, C. Je´gou, X. Deschanels, D. Roudil, V. Broudic, J.M. Delaye, J.-M. Bart, J. Nucl. Mater. 354 (2006) 1.

13. R.A.B. Devine, Nucl. Instr. Meth. B 91 (1994) 378
14. L.D.Bogomolova, V.A.Jachkin, S.A.Prushinsky, S.A.Dmitriev, S.V.Stefanovsky, Yu.G.Teplyakov, F.Caccavale, E.Cattaruzza, R.Bertoncello, F.Trivillin, J. Non-Cryst. Solids, 210 (1997) 101
15. Hj. Matzke, Nucl. Instr. Meth. B 32 (1988) 455.
16. Hj. Matzke, Nucl. Instr. Meth. B 65 (1992) 30.
17. G.W.Arnold, Radiat. Eff. 98 (1986) 55.
18. S. Sato, H. Furuya, K. Asakura, K. Ohta, T. Tamai, Nucl. Instr. Meth. B 1(1984) 534.
19. N. Ollier, B. Boizot, B. Reynard, D. Ghaleb, G. Petite, Nucl. Instr. Meth. B 218 (2004) 176.
20. F.Y.Olivier, B.Boizot, D.Ghaleb, G.Petite, J. Non-Cryst.Solids 351 (2005) 1061.
21. M.Okuno, B.Reynard, Y.Shimada, Y.Syono, C.Willaime, Phys.Chem.Miner. 26 (1999) 304.
22. A. Manara, I.M.Antonini, P.Camagni, P.N.Gibson, Nucl. Instr. Meth. B (1984) 475.
23. B. Boizot, G. Petite, D. Ghaleb, B. Reynard and G. Calas, J. Non-Cryst. Solids 243 (1999) 268.
24. B. Boizot, G. Petite, D. Ghaleb, N. Pellerin, F. Fayon, B. Reynard, G. Calas, Nucl. Instr. Meth. B 166/167 (2000) 500.
25. E.I. Kamitsos, Phys. Chem. Glasses 44 (2003) 79.
26. K. El-Egili, Physica B 325 (2003) 340.
27. M. Arora , S. Baccaro, G. Sharma, D. Singh, K.S. Thind, D.P. Singh, Nucl. Instr. Meth. B 267 (2009) 817.

28. D. Singh, K. Singh, G. Singh, Manupriya, S. Mohan, M. Arora, G. Sharma, J. Phys.: Condens. Matter 20 (2008) 075228.
29. Y. B. Saddeek, M.S. Gaafar, S. A. Bashier, J. Non-Cryst. Solids 356 (2010) 1089.
30. V.S. Yalmali, D.S. Deshingkar, P.K. Wattal, S.R. Bharadwaj, J. Non-Cryst. Solids 353 (2007) 4647.
31. D. Singh, K.S. Thind, G.S. Mudahar, B.S. Bajwa, Nucl. Instr. Meth. B 268 (2010) 3340.
32. S. M. Abo-Naf, F. H. El Batal, M. A. Azooz, Mater. Chem. Phys. 77 (2002) 846.
33. S. Baccaro, Monika, G. Sharma, K.S. Thind, D. Singh, A. Cecillia, Nucl. Instr. Meth. B 260 (2007) 613.
34. V. Kumar, O.P. Pandey, K. Singh, Physica B 405 (2010) 204.
35. M. I. Ojovan, A. Pankov, W.E. Lee, J. Nucl. Mater. 358 (2006) 57.

Chapter-VII

Summary and Outlook

7.1 Summary

In the present work, an attempt was made to investigate the radiation induced changes occurring in the nuclear waste glass by various spectroscopic techniques. Non invasive techniques such as X ray diffraction (XRD), UV-Vis absorption spectrophotometry, photoacoustic spectroscopy (PS), photoluminescence (PL), electron paramagnetic resonance (EPR/ESR), positron annihilation spectroscopy (PAS), Fourier transform-infra red (FTIR) and Raman spectroscopy were utilized to characterize the irradiated as well as unirradiated glass samples. The glass composition was similar to the borosilicate glass which is being routinely used to vitrify the stored high level waste from research reactors at Trombay. Speciation studies of various metal ions expected to be present in the waste glass were also undertaken to know the oxidation states and coordination geometries of the ions in the glass. The glass samples were also incorporated with suitable spectroscopic probe ions to study the radiation induced changes taking place in the vicinity of the ions. The glasses were irradiated with gamma rays, electron beam and heavy ions to get a complete idea about the radiation damage in the glasses. Based on the work carried out, the following conclusions can be made.

(a) Speciation studies of various metal ions such as Cr, Cu, Eu, Fe, Gd and Mn in the glass prior to irradiation suggested that, most of the metal ions are stabilized in highly distorted geometries. While, Cr gets stabilized in the glass matrix in two oxidation states namely, 3+ and 5+ in distorted octahedral geometries, Cu ions gets stabilized as Cu^{2+} in Z-out configuration. Iron was stabilized in 3+ oxidation state both in tetrahedral and octahedral geometries. In case of Mn, it was found out that, apart from the usual 2+ oxidation state, it gets stabilized in the matrix in the form MnO_4^- and MnO_4^{2-} as well. Both the rare earth ions were stabilized in their trivalent states. Gd was observed to form Gd_2O_3 clusters in the glass. Judd-Ofelt (JO) analysis of the Eu spectra suggested the existence of short range ordering in the glass with existence of higher degree of covalence in between Eu and oxygen.

(b) The glass samples were irradiated with gamma rays at dose rates of 1kGy/hr and 8kGy/hr. cumulative doses of 2, 50, 250 and 900 kGy were given to all the glass samples after which they were investigated by spectroscopic techniques.

It was observed that on gamma irradiation, boron based oxy hole centers are formed in the glass along with E'centers. A detailed EPR study revealed the formation of at least five different radical centers in the glass after gamma irradiation. PAS studies revealed increase in free volume in the glasses due to gamma irradiation. J-O parameters were evaluated for the Eu ion in the irradiated glasses. The trend in the J-O parameters suggested that on irradiation, there was no change in the short range ordering of the metal ions. However, the long range ordering of the Eu ions got modified along with its site distribution. It was observed that, for the same gamma dose, incorporation of more iron in the glass, reduces the formation of defect centers. This was attributed to charge trapping process of trivalent Fe ions present in the matrix. An EPR spin counting technique was employed to evaluate the defect centre concentration in the glasses formed due to gamma irradiation. It was observed that, the total defect centre concentration in the 900 kGy irradiated sample was ~350 ppm suggesting that bulk of the glass remains unaffected at the above dose range.

(c) To simulate the effects of beta radiation damage, the base glass samples were irradiated with high energetic electron beam. The irradiations were carried out at room temperature in an industrial 2 MeV and 20 kW electron beam accelerator facility, ILU 6 (Budker Institute of Nuclear Physics, Russia) at Vashi, Navi Mumbai, India. The samples were irradiated for varying time periods so as to get cumulative doses of 10^5, 10^6 and 10^8 Gy (J/kg).

PL data of the irradiated glasses suggested the formation of NBOHC and E'-centers in the glasses after irradiation. EPR investigations were done on the samples to have a complete understanding regarding the defect centers formed in the irradiated glasses and get an idea about their chemical nature. These investigations suggested the formation of at least five different species in the irradiated glass samples as in the case of gamma irradiation. Exact Hamiltonian parameters for the radicals were evaluated by EPR simulation technique using SIMFONIA program. PAS studies indicated increase in the free volume size and fraction in the glasses after irradiation indicating more and more trapping of the positrons in the glass. Not much change in the glass network was observed from FTIR data. A spin counting technique was employed to evaluate the number of defect centers in the glass irradiated with highest electron dose. It was observed that even at 10^8 Gy, the number of defect centers are few hundreds of ppm as was observed for the gamma irradiated glasses. This in a way confirmed the radiation stability of the barium based borosilicate glasses.

(d) To simulate the effects of heavy ion damage, the glass samples were irradiated with alpha and ^{12}C beams. BARC-TIFR pelletron facility was used for this irradiation. The samples were irradiated for varying time period so that the total dose received by the sample was 1×10^{10}, 7×10^{10} and 1×10^{11} Gy. The radiation induced changes were investigated using micro Raman and FTIR spectroscopic techniques. The Raman investigations suggested a possible migration and segregation of the alkali ions along with modification in the glass network on irradiation. Formation of molecular oxygen and NBOs were also observed in the irradiated glass samples. However, the IR data suggested that the bulk of the glass matrix was unaffected even at the highest dose of 10^{11} Gy.

Majority of the work done in the present set of investigation are with high dose rate because of the high dose rate and high beam current. This may cause some effects which will be absent in the actual HLW glasses irradiated at the same total dose.

For this reason, in-situ measurements are best suited to fully simulate the actual conditions of irradiation. However, the nature of radiation induced defect centers formed in the glasses due to irradiation will be identical irrespective of the nature and dose rate of irradiation.

The formation of the defect centers discussed in the study do contribute to the unbinding of the alkali metals and result in an enhanced rate of ion exchange. However, more investigations on the Trombay waste glasses are required to establish an one to one correlation between the radiation induced point defects and leaching of the glass matrix.

The findings of the present study will serve as input for the study of radiation induced changes in the borosilicate glass matrices or varying composition which may come for the future generation of nuclear waste.

7.2 Future scope and extension of the work

- Use of synchrotron based spectroscopic techniques such as extended X-ray absorption fine structure spectroscopy (EXAFS) and X ray absorption near edge spectroscopy (XANES) for the speciation study of different glass constituents will give better understanding about the various oxidation states and coordination geometries. Moreover, these highly sensitive techniques can throw light on the exact changes taking place in the vicinity of the ion of interest.
- In addition to external irradiation, incorporation of isotopes of a specific radioactive decay can also be useful in studying the radiation damage. Suitable isotopes such as ^{244}Cm, ^{241}Am, ^{239}Pu (for alpha) or ^{137}Cs, ^{90}Sr (for beta) can be incorporated in the glasses and the in-situ radiation damage can be investigated.
- Attempts will also be made to investigate the effects of recoil damage by irradiating the glass samples with low energy ion beam (energy in the keV region).
- As the glass composition for waste vitrification is site specific, which in turn is dependent on the type of fuel, cooling period, reprocessing flow sheet etc., the radiation damage in other glass compositions will also be carried out.

Some of these activities have already been initiated.